MICROMEGAS TIME PROJECTION CHAMBER DEVELOPMENT FOR RARE EVENT DETECTION

Thesis presented at the Faculty of Sciences
to obtain the title of Docteur ès Sciences

By

Leila Ounalli

accepted by members of the jury:

Thesis advisor: Prof. Jean-Luc Vuilleumier

Internal co-advisors: Prof. Damian Twerenbold
Dr. Frederic Juget

External co-advisors: Prof. Viktor Zacek
Prof. Jose Busto
R.D. Yannis Gioamtaris

Neuchâtel, 25 october 2006

Université de Neuchâtel

FACULTE DES SCIENCES
Secrétariat-Décanat de la faculté
- Rue Emile-Argand 11
- CP 158
- CH-2009 Neuchâtel

IMPRIMATUR POUR LA THESE

Micromegas time projection chamber development for rare event detection

Leila OUNALLI

UNIVERSITE DE NEUCHATEL

FACULTE DES SCIENCES

La Faculté des sciences de l'Université de Neuchâtel,
sur le rapport des membres du jury

MM. J.-L. Vuilleumier (directeur de thèse), D. Twerenbold,
F. Juget, J. Busto (Marseille), Y. Giomataris (Paris)
et V. Zacek (Montréal)

autorise l'impression de la présente thèse.

Neuchâtel, le 26 février 2007

Le doyen :
T. Ward

UNIVERSITE DE NEUCHATEL
FACULTE DES SCIENCES
Secrétariat-décanat de la faculté
Rue Emile-Argand 11 - CP 158
CH-2009 Neuchâtel

To Naceur, Rayan, Maram, my mother and to the mind of my father.

Table of Contents

Keywords

Rare event, double beta decay, Micromegas, TPC, detection, Xe, CF_4, drift, amplification, energy resolution, gas gain, ,ionization, scintillation, collection, charge, attachment, large drift volume.

Résumé

Depuis les chambres à fils "MWPC" de G. Charpak en 1968, des développements nouveaux pour les détecteurs gazeux ont été récemment proposées. Les "GEM" (Gas Electron Multiplier), les "LEM" (Large Electron Multiplier) ou "Micromegas" (Micro mesh gaseous structure) ..., sont les exemples les plus connus.
Le but initial de cette génération est d'avoir des bonnes résolutions, un bas bruit de fond, une réponse rapide avec une efficacité élevée de détecteur et une bonne sensibilité dans le domaine qui nous intéresse (le domaine de la radioactivité naturelle).

L'objectif essentiel de ce manuscrit est de décrire le développement d'une chambre à projection temporelle (TPC) avec un plan de détection de type Micromegas, nommé Micromegas-TPC. Deux TPC's existantes ont été utilisées:

- Un petit prototype, nommé la miniTPC de Neuchâtel, a été consacré pour étudier les propriétés de transport dans le gaz et de développer le plan de lecture basé sur le micropattern Micromegas.

- Un prototype intermédiaire, nommé la TPC du Gothard, a été utilisé pour opérer le plan de détection de type Micromegas à grande échelle et estimer le bruit de fond de ce détecteur. Cette TPC a été optimisée pour fixer des paramètres importants pour la détection des événements rares, spécialement pour la désintégration double bêta sans émission de neutrinos dans l'isotope ^{136}Xe.

Ce manuscrit dispose de deux parties: les quatre premiers chapitres présentent quelques connaissances fondamentales, nécessaires pour la détection des événements rares avec les détecteurs gazeux. En particulier, les chapitres trois et quatre décrivent quelques résultats nécessaires pour l'étude de la collection de la charge. La deuxième partie du manuscrit décrit les résultats obtenus par la miniTPC de Neuchâtel et la TPC du Gothard.

Une courte description des propriétés de neutrino et les points manquants dans le modèle standard (MS) en ce qui concerne ces particules, ainsi que plusieurs efforts expérimentaux effectués pour compléter le MS, sont donnés dans l'introduction.

Le chapitre un, présente la désintégration double bêta dans l'isotope ^{136}Xe et explique ce dont on a besoin pour détecter ce phénomène rare.

Le Chapitre deux, contient quelques connaissances fondamentales pour la chambre à projection temporelle. En particulier, l'interaction entre la particule incidente et la matière contenue dans le détecteur. Quelques propriétés de détecteur et des facteurs importants, telle que la résolution en énergie et le gain du gaz, sont aussi définis.

Le chapitre trois, explique les mesures de l'ionisation. Les détails techniques et les procédures pour obtenir les résultats de début à la fin, sont également mentionnés dans ce chapitre.

Le chapitre quatre, contient des résultats obtenus des calculs des champs électriques dans la TPC et des propriétés de transport des électrons dans le gaz, avec des programmes Monte Carlo différents. Nous distinguons le comportement des porteurs de charges, spécialement, la vitesse de dérive et les diffusions des électrons dans un mélange de gaz.

La deuxième partie de ce manuscrit, qui comporte mes propres résultats, est subdivisée en deux derniers chapitres et ils correspondent aux résultats de deux articles futurs:

Le chapitre cinq, intitulé "les résultats de la miniTPC de Neuchâtel", étudiait les développements d'un nouveau plan de détection Micromegas. Ici, nous présentons des gains élevés avec une bonne uniformité dans des mélanges de gaz différents, mais aussi les propriétés de transport des électrons et le choix du mélange de gaz convenable pour la détection des événements rares. Un mélange de gaz intéressant "$Xe(98)CF_4(2)$", particulièrement convenable pour la désintégration double beta sans émission de neutrinos dans le ^{136}Xe, est aussi étudié.

Le chapitre six, intitulé "les résultats de la TPC du Gothard", présente la performance d'un grand plan de détection Micromegas (50 cm de diamètre) dans différents mélanges de gaz, en allant du gaz le plus rapide "CF_4" au gaz le moins cher "P10" ($Ar(90)CH_4(10)$). Le bruit radioactif atteint dans cette TPC et les matériaux pertinents contribuant à l'augmentation de ce dernier sont aussi présentés.

Finalement, des conclusions de nos résultats sont données, les projets possibles et les développements suggérés sont présentés.
Dans ce contexte, des efforts particuliers peuvent être adressé pour construire un prototype, qui peut étudier les signaux d'ionisation et de scintillation, pour améliorer la résolution en énergie.
De plus, des efforts pour lire les signaux de l'anode et de la scintillation primaire sont aussi extrêmement importants dans le but de déterminer exactement le temps "t_0" de la dérive des électrons primaires.

Abstract

Since the Multi Wire Proportional Chamber "MWPC" of G. Charpak in 1968, new developments in gaseous detectors have been recently proposed. Gas Electron Multiplier "GEM", Large Electron Multiplier "LEM" or Micro mesh gaseous structure "Micromegas" ..., are some of the best known examples.
The main goal of this new micropattern generation is to have good resolutions, low background, fast response with the highest efficiency and good sensitivity in the range of interest (the range of naturel radioactivity in our case).

The main purpose of this manuscript is to describe a development of a Time Projection Chamber (TPC) with a Micromegas detection plane, we called it "Micromegas-TPC". Two existing TPC's are used:

- A small prototype, called Neuchâtel-miniTPC, is devoted to study electron transport properties in the gas and to develop the read out plane based on the Micromegas micropattern.
- An intermediate prototype, called Gotthard-TPC, is used to operate the Micromegas detection plane in a large scale and to estimate the background of such a detector. This TPC detector is optimized to fix such important parameters needed for rare event detection, especially for neutrinoless double beta decay in the ^{136}Xe isotope.

This manuscript is laid out in two parts: the first four chapters present some of the fundamental background knowledge required for rare event detection with a gaseous detector. In particular, chapter three and four describe some results needed for charge collection study. The second part of the manuscript describes the Neuchâtel-miniTPC and the Gotthard-TPC results.

A brief description of neutrino properties and the Standard Model-missing points concerning this particle, as well as several experimental efforts done to complete the SM, are given in the introduction.

Chapter one, presents the double beta decay of the ^{136}Xe isotope and explains what we need as restricted conditions to detect this rare phenomena.

Chapter two, contains some fundamental knowledge on the Time Projection Chamber. In particular, the interaction between the incident particle and the matter contained in the detector. Some detector properties and important factors, such as the energy resolution and the gas gain, are also defined.

Chapter three, explains ionization measurements. Some technical details and procedures to obtain the results from the beginning to the end, are therefore done in this chapter.

Chapter four contains results obtained from the electric field configurations inside the TPC and the electron gas transport properties computations, with different Monte Carlo programs. We distinguish the behavior of charge carriers, especially the drift velocity and diffusions of electrons in the gas mixture.

The second part of this manuscript, which involves my own results, is divided in the two last chapters, which corresponds to two future papers:

Chapter five, called "Neuchâtel-miniTPC results", is devoted to the development of a new Micromegas detection plane. Here, We present the high and the good uniformity of the obtained gas gains, as well as the electron transport properties and the choice of the gas mixture convenient for rare event detection. An interesting gas mixture "$Xe(98)CF_4(2)$", particularly convenient for neutrinoless double beta decay in ^{136}Xe, is also studied.

Chapter six, called "Gotthard-TPC results", presents the performance of a large Micromegas detection plane (50 cm of diameter) in different gas mixtures, going from the fastest gas "CF_4" to the cheaper noble gas "P10" ($Ar(90)CH_4(10)$). The achieved radioactive background in this TPC, and the relevant materials contributing to enhance it are also presented.

Finally, some conclusions of our results are given and possible projects and suggested developments are presented.

In this context, particular efforts can be addressed to built a prototype, which will study

both ionization and scintillation signals to better improve the energy resolution.
Further efforts to read the anode and the primary scintillation signals would also be extremely important, in order to determine exactly the time "t_0" of the drift of primary electrons.

Introduction

We give a global view of neutrino properties and we proceed towards shortcomings in the Standard Model. In addition, we set out for experimental efforts to give answers to some delicate points or to complete this model.

Neutrinos are abundant particles, coming from everywhere. They are generated by numerous sources: they come from stars or supernova explosions. They can be produced by reactors, or by cosmic rays interactions with atmospheric atoms. They can also be produced by natural activities.

Neutrinos exist in three types, as observed by the LEP[1] experiments: electron ν_e, muon ν_μ and tau ν_τ, with respectively their antineutrinos: $\overline{\nu}_e$, $\overline{\nu}_\mu$, $\overline{\nu}_\tau$.

In the standard model, neutrinos are fermions, with spin 1/2. They have no charge and are massless. They interact only by weak interactions [1], thus they do not conserve parity. The neutrino spin has an opposite direction to the motion: it is "left handed" and the antineutrino is "right handed", because the latter spin has the same direction as the motion. The probability of interaction between neutrino and matter is extremely low. Thus, it is extremely difficult to detect them. This particle interacts so weakly, that it can go across the full earth without any collision.

[1] Large Electron Positron collider.

Three questions:

are neutrinos massive particles?

have they magnetic moments?

is the neutrino equal to its antineutrino?

are not answered by the Standard Model.

The first question is answered by all solar, atmospheric, reactor and beam neutrino experiments. First, solar neutrino experiments (GALLEX [2], GNO [3], Homestake [4], Kamiokande [5], SAGE [6], SNO [7], Super-KamioKande [8]) agreed that the measured flux of solar neutrinos is less than predicted by the Solar Standard Model (SSM), which confirmed that electron neutrinos "ν_e" oscillate when travelling from the core of the sun to our earth. Thus, *neutrinos are massive particles*.

The second question has no direct answer: electron neutrino experiments did not measure a magnetic moment but gave only a limit, even by direct measurements with detectors located next to nuclear reactors (TEXONO [9], MUNU [10] with a best limit $\mu_{\overline{\nu}_e} < 9.0 \times 10^{-11}\ \mu_B$ at 90% C.L), or by indirect measurements (KamLAND [11], Super-KamioKande [12] with a limit $\mu_{\overline{\nu}_e} < 1.1 \times 10^{-10}\ \mu_B$ at 90% C.L) when studying neutrino oscillations. The presence of the magnetic moment would confirm that:
Neutrinos are able to interact also by electromagnetic interactions.

The last question has no answer until now: only the neutrinoless double beta decay, if it exists, can determine the nature of the neutrino: it can be of the "Majorana" type, if the neutrino is equal to its antineutrino or of the "Dirac" type, if the neutrino and the antineutrino are different particles. In addition, neutrinoless double beta decay can determine the absolute scale of the effective mass of neutrinos and gives information about the matter-antimatter asymmetry. Therefore, this discovery is a unique way to give answer to the third question and also give clarifications to some ambiguities concerning this particle in the Standard Model.

Joined efforts are done by several experiments and theoretical studies, to know more about this particle, which will be a key for a new model.

Several experiments were studied this process (Gotthard [13], IGEX [14], NEMO-3 [15]), but the "$0\nu\beta\beta$" decay has never been observed. Future projets (CUORE [16], EXO [17], GENIUS [18], Majorana [19], MOON [20]) work hard to increase their detector-sensitivities to observe the neutrinoless double beta decay.

The Enriched Xenon Observatory (EXO) project, with its own idea of "Ba tagging" technique [21], and its great care when choosing the extremely radio-pure materials constructing the detector or shielding it, promises to observe this process and to reach the 10 meV limit for the mass with one ton of enriched xenon. The source mass of the first stage of the EXO detector is about 200 kg of xenon enriched in ^{136}Xe.

The extraction of the $^{136}Ba^{++}$ ion, called "Ba tagging" (the decay product of ^{136}Xe isotope), will reduce by a great factor the background caused by the "$2\nu\beta\beta$" decay, which is the major development done by the EXO collaboration.

In the framework of the EXO collaboration, we are working on our side on the development of the readout plane and we study, in parallel, the electron transport properties in Xe-CF_4 gas mixtures.

Chapter 1

Double beta decay and Standard Model

Despite its great success in particle physics, the Standard Model is not a complete theory of elementary particles and their fundamental interactions. This model does not include the gravitational interaction and does not explain the tiny asymmetry between matter and antimatter, as well as neutrino properties, especially their mass and nature.

In particular, in the standard model, neutrino masses are put to zero. The following hypothesis has been made by theoretical attempts [22]: "*Weak interaction eigenstates may not be mass eigenstates but superpositions of such states, introducing neutrino oscillation phenomena*", and has been confirmed by solar neutrinos experiments [2, 3, 4, 5, 6, 7, 8] and also by atmospheric [5, 8] and reactor [11] neutrino experiments. So, neutrinos have masses. A direct detection of neutrino masses will be achieved by neutrinoless double-beta decay experiments, which is a straightforward application to give the absolute scale of the effective mass of neutrinos.

1.1 Double beta decay

The double beta decay is an isobaric process transforming a (A,Z) nucleus to a (A,Z+2) one and emitting two electrons. Two main decay modes exist: the two neutrinos beta-beta decay "$2\nu\beta\beta$" and the zero neutrino beta-beta decay "$0\nu\beta\beta$".

1.1.1 The two neutrinos double beta decay

The two neutrinos beta-beta decay "$2\nu\beta\beta$", consists in the simultaneous decay of two neutrons of the initial nucleus into two protons in the final nucleus, two electrons, and two anti-neutrinos:

$$(A, Z) \rightarrow (A, Z+2) + 2e^- + 2\overline{\nu}_e$$

The lepton number is conserved in this process (ΔL= 0), which makes it allowed by the Standard Model.

The two electrons, carry only a fraction of the decay energy Q. The energy spectrum of the two electrons is therefore continuous extending from zero to the Q value (see the blue spectrum of figure 1.1).

This second order process is mentioned by Heisenberg in 1932 as a possible but rare process in nature. In addition, it has been observed for the first time by Moe [23] in 1986. It is already observed for several isotopes in many experiments (Heidelberg-Moscow [24] , IGEX [25], NEMO-3 [15]). The half life of the process exceeds 10^{18} years, depending on the considered nucleus (see appendix A).

1.1.2 The neutrinoless double beta decay

Neutrinoless double beta decay "$0\nu\beta\beta$" arises spontaneously. In this process, two neutrons of the initial nucleus decay simultaneously into two protons in the final nucleus, two electrons and zero neutrino:

$$(A, Z) \rightarrow (A, Z+2) + 2e^-$$

This decay mode is clearly forbidden by the Standard Model, because the lepton number is not conserved (ΔL= 2).

Given that, the two electrons, contrary to the "$2\nu\beta\beta$" mode, take away all the energy $Q_{\beta\beta}$ released in the decay. What we hope to see, if this very rare phenomena exists, is a fine and slight peak in the summed electron energy spectrum, centered at $Q_{\beta\beta}$ (the red peak of the figure 1.1).

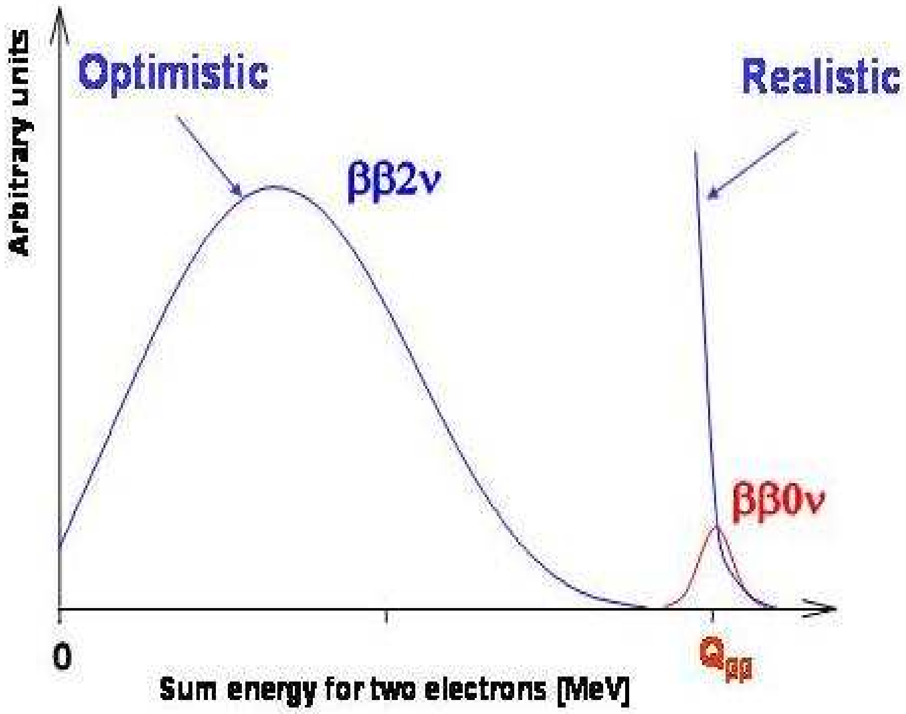

Figure 1.1: The theoretical energy spectra of the various double beta modes and the realistic view.

Up to now only the Heidelberg-Moscow experiment [24], claims the observation of the "$0\nu\beta\beta$" mode in the ^{76}Ge nucleus. It is considered as the most sensitive experiment until now (with no concurrence), with the lower bound obtained for the neutrinoless double-beta decay half-life of ^{76}Ge ($T_{1/2} > 1.5 \times 10^{25}$ y at 90% CL), which corresponds to an upper bound for the effective neutrino mass ($< m_\nu > < 0.39$ eV). Nevertheless, this result has not been confirmed by any other experimental groups.

Theoretically speaking, the "$0\nu\beta\beta$" mode is distinguished from the "$2\nu\beta\beta$" mode (the optimistic case of figure 1.1), but in reality the tail of the continuous spectrum of the "$2\nu\beta\beta$" decay spreads out until the "$0\nu\beta\beta$" peak region and can cover it (the realistic case of figure 1.1). Excellent energy resolution can reduce this background and distinguish the peak from the continuous spectrum.

1.2 Double beta decay in Xenon 136

In nature, several nuclei (see appendix A) are double beta decay candidates, with an energy release of a few MeV.

Xenon is a good candidate for the "$0\nu\beta\beta$" observation. It is considered as the best isotope among others, because it is the unique gaseous isotope, which helps to give a good tracking information and it is relatively easy to enrich. More details on the xenon properties are given in section 3.10.

The "$2\nu\beta\beta$" decay in ^{136}Xe has never been observed, because of the long half life compared with other isotopes. Only lower limits for the half life have been reported [13].

The double beta decay of ^{136}Xe will produce a doubly charged barium ^{136}Ba^{++}, with two electrons and 2 or 0 neutrino emissions.

$$^{136}\mathrm{Xe} \rightarrow ^{136}\mathrm{Ba}^{++} + 2\mathrm{e}^- + \begin{cases} 2\nu, \\ 0\nu, \ \ (Q_{\beta\beta} = 2.479\ \mathrm{MeV}) \end{cases} \tag{1.2.1}$$

The effective neutrino mass can be expressed as follows [26]:

$$< m_\nu >^2 = [T_{1/2}^{0\nu\beta\beta} G^{0\nu\beta\beta} |M^{0\nu\beta\beta}|^2]^{-1}, \tag{1.2.2}$$

where: m_ν, $T_{1/2}^{0\nu\beta\beta}$, $G^{0\nu\beta\beta}$ and $M^{0\nu\beta\beta}$ are respectively, the effective "Majorana" mass, the measured half life, the known phase space factor and the matrix element calculated from nuclear models.

Moreover, the half life limit $T_{1/2}^{0\nu\beta\beta}$ is derived from a statistical analysis, which can be expressed as [27]:

$$T_{1/2}^{0\nu\beta\beta} > C \cdot \xi \cdot i \cdot A^{-1} \left(\frac{M \cdot t}{b \cdot R_E} \right)^{1/2}, \tag{1.2.3}$$

where: C, ξ, i, A, M, t, b, R_E are respectively, a normalization constant, the detector efficiency, the isotopic abundance[1], the atomic number, the detector mass, the time acquisition, the background count rate and the energy resolution at the $Q_{\beta\beta}$ value.

As presented in equation 1.2.2, the neutrino mass is inversely proportional to the measured half life and can be deduced as below:

$$m_\nu \;<\; (b \cdot R_E)/(M \cdot t) \tag{1.2.4}$$

Observing the "0ν" peak, means reducing the background count rate, improving as much as possible the energy resolution, increasing the active mass and the measuring time.

The large mass of the detector (M) and the long acquisition time (t) are unavoidable factors and require only money and patience. Efforts should be consecrated to go to the lowest background level as possible and to improve the energy resolution, to separate the "$0\nu\beta\beta$" peak from the "$2\nu\beta\beta$" continuous spectrum.

A large size and high pressures are required, this is why liquid xenon will help to reduce the size of the detector, but there is no information about the track. This is why, we insist on the operation in the gas medium and we try to optimize the detector for good charge collection in xenon.

The advantage of the gas is its high mobility and its lower attenuation length. It allows the drift of electrons, especially, in a <u>*large drift volume*</u>. It is particulary simple to purify compared with liquid.

[1] Which depends on the enrichment of the gas.

1.3 Requirements for rare event detection

Solar neutrinos, double beta decay and dark matter, are experiments with very low event rate and low energy threshold. So, underground detectors with an energy threshold as low as possible are required.

1.3.1 Low energy threshold

Following elastic scattering, the recoil energy given to the nucleus is very small, ranging from a few keV to a few ten keV, according to the incident particle (neutrinos, WIMP[2]) and nuclei masses. This is why the choice of the gas candidate is important with respect to its atomic number and its cross section. The detector energy threshold should be as low as possible in the case of dark matter and solar neutrino detection.

In the case of the $\beta\beta$ xenon decay, the energy is in the range of natural radioactivity, so we need to improve the energy resolution and reduce the background count rate. Our work is therefore focused on these two fields.

1.3.2 Deep underground and low radioactivity

The deep underground location is essential to protect our detector from cosmic rays, which can increase the background and create fake events. Muons loose a considerable part of their energy when passing through rocks by ionization, pair production and nuclear interaction. For example, the muon flux is attenuated by a factor 10^6 when reaching the Gotthard laboratory.

In addition, an active shielding is essential to protect the detector from laboratory contaminations. Materials with high atomic number (Z), such as lead (Pb), is needed to attenuate gamma activities surrounding the detector. Low energetic photons, electrons and hadrons[3]

[2]Weak Interaction Massive Particles.

[3]even, if they are very little in the underground laboratory

are right away absorbed by the lead shielding.

The detector should be well protected against the external background as described above. A major effort was dedicated to reduce the intrinsic background of the detector components. Here the choice of ultra pure materials is mandatory. A considerable part of our work is the search and the purity testing of these components. Every material put in the detector, is strictly chosen in favor terms of low radioactivity measured by gamma spectrometry and low cost.

Chapter 2

Micromegas-TPC detector & ionization measurement

This chapter is devoted to a detailed description of what happens inside the detector. Several processes are involved when a particle arrives at the detector and crosses the medium, from the first energy deposition until the final acquisition of the information.
In order to understand more the functioning of such a detector, keep in mind the human visual perception. The light perception by the eye is a complex-phenomena which depends not only on the light-eye diffraction but also on the eye-retina structure (the detection plane in the case of the detector). It depends also on the transmission of the information by the optic-nerve (from the detector to the computer), the brain treatment of the information (computer acquisition) and the final visual-sensation which emerges to the conscience (data analysis).
The retina is the part of the eye that receives the light and converts it into a chemical energy. The chemical energy activates nerves that conduct the messages out of the eye into the higher regions of the brain. The striking similarity between the eye perception and the particle identification, pushes us to consecrate time to develop new readout techniques and optimize such a detector to achieve excellent particle detection.

2.1 The detector geometry

A particle crossing matter is subjected to collide with the atoms forming it. It can scatter elastically from a nucleus via the coulomb force, or be absorbed via inelastic collisions. Therefore, a detector should have a complete azimuthal-coverage to contain the majority of interaction-products.

A spherical detector allows a full coverage and an uniformity of the azimuthal region. For example, the NOSTOS project [28], with its spherical geometry, will have a full acceptance. It is difficult to insure a good flatness of a big readout plane, moreover when following a spherical surface. Here, the detection plane will be a real problem. For this reason, most of detectors had a concentric-cylindric form, such as Time Projection Chambers, called "TPC"s.

The TPC chamber was used by several experiments: ALEPH and DELPHI in 1980, STAR and Gotthard in 1990, ALICE and MUNU at around 2000. This technique is still used by future experiments, such as ICARUS and EXO.

2.1.1 The Time Projection Chamber:

The Time Projection Chamber, invented by Dave Nygren at Berkeley in 1974 [29], is a proportional chamber filled with gas or liquid. It plays a major role to probe processes with excellent imaging capability and good resolution. Hence, with rapid electronics, it is considered as a tridimensional camera, which can show particle tracks.

The TPC detector is the only manner that gives information about the time component "Z", also called longitudinal coordinate. It permits measurements of space points (X, Y, Z) along a particle trajectory: X-Y coordinates are obtained from the detection plane and the Z coordinate from the drift time. The measurement of the third coordinate requires a precise knowledge of the drift velocity.

An important characteristic of this detector is the tracking capability and the ability to

distinguish the particle type by the deposited quantity of charge. Consequently, a good rejection of bad events by particles identification is a good feature of this detector.
In addition, the compact TPC design permits to purify continuously the fluid filling it and fluid recuperation is also possible, which is important in the case of expensive noble gases like Xe.

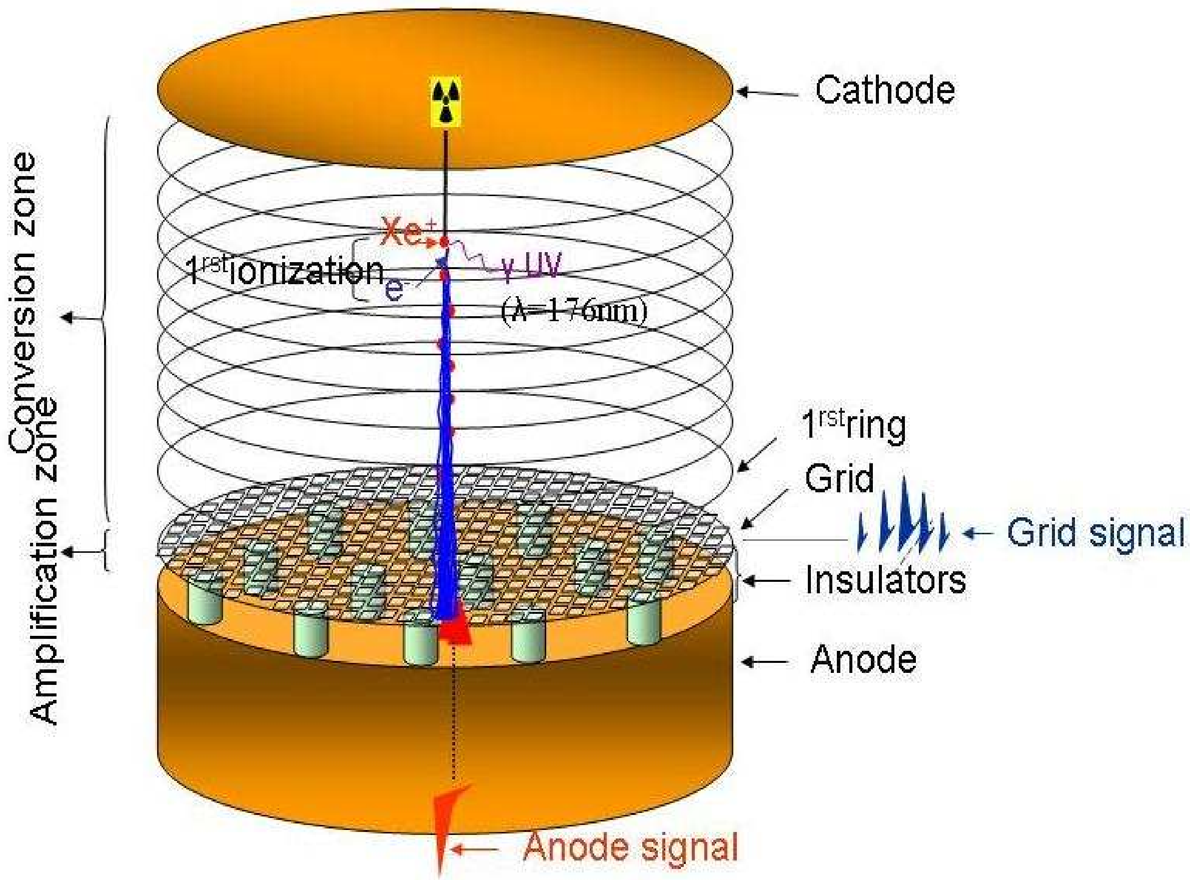

Figure 2.1: X-ray absorption with a gas Micromegas-TPC.

The TPC is divided into two zones as presented in figure 2.1:

- The first one is, at the same time, a conversion and a drift zone, where the primary ionization occurs. It insures the drift of electrons to the anode plane and ionized molecules (or ionized atoms) to the cathode plane.

- The second one, called the amplification zone (also called the gap height), is intended to amplify the ionization in order to have a detectable signal.

Usually, TPC's with MWPC anode plates are used as readout planes. In the last decades, several end plates with micropatterns are combined with the TPC. Some of them are cited in appendix B.
In this work, we combine a TPC with a Micromegas detection plane and we called it a "Micromegas-TPC".

2.1.2 The Micromegas micropattern

The Micromegas (Micro Mesh Gaseous Structure) consists of a two-stage parallel-plate avalanche chamber with a small amplification gap (> 50 μm) combined with a long conversion-drift space (some mm to few meters). The design and the principle of functioning of a Micromegas detector is shown in figure 2.2.
The Micromegas micropattern, with its simple geometry (parallel plate chamber), is a high gain gaseous detector [30], which can operate without additional preamplification. A full description of the Micromegas used for our tests, is given in the subsection 3.1.1.

2.1.3 The Micromegas-TPC

The Micromegas-TPC consists of a TPC chamber combined with a Micromegas detection plane, in which a small amplification gap (between 75 and 250 μm in our case) is combined with a long conversion-drift space (18 cm for the Neuchâtel-miniTPC (see figure 3.1) and about 70 cm for the Gotthard-TPC (see figure 6.1)). This *large drift volume* required a high purification of the gas.

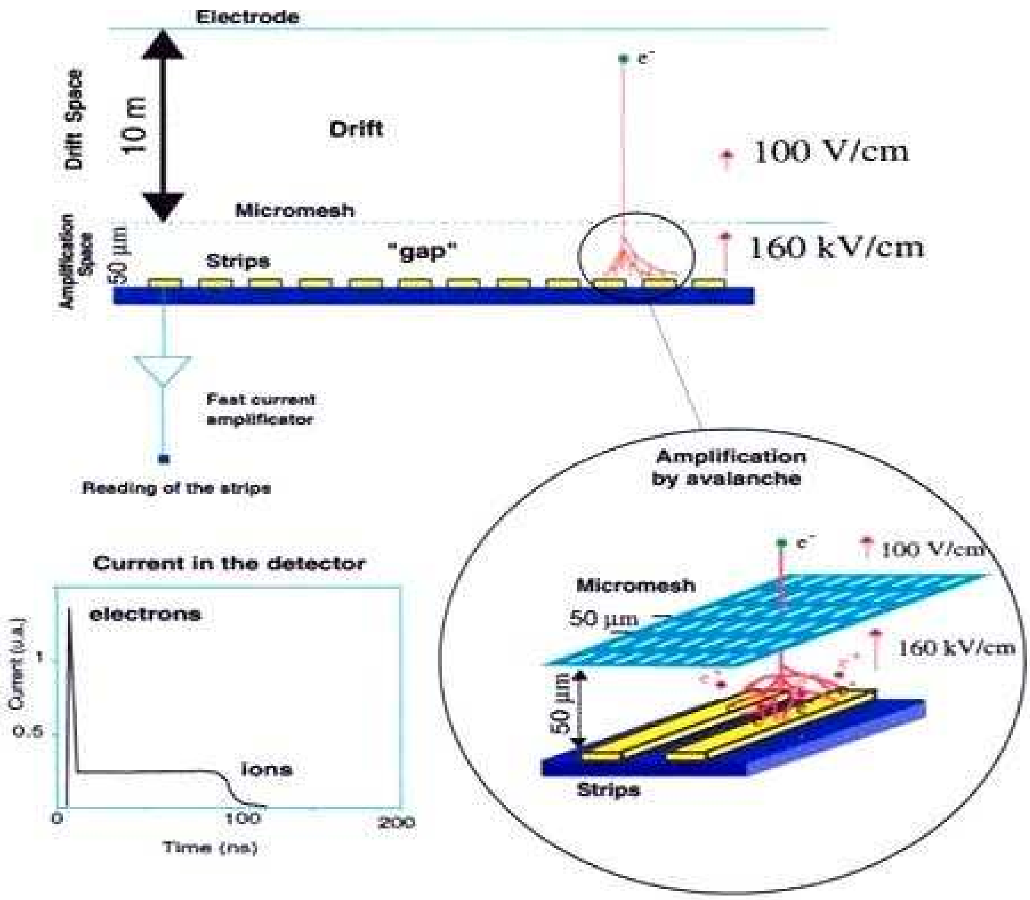

Figure 2.2: The principle of functioning of a Micromegas detector.

2.2 The ionization measurement

Two parameters need to be understood for rare event detection:

- The particle-matter interaction.
- The characteristics of the detector.

The particle-matter interaction is a function of the nature of the incident particle and the gas properties (in the case of gaseous detectors).

In the case of neutrinos, if they interact, the deposited energy is transferred to the detector medium, where it is converted into a measurable signal. Consequently, more efforts should be devoted to study the gas medium, to insure good transport properties (higher drift velocity, lower longitudinal and lateral diffusions ...). In addition, we should optimize the detector to operate it at the highest possible pressure, to increase the detector mass and contain better the particle tracks.

2.2.1 The particle-matter interaction & Processes inside the TPC

Let us choose a photon as an incident particle and a gas as a detection medium (Xe as a main gas and CF_4 as an additive).

The incoming photon interacts, by photoelectric or Compton effects (in the case of a low energy photon), and gives its energy to the ejected electron, ionizing a gas molecule. The ejected electron, with a given energy, will travel through the gas medium, producing primary ionization. These electrons undergo multiples scattering which somehow randomizes the ionization trail.

In order to increase the probability of interaction of the incident particle with the target nucleus, the pressure of the gas must be high enough.

Several processes take place in the heart of the detector as recapitulated in figure 2.1. Let us review them in more details, starting by the gas ionization and ending with the charge collection.

a. The gas ionization

When crossing the medium, the low energetic photon ionize the Xe atom by photoelectric effect, producing an electron-ion pair similar to the equation C.2.1:

$$\gamma + \mathrm{Xe} \rightarrow (\mathrm{Xe}^*)^+ + e^- \tag{2.2.1}$$

In turn, the electron is slowed down in the gas. It produces primary electrons:

$$N_i = \frac{E_{dep}}{W_i}, \tag{2.2.2}$$

where W_i is the average energy required to ionize the gas and E_{dep} is the deposited energy of the incident photon.

b. The liquid ionization

If the electron density is sufficiently high, which is the case of liquefied noble gases (Ar, Kr and Xe), an excited ion drifting to the cathode can encounter another atom and contribute to the ionization by the "*associative ionization*":

$$\mathrm{Xe} + \mathrm{Xe}^* \rightarrow \mathrm{Xe}_2^+ + \mathrm{e}^-.$$

The product of the last process can lead to the recombination of an ionized xenon atom with an electron, which yields to the so called [31] "*recombination luminescence*":

$$\mathrm{Xe}_2^+ + \mathrm{e}^- \rightarrow \mathrm{Xe}_2^*.$$

Then, the excited Xe_2^* produces scintillation photons by relaxation:

$$\mathrm{Xe}_2^* \rightarrow 2\,\mathrm{Xe} + \mathrm{h}\nu$$

c. The gas de-excitation

When de-excited, the gas molecule can emit a photon or an electron by "Auger effect" (see appendix C.4). Products of de-excitation, can by their turn ionize the gas medium and their behavior is like that of Delta electrons.

In the case of xenon gas, when excited positive ions $(\mathrm{Xe}^*)^+$ reach the cathode, they are neutralized and often release a 12.13 eV photon. Due to the photoelectric effect, this can liberate an electron from the cathode, which may in turn lead to serious sparks. One role of "quench gas" is to absorb such photons. Quench gas is also, and more importantly, necessary to delay the transition from proportional to Geiger mode (see appendix D).

d. The quencher

A small addition of an hydrocarbon polyatomic gas to noble gases, essentially, allows higher fields and higher gas amplification, smaller diffusions and higher drift velocity.
When the excited ion collides with a neutral quencher molecule, such as iso-C_4H_{10}, an electron is transferred from the quencher compound to the excited ion of xenon by the "Penning effect" (see appendix C.5):

$$\mathrm{Xe}^* + \text{iso-}\mathrm{C_4H_{10}} \rightarrow \mathrm{Xe} + (\text{iso-}\mathrm{C_4H_{10}})^+ + \mathrm{e}^-$$

Then, the iso-C_4H_{10} ion drifts to the cathode and neutralizes there.
As described above, a small quantity of an hydrocarbon gas is added to "mop up" any free electrons produced in the cathode. This addition allows operation with a gas gain up to 10^3 (see the left of figure 5.1), without any breakdown of the chamber.
Even if it violates the penning effect, CF_4 gas is chosen for its high drift velocity and low diffusions.

e. The gas amplification

Electrons, produced in the drift space, ionize the gas. The ionized electrons drift smoothly to the detection plane under a uniform electric field, created by grid, cathode and field shaping rings (see figure 2.1).
When reaching the frontier drift-amplification zones, electrons are attracted under the high electric field to the anode and they are fast enough to ionize the gas more and more and create avalanche-ionization, with low diffusions and high velocities.
These cloud of electrons go down and are inhaled to populate the anode. The uniformity of the electric field in the amplification region maintains the good stability in the avalanche development.

Local recombination in densely ionized region, essentially in the amplification gap, is suppressed by the high electric field, where the avalanche occurs.

Since most of the ions are produced in the lower region of the grid, they are drifting in the opposite direction of electrons and go up along the central field lines. The grid hole should be large enough to support this shower and the ratio between the amplification and electric fields should be high enough to insure the high efficiency of ions collection on the grid [30].

When encountering lower drift electric field[1], the majority of positive ions are quickly lapsed on the grid.

The charge collected on electrodes is:

$$Q_f = G \cdot e \cdot N_i, \tag{2.2.3}$$

where G is an amplification factor or the gas gain, N_i is the number of primary electrons defined in the equation 2.2.2 and e is the elementary charge.

The gas gain is the collected charge over the initial charge given by the first ionization.

f. Ions feedback and space-charge effects

Ions in the TPC drift volume represent a positive space charge and can deteriorate the homogeneous electric drift field, thus leading to track distortions [32]. The ion back drift can be derived from the measurements by dividing the drift current by the grid current.

Big problems are encountered with the single GEM micropattern [33], coming from a strong field effect caused by ions drifting back to the cathode, which limits the gas gain.

Several studies of the ion feedback suppression with a Multi-GEM structure are done [34, 35].

The feedback of ions is proportional to the $\frac{E_d}{E_a}$ ratio, where E_d and E_a are respectively drift and amplification fields. The latter ratio should be exceedingly low. In the case of

[1] $E_d = 200\ \mathrm{V{\cdot}cm^{-1}{\cdot}bar^{-1}}$.

Micromegas detector [36], the ion feedback to the cathode plane is strongly suppressed as confirmed in the section 4.2.

g. The attachment

The presence of electronegative impurities, such as O_2, H_2O, CO_2, CCl_4 ..., especially in the amplification region where the electric field is very high, reduces the efficiency of the detector by attaching electrons before attaining the anode plane. Moreover, the presence of this impurities, can contribute seriously to increase fluctuations of the ionization process and therefore, worsen the energy resolution.

In addition, loss of electrons can be caused by the main gas itself like CF_4 and can affect seriously the efficiency of the detector. The electron attachment process in this gas, was seen to become important only in very high electric fields (a few $kV.cm^{-1}$) [37]. Detailed studies of the electrons lost by CF_4 attachment are presented in the subsection 5.2.2.

h. The charge collection

After all these processes and (electrons & ions) travelling, the signal makes its first appearance, corresponding to the start of the grid collection of positives charges due to positive ions.

Using fast electronics, one can read out, in parallel, the anode signal and avoid the doubt of complete charge collection and ion feedback consequences.

The Micromegas grid collects the ionization ions to form a charge signal. The information from the detector is transformed into electrical pulses, which can be treated by an electronic system. To realize faster transmission and more accurate treatment of the information, a readout plane with fast electronics and computer acquisition are required.

i. The response of the detector

The response of the detector is the relation between the energy loss by the incident particle and the total charge or the pulse height of the output signal.

The particle-matter interaction produces electrons and ions, which will be absorbed in the detector gas. The output signal is in the form of a charge pulse and the ionization amount is reflected in the electrical charge signal, it means the integral of the pulse with respect to time.

j. The image reconstruction

Primary or secondary electrons generated by incident particles[2] in the gas, follow the electric lines of the event to the X-Y plane (strips).

The strip readout, recording the event, allows a full 2-D image reconstruction. Each of the strip planes of the anode provides a two dimensional projection of the event (α, p, e ...).

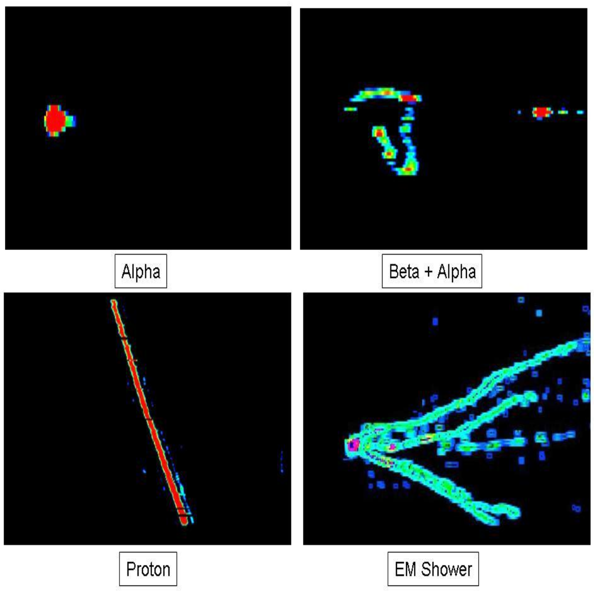

Figure 2.3: Typical tracks recorded by the MUNU detector at 3 bar of CF_4 gas.

[2]primary or secondary ionizations

Some events recorded by the MUNU TPC [38] are presented in figure 2.3. The α particle (top-left) deposits all its energy at almost one point. The top-right picture shows β and α events, and the two bottom pictures are some rare events: a proton (bottom-left) and an electromagnetic shower (bottom-right).

The absolute Z coordinate is not determined, since the absolute to time is not measured.

2.2.2 Detector characteristics

The detection of massless particles is a complex phenomena, which depends not only on the particle-matter interaction, but also on the detector characteristics, such as its sensitivity and its efficiency.

a. The sensitivity of the detector

Light represents the visible part ($330 < \lambda < 780$ nm) of a board spectrum, in which the human eye is sensitive. Similarly a detector has a range of energy, in which it is sensitive. The sensitivity of the detector to a particular radiation with a given energy depends on several factors:

The cross section of the detector reaction The detector should contain the majority of the ionizing reactions taking place in it.

The detector mass: A higher mass density and volume are necessary to increase the interaction rate, hence the sensitivity of the detector. This is why, several tons of mass detector are necessary for neutrinos and dark matter detection.

The internal radioactive noise: The inner detector noise, such as radio-impurities of components (shaping rings, detection plane, resistors, glue, solder ...), is responsible for the background count rate increase, decreasing the detector sensitivity when searching for rare events.

The external radioactive noise: The surroundings of the detector, including the shielding, the environment and cosmic rays, can affect seriously the detector sensitivity. This is why, rock covering and active shielding are essential when seeking for rare events.
The electronic noise: The ratio of the ionization signal produced in the detector over the average electronic noise level at the detector output, must be as high as possible.

b. The efficiency of the detector

The intrinsic efficiency of the detector depends on the number of electron-ion pairs produced and collected. It depends on the energy loss, the height of the amplification volume, the gas, voltages, noises, ... and on the geometry of the detection plane.

2.2.3 The energy resolution

The energy resolution determines the ability of the detector to distinguish close spectrum lines. It can be measured by sending a monoenergetic radiation into the detector and observing the resulting spectrum. It is determined by the statistics of the statistical fluctuations in the ionization process and the initial electron cloud. So it depends strongly on gas properties and on the uniformity of the drift and the amplification electric fields.
In reality, we usually observe a peak structure with a finite width and a gaussian form. This width depends on fluctuations in the produced ionization. It is also defined [39] as follows:

$$R_E = 2.35\sqrt{\frac{FW_i}{E_{dep}}}, \tag{2.2.4}$$

the factor 2.35 relates the standard deviation of a gaussian to its Full Width at Half Maximum "FWHM". F is the Fano factor for the gas mixture, which represents fluctuations in the number of electron-ion pairs. $F < 1$, for gases detectors [39]. A Fano factor of about 0.29 ± 0.02 and an ionization energy of about 21.9 ± 0.3 eV in Xe and for α particles were obtained [40]. Note that the Fano factor in xenon for α particles is as larger than that for electrons by a factor two.

Two factors can degrade the optimum resolution: attachment of drifting electrons and variations in the paths followed by primary electrons to the avalanche region.

An additional factor on which the energy resolution depends, is the electronic noise. The contribution of the latter is often very low and should be negligible compared to that caused by the statistical fluctuation in the number of ionizations (see the section 3.5).

2.2.4 The spatial resolution

The spacial resolution depends on the distribution of primary ionization electrons, diffusions, readout electronics and gas amplification. It depends on the space between two anode wires, in the case of MWPC, and on the strip dimension on the X-Y plane.

An important parameter, which plays a major role to improve the spatial resolution is low transverse diffusions. It can be achieved by using fast gas-mixtures (see the subsection 4.3.2) or by increasing the gas density. In addition, an applied magnetic field parallel to the drift direction improves the space resolution.

2.2.5 The time resolution

In the case of X-rays detection, the time resolution is good, because of the short time structure pulse. Thus, all electrons arrive within nanoseconds between them. If we collect rapidly the charge, time resolution is good. This can be achieved by using fast gases and rapid electronics.

These two latest parameters, space and time resolutions, are not directly studied in this work.

Chapter 3

Charge collection study & gas choice

Introduction

Our goal is to achieve the highest gas gain, a good energy resolution and to choose a convenient quencher.

To accomplish this goal, we should before, understand the charge concept and be familiar with terms and the shape of the detector response.

In this chapter, we try to disentangle some ambiguities. For example: why we choose this gap height and not another? Why we apply such a drift field?

All tests are done with a ^{55}Fe source and (P10, CF_4, Xe) gas mixtures, at different pressures and various gap heights (75, 100 and 225 μm).

3.1 The prototype TPC

Our prototype detector is a Time Projection Chamber (20 l of volume), as shown in figure 3.1. It was set up, for the first time, to study the transport properties of CF_4 gas in a *large drift volume* using a MWPC as a detection plane. These studies were used for the MUNU experiment [41]. It was also used to study the performance of the Micromegas micropattern using a woven wire mesh as a grid in pure CF_4 gas, compared with a nickel grid [42].

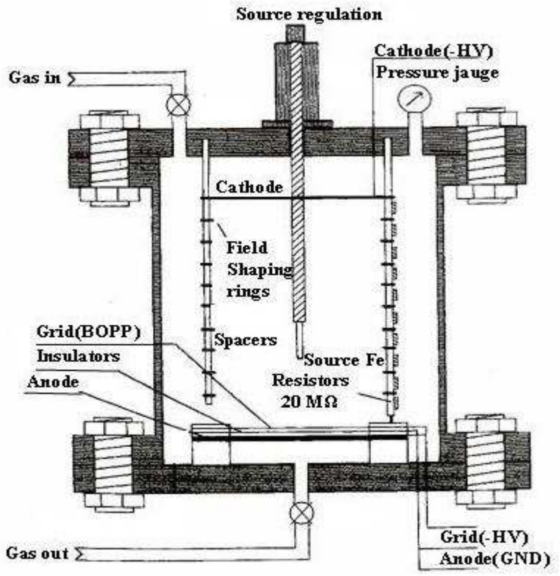

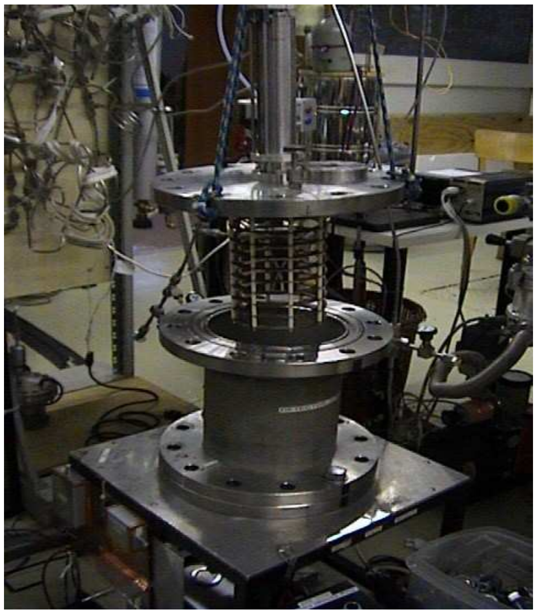

Figure 3.1: The Neuchâtel-miniTPC prototype and a photographic view, used to study the gas properties and to develop the detection plane.

The Micromegas-miniTPC is enclosed by a grounded stainless steel vessel, which can be evacuated down to 10^{-6} mbar before every test.

To achieve a uniform electric field inside the chamber, evenly spaced field shaping rings are placed inside the TPC, connected with equal value resistors (10 MΩ) and separated by a nonconducting material (delrin). Field uniformities, even in the drift volume or in the amplification gap, are studied with Maxwell [43] and Garfield [44] as described in the section 4.1.

3.1.1 The detection plane

The detection plane is a Micromegas micropattern. The anode and the grid, separated by spacers, are compacted "two in one" as it is shown in figure 3.2. It is also called a "compact" Micromegas [45].

The full anode with spacers was developed by the CERN surface treatment service [46]

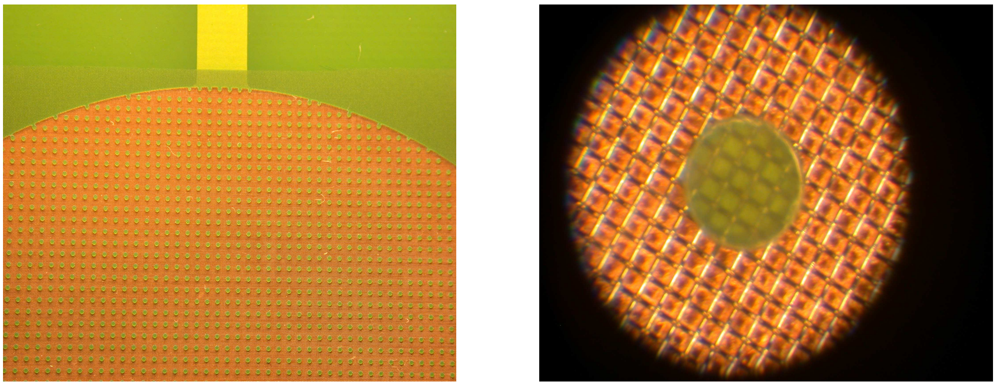

Figure 3.2: A photographic view of the detection plane (left) and a microscopic zoom on one spacer (right). The diameter of the spacer and the opening of the grid are 250 μm and 53 μm, respectively.

and the grid was tensed delicately at Neuchâtel.

The anode is a continuous copper plane: it has a diameter of about 9 cm with cylindrical pin spacers. The diameter of one spacer should be 2.5 times bigger than its height (exp. 250 μm of diameter by 100 μm height). These spacers are formed with kapton, placed every 1 mm and their height represents the amplification gap dimension.

The grid is made of stainless steel wires[1] with 20 μm of diameter, woven with a 53 μm spacing. This grid is cheap, easy to handle, robust (no damage were observed on the grid even under higher voltages or after some discharges), with low radioactivity[2] (see table 6.1), and it can be obtained in large sizes (2.5×30.5 m^2). A large size device (50 cm of diameter)[3] was tested in the Gotthard-TPC with P10 and CF_4 gases and good efficiencies were observed. Detailed studies are shown in the Gotthard-TPC results (chapter 6).

The presence of a great quantity of insulators in double-sided kapton micropatterns (GEM, MSGC ...) can be a source of background in the low rate experiments with low energy threshold. This is one of the arguments to give a preference to this simple mechanical

[1]From Bopp company [47].

[2]No chemical etching.

[3]Compass detections planes: GEM and Micromegas are about (31×31) and (40×40) cm^2.

woven grid.

Best results with good charge collection, have been obtained for the gap close to 100 μm [48], which justifies our choice of this height.

Before being mounted, the anode plane is washed with isopropyl alcohol and dried with a fine aspirator brush to remove dusts and scraps from manufacturing and to keep humidity low. The least humidity in the chamber, especially in the narrow gap can affect the energy resolution, and some dusts on the surface of the grid can increase the frequency of discharges and usually prevent the charge collection.

Great care has been taken when handling the detection plane, to avoid gap deformation. Obviously, defects of flatness are responsible for gain fluctuation and therefore affect the energy resolution.

3.1.2 The gas system

The performance of the detector is influenced by electronegative contaminants, which absorb the primary or secondary electrons. This is why continuous purification is necessary and a gas station is installed near the chamber as it is shown in figure 3.3.

To achieve good purity, the chamber was evacuated to 10^{-6} mbar while heating to evaporate humidity, before each gas filling.

The purification of the gas from electronegative admixtures has been realized in a flow-type, circulating the gas through two "*oxysorb*" filters: one to absorb oxygen contaminants (O_2, H_2O ...) and the second one in series for the control. A cold trap serves to remove water and possible freon contaminations.

The gas is continuously recirculated to improve the uniformity of the distribution in all the volume, especially in the avalanche volume. Moreover, the purity of the gas is controlled with mass spectrometry as described in the subsection 3.3.1.

The color of the "*oxysorb*" filter deviates to brown when it saturates with oxygen and when

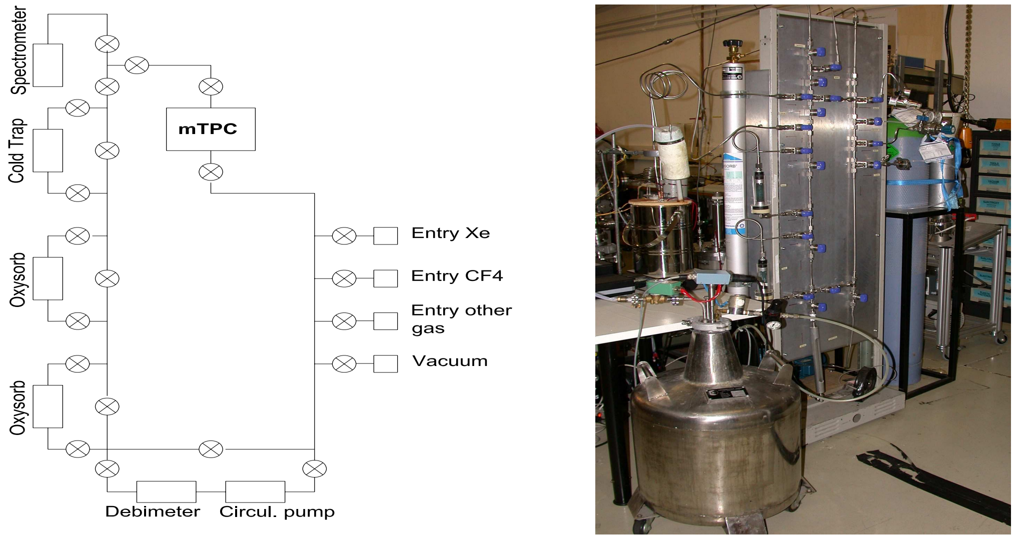

Figure 3.3: Schematic (left) and photographic view (right) of the gas system of the miniTPC.

there is a leakage in the purification system, and violet in the presence of humidity. Undoubtedly, the gas has to be very pure to allow low attachment.

3.1.3 The electronic system

The detector was operated with the cathode at a negative potential, the anode at ground and the grid at a negative potential of several hundred Volts. Figure 3.4 depicts the electronic system used to study the charge collection.

The incoming charge, generated by the detector, is collected on a capacitor (C= 10 pF). Then, it is amplified by a charge-sensitive preamplifier "ORTEC 142iH" and then amplified again and shaped in a gaussian form by a spectroscopic amplifier "ORTEC G72". Then, the multichannel analyzer sorts out the incoming pulses by the pulse height and stores information in the multichannel memory. The contents of each channel can then be displayed on a screen to give a pulse height spectrum, which is the response of the detector.

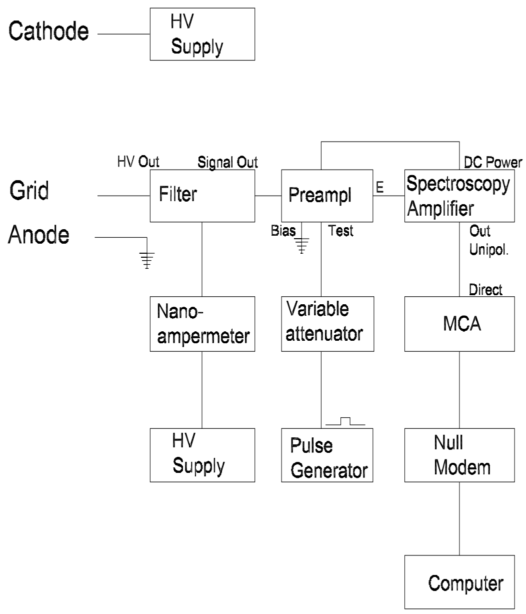

Figure 3.4: Schema of the miniTPC electronic system.

The mean value of the ionization current is obtained by a slow base time oscilloscope (Autoranging Combiscope "Fluke PM3392 A") via a nanoampermeter "ICM 035".
In order to reduce the electronic noise, the crate that holds the amplification electronic system and the pulse generator calibration system had a common ground. This ensures that there is no potential difference between the grounds of the various components, which could cause noise. This is accomplished through the use of ground braids and conductive copper tape.
We have a *weak signal* and we should preserve the information contained in it. This is why the charge preamplifier is mounted close to the detector in order not to loose the information.

3.2 The signal form

Before starting real tests, we should control the signal properties and the signal to noise ratio and we should be sure that there is no electronic oscillation, that can deteriorate the resolution of our physical signal or falsify it.

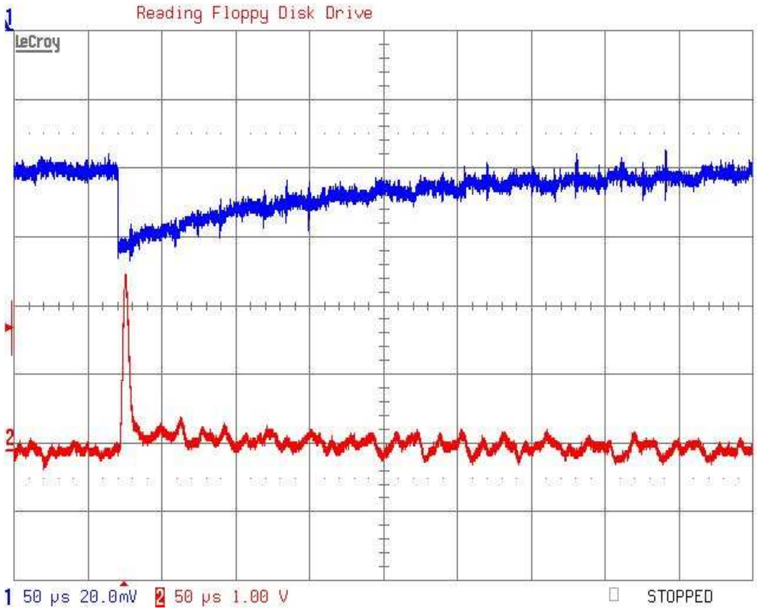

Figure 3.5: The shape of the preamplifier output (blue) and the spectroscopic amplifier (red), recorded in the scope.

The output of the preamplifier should give a negative pulse with an exponential tail, in the mV range, and the spectroscopic amplifier output should have a gaussian form in the range of a few volts.

Figure 3.5 shows a typical event signal of ^{55}Fe X-rays in CF_4 gas at 1 bar of pressure and 100 μm of gap. The signal to noise ratio is quit high. The slowness of the rise time (about hundred ns) is normal, because we collect ions and not electrons. This is why it is important to read the anode signal. In addition, there was no gas purification when recording these preamplifier and spectroscopic amplifier signals.

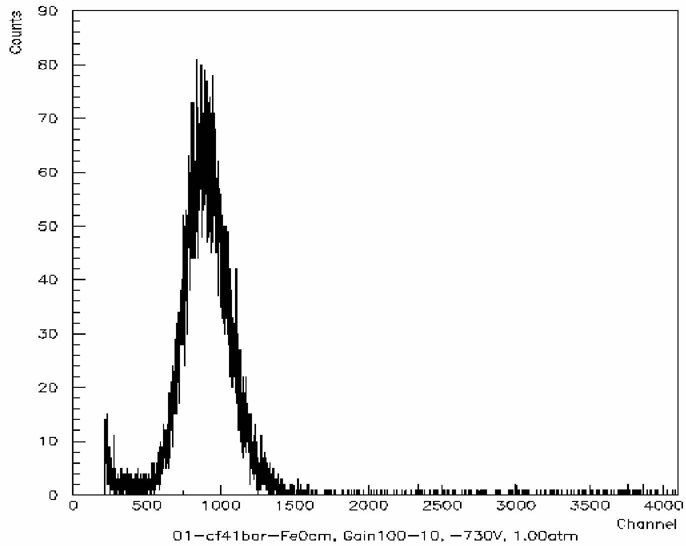

Figure 3.6: Pulse height spectrum in the grid for 5.9 keV X-rays, measured at 1 bar of CF_4 gas.

In figure 3.6, a typical Mn-K_α X-ray pulse height spectrum is shown, at atmospheric pressure of CF_4 and a drift electric field E_d = 200 V·cm^{-1}·atm^{-1}, with the same settings as the recorded event shown in figure 3.5. The gas gain is about 2×10^4

In reality, the ionization distribution is a Landau one as expected by the fluctuation in the number of electrons created in the conversion gap, with a long tail towards higher values of energy (channels). The tail of the Landau distribution is so much shortened that we consider the spectrum as a gaussian distribution. The shape of the pulse height spectrum looks like a gaussian distribution.

3.3 The gas purity

3.3.1 Gas analysis

A mass spectrometer is provided near the chamber to analyze the inflowing and the outflowing of the gas.

Before being detected, different kinds of ions generated in the "Balzer" spectrometer during the ionization process should be separated[4], according to their mass-charge ratio (m/e) [uma]. An example of a Xe(98)CF_4(2) gas analysis, after 1 day of circulation, is shown in figure 3.7. Impurities are visible.

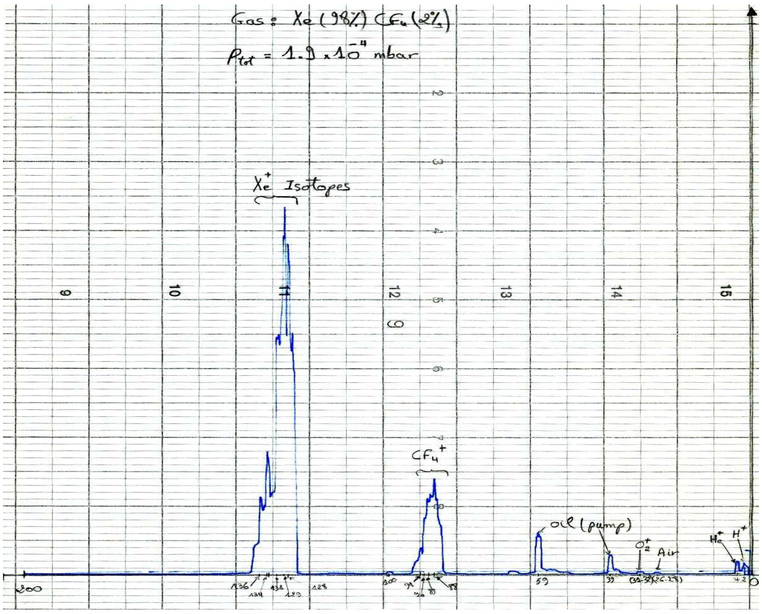

Figure 3.7: Typical spectra obtained with "Balser" mass spectrometer for Xe(98%)-CF_4(2%) gas sample.

The Xe concentration is higher than the CF_4 one as expected. Air and oxygen concentrations are considerably low, which is the case for all gas mixtures. The fragments 35 and 55 [uma] are hydrocarbons residues, released from the oil of the primary pump attached to the spectrometer.

[4] Steps are: *ionization, separation and detection.*

3.3.2 Varying the source position

At the same conditions (pressure, operating voltages, electronic settings) as in the figure 3.6, we measure the position and the pulse height of the spectrum at different source-cathode distances.

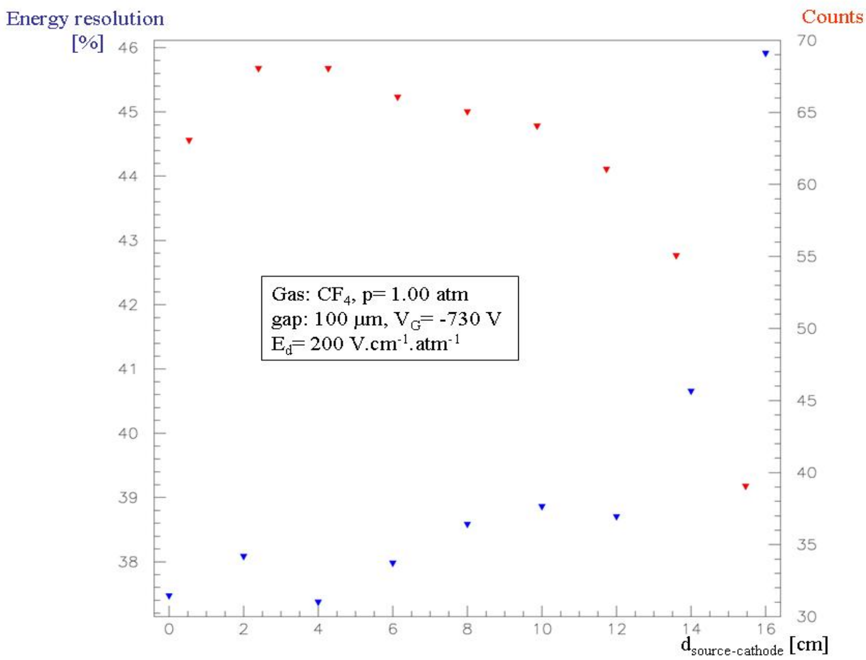

Figure 3.8: Plots of counts (red) and ^{55}Fe energy resolution (blue) as a function of the cathode-source distance.

The decrease of counts for large distances, when the iron source is near the detection plane, can be explained by the azimuthal coverage which is lower than the detector surface (< 9 cm). The interaction area of photons with the gas molecules is lower than the collection area. While, the maximum of counts is reached when the source is about $16 - 18$ cm far away from the grid . We expect that we have a full azimuthal coverage at this level of source position. The detection plane contains all the events generated by the ionization. Moreover, the energy resolution degrades with the source-cathode distance, while the number of counts decreases. This is explained by the fact that, firstly, the source disturbs the drift of electrons when travelling down and secondly the interaction area is smaller than the collected charge plane.

3.4 Voltage effect

When increasing the grid voltage, the spectrum is displaced linearly with the applied grid voltage. Counts at the peak-maximum decrease and the peak becomes larger but it keeps the same integral of the gaussian distribution, as shown in Figure 3.9.

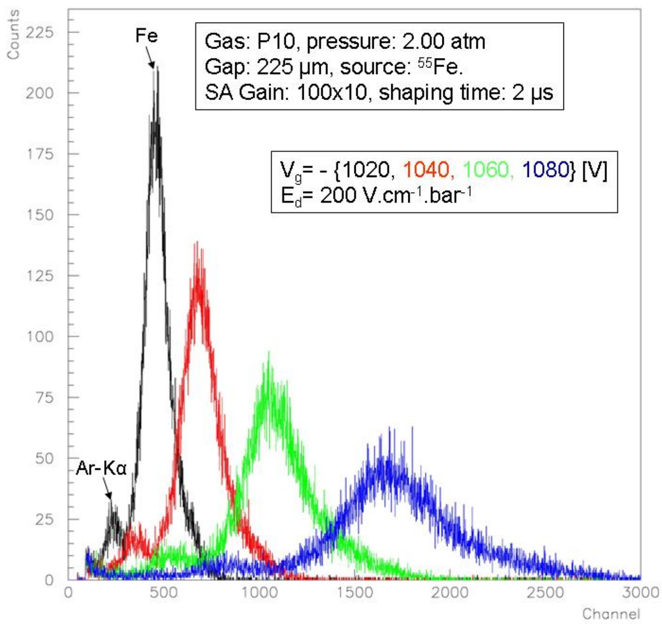

Figure 3.9: Voltage effect on the mean of the spectrum and its distribution.

The beginning of the charge collection, corresponding to the first appearance of the signal, means that the detector is operated in the "proportional mode" (see the appendix D.2). The collected charge is proportional to the incident gamma rays emitted by the source and the mean of the spectrum corresponds to the energy of the iron source.

The amplification field increases with the grid voltage and then, the collection efficiency becomes greater. The detector still operates in the "proportional mode". An exaggerated applied field leads to continuous discharges. The gain is saturated and the energy resolution is deteriorated.

The maximum voltage applied depends on the gap height, the wire elasticity, the grid opening and of course on the gas. Rare gases have lower operating voltages.

The highest applied voltage corresponds to the limit where discharges occur and the gas gain is saturated. The working region is the difference between the grid voltage (V_g) at the limit of discharges, corresponding to the highest reached gain, and V_g at the appearance of the pulse height spectrum.

The Ar-K_α peak in figure 3.9 is due to some energetic electrons emitting bremsstrahlung photons. These photons, when escaping, interact with the detector-edge and liberate electrons, which by their turn ionize the gas molecules.

3.5 Electronic noise effect on the energy resolution

Noise is an important problem when dealing with small signals: if the noise is large, the signal can not be visible. Thus, it is necessary to reduce the electronic noise as much as possible. Noise reduction can be obtained by setting up a common ground, put the electronic system as close as possible to the detector, use shorter cables ... More details on the electronic system are in the subsection 3.1.3.

The two spectra shown in figure 3.10 were recorded at the same conditions of pressure, voltages and electronic settings, in CF_4 gas, but with two different levels of electronic noise. The contribution of the electronic noise to the energy resolution is given by the right peak (pulser) of each picture.

With a low noise (the right plot), the energy resolution of the detector and the electronic resolution are about 38.34% and 1.81% respectively. Moreover, the tail of the electronic

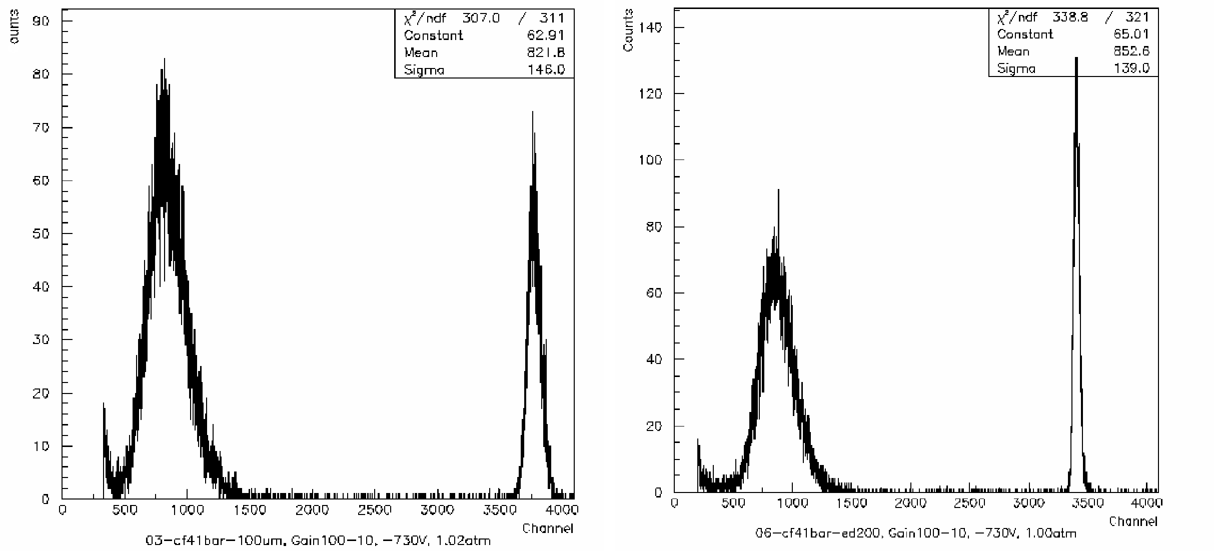

Figure 3.10: Pulse height spectra in the grid for 5.9 keV x-rays, measured at 1 bar of CF_4 gas, recorded with different levels of the electronic noise: higher (left) and lower (right).

noise distribution shifts to channel 430 at low energies. The slight displacement of the spectrum is due to the tiny difference between pressures: 1.00 atm in the case of low electronic noise and 1.02 atm for the higher level of electronic noise.

However, with a higher level of electronic noise (the left plot), the detector energy resolution reached is 41.74% and 3.32% for the electronic resolution.

With low level of noise, the working region extends from $V_G = -680$ V to $V_G = -790$ V and the tail of the electronic noise distribution is around channel 277. But with high electronic noise, the working region gets smaller ($-710 < V_G < -790$ V) and the energy resolution deteriorates with the electronic resolution.

3.6 The drift electric field choice

One should ask the question: why should I apply such a drift field and not a higher or lower values. To answer this question, some tests were done with different gases at various drift electric fields. As we know, when we increase the voltage between the cathode and the grid, electrons drift faster to the detection plane and diffusions decrease. But, each gas behaves differently.

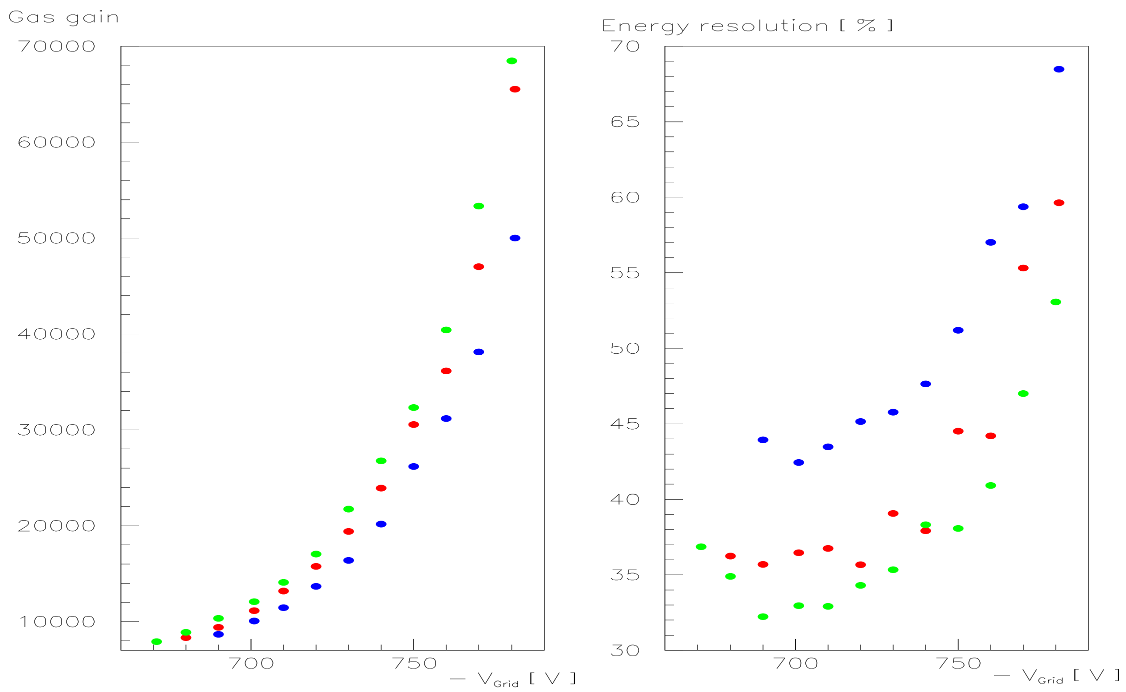

Figure 3.11: The CF_4 gas gain and the energy resolution in function of the grid voltage varying the drift electric field (E_d = {100 (blue), 200 (red), 400 (green)} [$V \cdot cm^{-1} \cdot atm^{-1}$]), at atmospheric pressure, with 100 μm gap and ^{55}Fe source.

The drift time is often inversely proportional to the drift electric field (see equation 4.3.1). The charge collection is therefore well favored and arises faster, if we apply higher electric fields. Lowering the electric field, results in an increase of diffusions and a loss of electrons by capture on impurities. The drift field is however limited by the total cathode voltage, which must be such that no HV breakdown occurs.

We are doing tests with CF_4, Xe(98)CF_4(2) and P10 gases operated with 100, 200 and 400 $V \cdot cm^{-1} \cdot atm^{-1}$ drift electric fields.

In the case of CF_4 gas, we collected the charge even with a low drift electric field (100 $V \cdot cm^{-1} \cdot atm^{-1}$). Figure 3.11 shows that we can achieve highest gains when increasing the drift electric field. The energy resolution keeps getting better at higher drift electric field (E_d = 400 $V \cdot cm^{-1} \cdot atm^{-1}$). This is explained by the fact that the free electrons produced in the conversion region take less time to drift to the detection plane and therefore the drift velocity is higher and diffusions are lower. In addition, ionization fluctuations become smaller and the energy resolution is better.

Other tests were done with the noble gases P10 and Xe(98)CF_4(2) mixtures.

Figure 3.12 shows that noble gases do not work at higher drift electric fields[5]. At lower drift field (E_d = 100 $V \cdot cm^{-1} \cdot atm^{-1}$), diffusions are high and electrons are lost. We expect that: when we rise beyond a certain drift electric field, we start exciting noble gas atoms. Lights emitted by the gas de-excitation, go to the cathode or to the edge of the chamber causing sparks.

One can see the effect of the CF_4 attachment on the energy resolution, if we compare CF_4 energy resolutions with those obtained by the P10. We obtain better energy resolutions with P10 gas.

At low electric field, the primary electrons have time to be trapped by electronegative impurities and a loss of the pulse causing a position dependence in the output pulse and a widening of the peak. Thus, the relative FWHM decreases sharply as the grid potential is increased until the losses are negligible. When the grid potential is increased, a weak tendency for a rise of the relative FWHM can be observed.

With P10 gas and at 100 $V \cdot cm^{-1} \cdot atm^{-1}$ drift electric field, ions prefer joining electrons to form pairs. Then, the collection is penalized because of recombination. Also with a Xe(98)CF_4(2) mixture, we hardly see the tail of the spectrum, because of the long time purification needed and high diffusions. In addition, the electric field is not high enough

[5]Sparks near the cathode were heard.

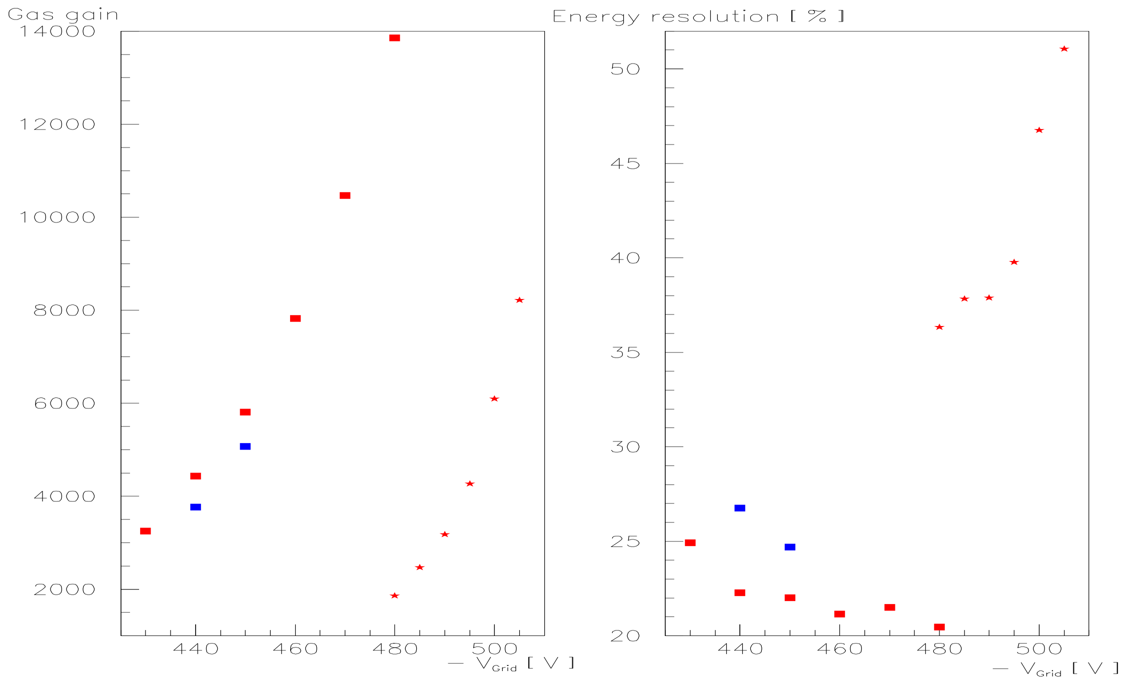

Figure 3.12: Electric drift effect (E_d = {100 (blue), 200 (red)} [V·cm^{-1}·atm^{-1}]) on the energy resolution and on the gas gain at atmospheric pressure, with a 100 μm gap and ^{55}Fe source in P10 (square) and $Xe(98)CF_4(2)$ (star) gases.

and the quality of ionization created through multiplication becomes sufficiently large that the space charge created distorts the drift electric field.

By increasing the voltage, the multiplication becomes higher so that a discharge occurs in the gas.

The choice of the drift electric field $\mathbf{E_d = 200\ V{\cdot}cm^{-1}{\cdot}atm^{-1}}$ is therefore well justified.

3.7 Pressure effects

Operation at higher pressures is needed to obtain efficiencies close to 100% and to compete with other techniques in spatial resolution.

Some tests were done to study the effect of the gas density on the energy resolution and

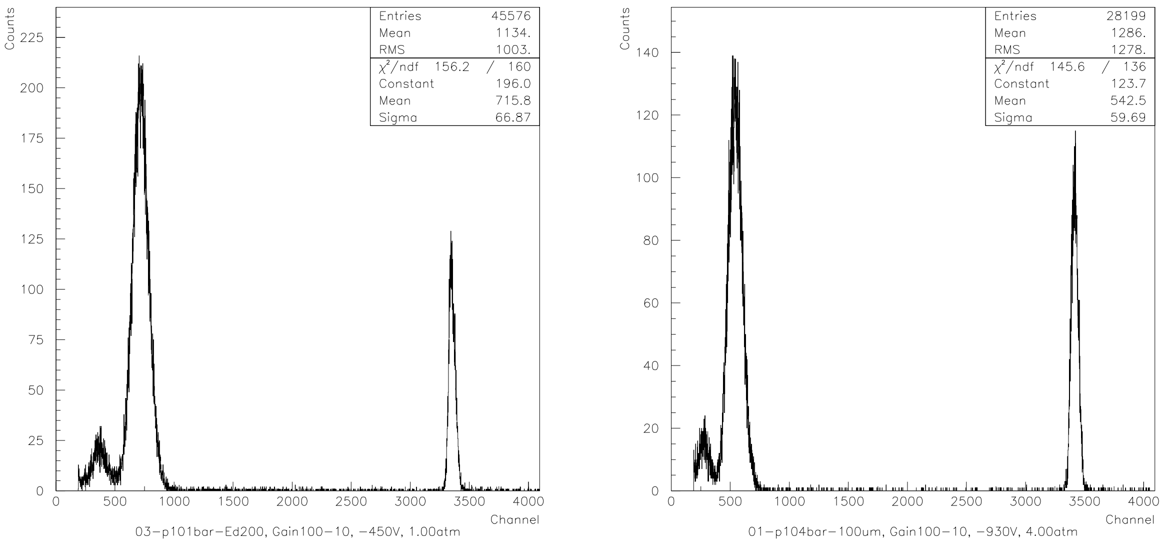

Figure 3.13: Gas density effect on the energy resolution in P10 gas at 1 (left) and 4 (right) bar.

within which limits the Micromegas detector is transparent.

As shown in figure 3.13, the energy resolution is slightly deteriorated by increasing the P10 gas pressure. If we compare two pulse height spectra at the same conditions (drift field, gap height, electronic settings ...), we can see that the energy resolution at 1 bar (22.02%) is slightly better than at 4 bar (25.82%) with gas gains 5808 and 5883 respectively. We conclude that the grid has approximately the same transparency at different P10 gas densities.

This is not the case for CF_4 gas, where the energy resolution is remarkably worse by increasing the pressure. The energy resolution at 1 bar is about 1.5 times better than at 2 bar, with approximately the same gains. Here, the reason is the CF_4 attachment effect. Figure 3.14 summarizes this effect.

At higher pressures, longitudinal diffusions are low and the detector efficiency is high. We go to higher pressure to accentuate the medium stopping power. But, the transverse width

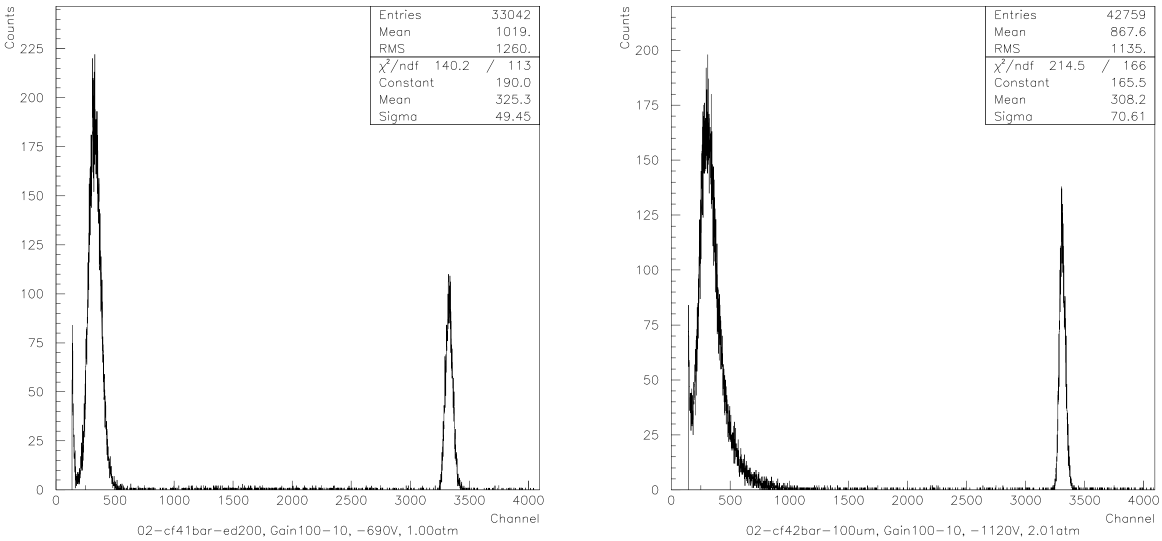

Figure 3.14: Pulse height spectra in the grid for 5.9 keV X-rays, measured in CF_4 gas at 1 (left) and 2 bar (right) pressures.

of the diffusion cloud increases with the gas density.

The pressure must be lowered, if lower energy electrons are to be investigated to keep multiple scattering low. This is the case of the detection of low energy neutrinos coming from the pp fusion and ^{7}Be reactions of the solar chain.

3.8 Gap effects

We have studied the dependence of the gas gain and the pulse height resolution of the Micromegas detector with *large drift volume* as a function of various gaps.

Since the drift distance is chosen long enough to go up to higher detector volumes, gap dimensions are also studied to select the best suited one. Good energy resolution and highest pressure are the most important parameters. Two different gaps were investigated: 75 and 225 μm at various gas pressures extending from 1 bar to the highest achieved pressure. Figure 3.15 shows measurements of the gas gain versus the grid potential obtained for the P10 gas at different pressures: $(1, 2, 3)$ bar for 75 μm and $(1, 2, 3, 4)$ bar for 225 μm gaps.

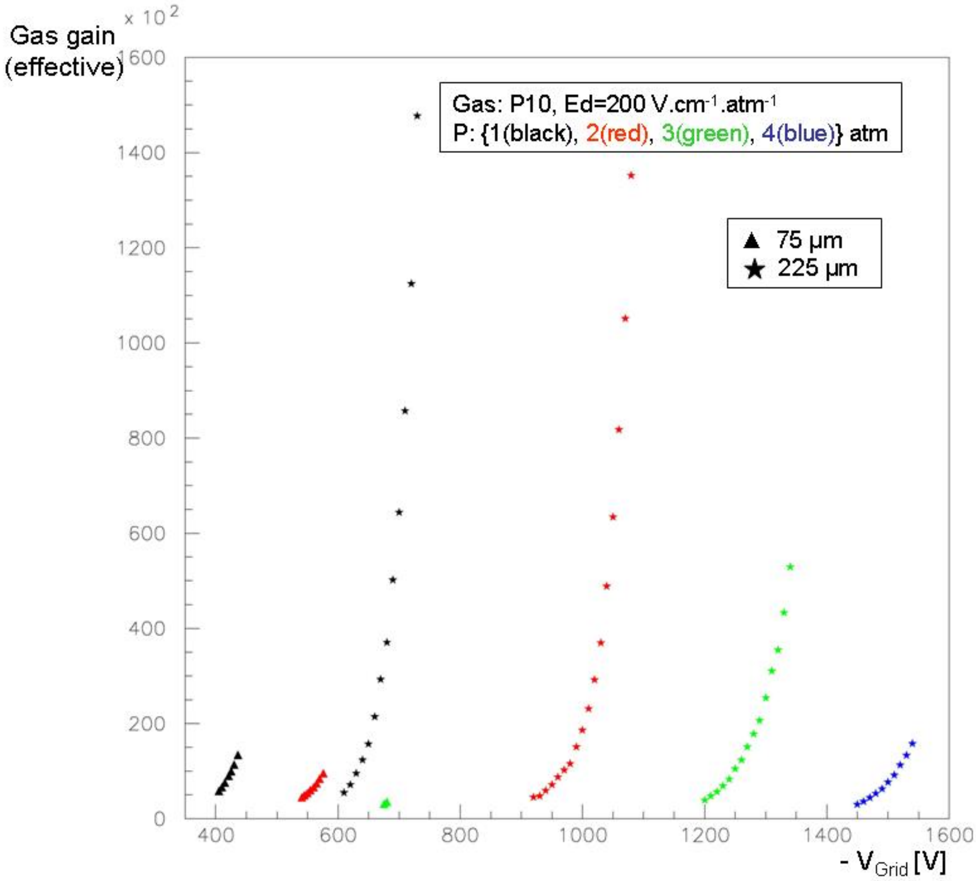

Figure 3.15: Gas gains measured in P10 gas, with 75 μm (▲) and 225 μm ($\star$) gap heights in different pressures as a function of the grid voltage, using a ^{55}Fe source and operated at a drift field of $E_d = 200$ V$\cdot$cm$^{-1}\cdot$atm^{-1}.

With a reasonable gap value (225 μm), gas gains greater than 10^4 are comfortably achievable. The maximum gain in each curve corresponds roughly to the maximum stable operating points, which is the limit for discharges. With a 225 μm gap, much higher voltages are needed to reach the same gain obtained by 75 μm, but the working region is larger. For example, at 3 bar of pressure, we have a working region of about 5 V with a 75 μm

of gap and 80 V with a 225 μm one. In addition, our limit of pressure is not caused by the grid working limit, but by sparks in the cathode plane. A remarkable fact is that the maximum achieved gas gain drops with pressure. The same effect was observed with a triple-GEM detector [49, 50], operated at different pressures of argon, krypton and xenon. The collection efficiency is higher with 75 μm gap, but the working region is smaller and we can reach the same gain as with a higher gap with a lower applied voltage. If we go up to higher gaps, we decrease the relative gap variations over the entire area. We insure gain uniformity in the avalanche region and we can achieve larger detection plane surfaces. This was our argument to choose a **250 μm gap** for the Gotthard-TPC detector.
The grid is transparent even at 4 bar pressure in the P10 gas. The operation-limit of the Micromegas at higher pressure of CF_4 is not due to the grid transparency, but is due to the electrons lost by CF_4 attachment. This can be explained by the working at higher pressure in P10 and Xe based mixtures.

3.9 Quencher effects

Serious studies of quencher effects and the choice of the convenient percentage, especially to reduce the percentage of electrons lost by CF_4 attachment and to favor the charge collection in Xe gas are presented in Neuchâtel-miniTPC results (chapter 5) and also in the section 4.3.

3.10 The gas choice

The gas mixture is an important and delicate choice for drift chambers. Gas molecules or atoms should have a high atomic number to yield the highest specific ionization. Low atomic number minimizes the multiple scattering and allows for the reconstruction of the electron direction. The gas molecules should give low diffusions, in order to provide good position resolution even for the largest drift distances[6] and should be fast. CF_4 has small diffusion coefficients as shown in subsection 4.3.2.

The rapidity of the drift velocity translates into a short collection time and a small longitudinal diffusion [51]. The fastness of CF_4 gas plays the same role as the magnetic field. As we know, the magnetic field has no effect on the longitudinal diffusion, but it decreases the transverse diffusion.

The gas should also have a high density to maximize the number of target electrons. For example, the density of CF_4 is 3.68 g/l at 1 bar and 15°C temperature, which gives a very high electron density of 1.06×10^{21} cm^{-3}, this is why we obtain higher gains.

We need the conditions in which the voltage is the smallest for necessary gas amplification. This is attainable if we use rare gases: they are usually chosen for their minimum working voltages.

Gas mixtures are also chosen for their extremely low aging (with small hydrocarbon concentrations [52]), their spark resistance, good electrical properties, good chemical properties[7], the low cost and ease of use. It should be stable and insensitive to small impurities, which is not the case for xenon gas.

3.10.1 Why Xenon ?

Xenon offers an excellent stopping power, given its high density (3 g/cm^3, at 300 K) and high atomic number (54). Detectors filled with xenon insure a high event rate and therefore increase the cross-section, which is proportional to A^2.

The ^{136}Xe isotope acts as the source and the target at the same time, in the case of the double beta decay search. It has a high scintillation and ionization yields. Moreover, the only double beta decay of the ^{136}Xe into a short-lived radioactive isotope ^{136}Ba strengthens xenon as a good candidate.

[6] more than a few cm.

[7] no flammable and no poisonous.

Xenon is a mono-atomic molecule, so nothing can decompose and there is non-ageing, which is important for very long experiments.

Xenon can be continuously purified of chemical and radioactive contaminants.

Xenon is an efficient UV scintillator (175 nm), which helps to go to low visible energy threshold.

Because of the high diffusion in xenon, the electron is completely lost. We see just a part of the track of low energetic electrons. This is why, xenon is not good for solar neutrino detection, but the best for double beta decay search.

3.10.2 Why CF_4 ?

CF_4 gas, called usually fast gas, has a high electron density .

Its low Z means low multiple scattering, which leads to better tracking. The absence of high Z elements decreases the multiple electron scattering as well as the distortion of its trajectories.

In addition, CF_4 is a scintillator, which emits light in the region from ultraviolet (near 160 nm) to the visible light. The primary scintillation photon yield of CF_4 is about $16(\pm 5)\%$ of that of Xe [53]. Light signals registered by MUNU-experiment photomultipliers are good prove for CF4 scintillation emission. Figure 5.7 shows PM's switched on by the CF_4 light. Despite its high electronegativity causing serious electron lost and its ageing, the CF_4 gain can reach 10^6, because of its high electron density and its elevated drift velocity. It was operated in several detectors. A 10^6 of gain was reached with **triple**-GEM based detector in pure CF_4 [54]. It was operated with a MWPC [55]. CF_4 was used as gas filling of MUNU experiment [10, 56], and the tracking capability and final results on the electronic neutrino magnetic moment, proved the adequacy of this gas.

3.10.3 The choice of the quencher

We add quencher not only to decrease operating voltages and avoid the necessity of using exaggerated potentials across the grid, but also to reduce the attachment and be useful and convenient for rare event detection.

In pure noble gases, the electron drift velocity is relatively small and the diffusion is large. Adding 2% of CF_4 to Xe, can increase the time collection and reduce diffusions. Results given in the section 4.3 can confirm this.

We can obtain higher gains with a tiny quantity of additives as shown in the section 5.2.1.

Chapter 4

Electric field configurations and electron transport properties

To understand well the measurements presented above and to know the influence of parameters before choosing them, we are doing simulations using Maxwell, Garfield, Magboltz and Heed packages, described in Appendix E.
Computations can be favored by priority and need. So, electric field configuration inside the detector and near the amplification zone is the first simulation to do. Secondly, we can plot drift electron lines and the feedback of ions. On the other hand, we studied electron transport properties in the gas and under applied electric fields. Finally, we can estimate the muon energy loss crossing the gas molecules.
Because of its large volume, the TPC needs fast drift velocity, low diffusions and a high energy loss (dE/dX), to ensure best tracking and particle identification.
All simulations are done by using measured values, such as geometric structure, pressure, temperature, applied voltages ...

4.1 Electric field configurations

Much of our work was dedicated to develop a new TPC with a *large drift volume*, based on a Micromegas detection plane, which replaced the MWPC installed before in the Neuchâtel-miniTPC prototype and in the Gotthard-TPC detector. Thus, simulations of the new electric field configuration are essential, especially near the collection zone.

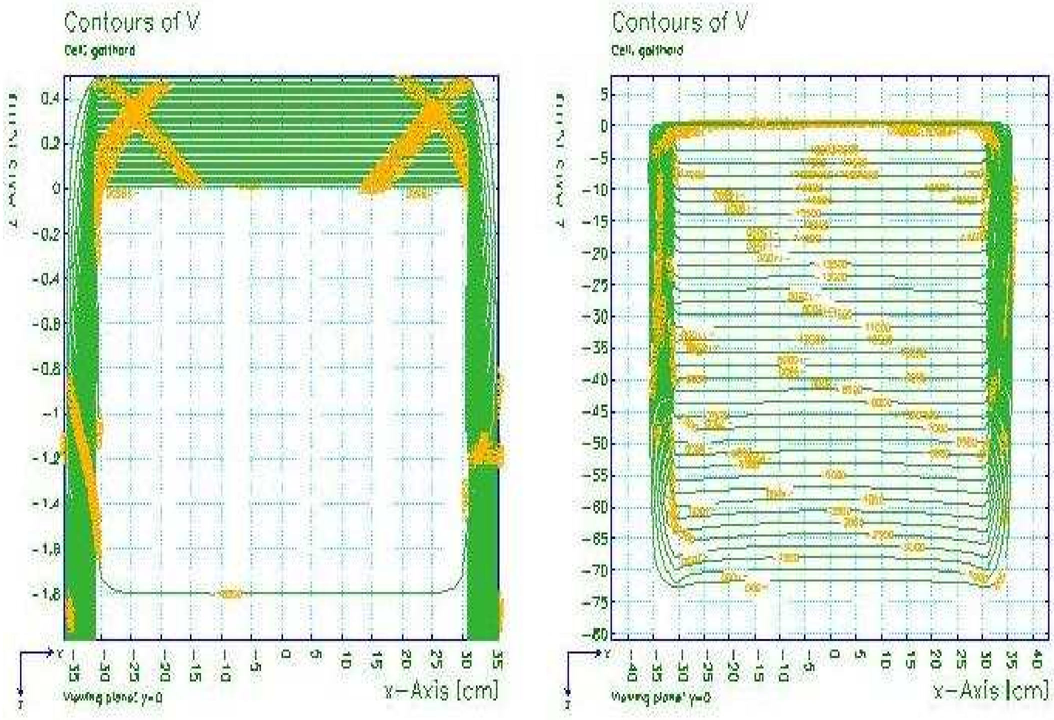

Figure 4.1: The electric field configuration inside the Gotthard TPC (right) and near the the detection plane (left).

The geometry of the detector, in the Neuchâtel-miniTPC (see figure 3.1) or in the Gotthard TPC (see figure 6.1) is the same. Only the volume is different: 20 l for the miniTPC and 180 l for the TPC. We gave priority to simulate the electric field in the Gotthard TPC, closer to real detectors for rare event detection (the largest possible).
Calculating the electric field maps inside the TPC needs "Maxwell 2D field simulator". We started by drawing explicitly the geometric structure (units, dimensions, electromagnetic properties ...) of the Gotthard TPC, thanks to its "simple" design, and specified all relevant material characteristics (dielectric or conductor), boundary conditions and sources. We

exploited the axial symmetry of the TPC and the periodicity of field shaping rings and insulators between them.

Then, Maxwell generated the necessary solutions, called "field maps" and after, Garfield read these files. Results of electric field calculations are presented in figure 4.1.

The electric field is perfectly uniform near the detection plane and in the conversion region. Distortion of the electric field near the cathode (the bottom of the right picture) is due to a dimension mistake (distance between the cathode and the TPC-edge).

4.2 Field lines and ions-feedback

We also studied the behavior of electrons when drifting to the detection plane and ion feedback to the drift zone. The 2D configuration of Garfield was used for these simulations.

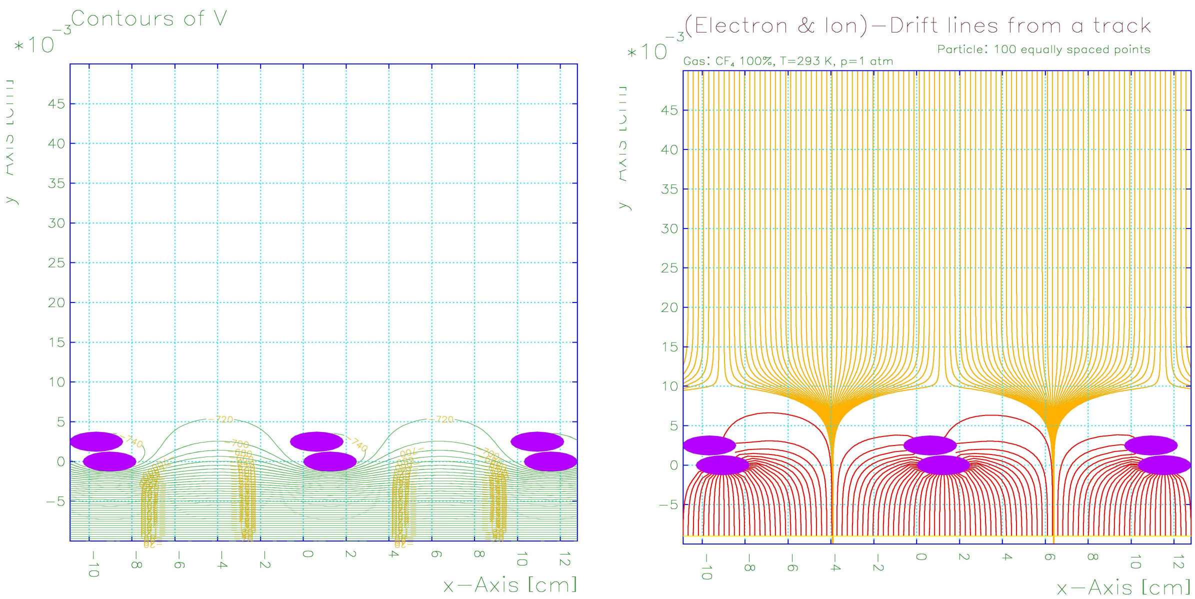

Figure 4.2: Electric field configuration (left) and (electrons (yellow) & ions (red)) drift lines (right) simulated in a clothed grid. The X axis is scaled by a factor 10^{-5}.

Normally, the chamber has a 3D form, but it can be locally approximated to good precision by 2D cuts. The 3D computations of two crossed wires in the micromesh grid are simplified to superposed circles, with 20 μm of diameter. One of them is put back to the other in Y axis. The wires are repeated every 53 μm, which corresponds to the opening of the grid. Results of Garfield simulations are presented in figure 4.2.

The left figure shows that the electric field is homogeneous in both the conversion and the amplification region. But, there is like a bulge in the opening of the microgrid.

In principle, the field lines between the holes should be homogenous to insure a very good energy resolution, but in reality, homogeneity in this region has never been reached because of the potential difference in this drift-amplification frontiers.

An incompletely stretched grid can distort more the electric field in the grid openings. The flatness of the grid is also a major factor, which contributes to the homogeneity of the gap region and the energy resolution.

Space charge of positive-ions, feeding back to the drift volume, destroys the field near the head of the avalanche and generate sparks. In the case of the Micromegas structure, the ratio between the amplification and the drift electric fields exceeds 250 for all gas mixtures in our tests. This value is sufficient to permit a full electron transmission, to explain the intrinsic ion feedback suppression and to favor the total charge collection (see the left picture of figure 4.2).

The charge signal is mainly due to the positive ion drifting to the micromesh grid. So, the ion feedback to the cathode should be completely suppressed. These simulations are confirmed by the detector response in figure 3.5, where the response time, at 1 bar of pure CF_4 gas, is of about hundred ns. This rise time allows to catch-up the fully induced charge.

The uniformity of the electric field insures parallel drifting of electrons, moving on tracks, and the constancy of their velocities. Note that, in our calculations, we did not take into account gas properties (diffusions, attachment...).

The advantage of the Micromegas structure is that the electric field near the anode is very homogenous. On the other hand, the equipotentials are almost circular in the case of the

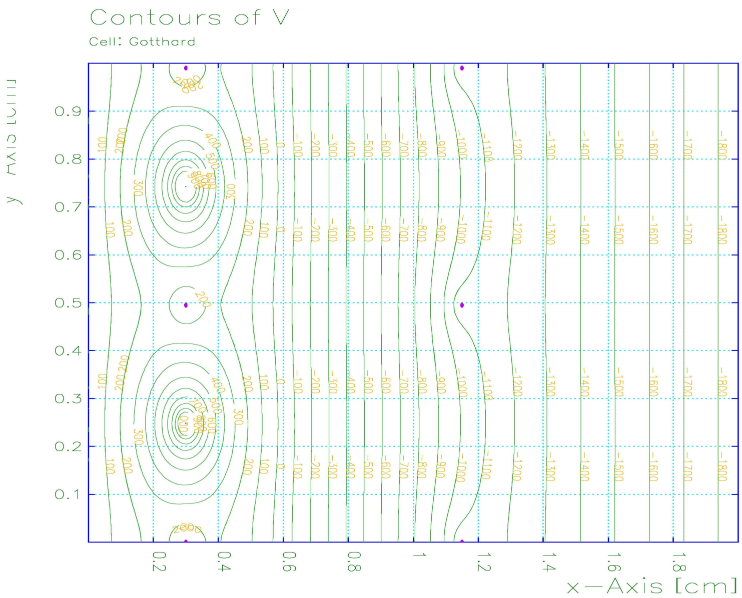

Figure 4.3: The electric field configuration near the MWPC plane with Gotthard voltage settings. The TPC was operated with 5 bar of Xe(95)CH_4(5).

MWPC wires, as it is shown in figure 4.3. The field lines near the anode wires bend toward the wires, the charges are drawn towards the anode wire. This phenomena worsens the resolution and degrades the efficiency of the detector.

4.3 Electron transport properties in the gas

The behavior of electrons must be well understood by studying the electron drift velocity, transverse and longitudinal diffusions, the amplification and the attachment. Magboltz interfaced to Garfield, showed its capability to do all these simulations.

4.3.1 The electron drift velocity

Drift gases are characterized by the electron drift velocity. When drifting through the gas volume, the electron cloud at a position (x_0, y_0, z_0) is smeared out in space due to diffusions.

It depends on gas properties (atomic number, cross sections[1]) and applied electric field.

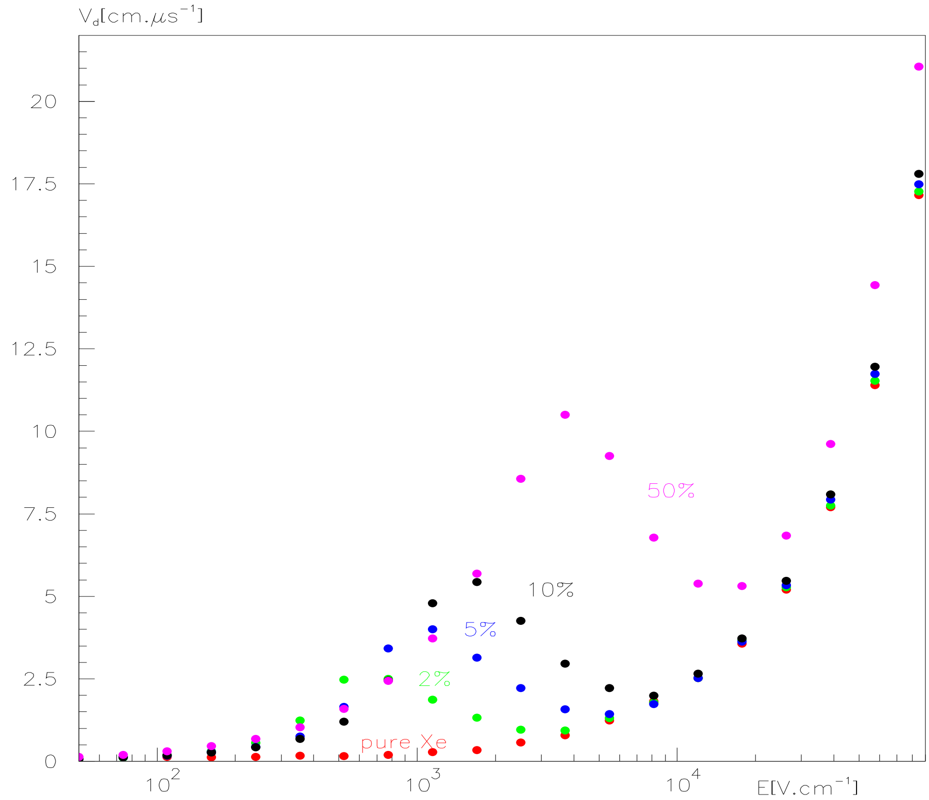

Figure 4.4: Dependance of the electron drift velocity on the electric field for (0, 2, 5, 10 and 50)% of CF_4 contents in Xe, calculated using Magboltz interfaced to Garfield.

With a high drift velocity (as in CF_4 gas), we can avoid losses due to the dead time and collect charge faster and diffusions are low.

The electron drift velocity in CF_4 gas is high even under low electric field. This gas is used with long or even very long drift distances.

In figure 4.4, we present the calculated drift velocities for different CF_4 percentages in Xe admixture at atmospheric pressure and ambient temperature. The drift velocity of

[1] Elastic, ionization, vibration, excitation, attachment ...

electrons in pure Xe is much smaller than in Xe(98)CF_4(2) gas mixture. We clearly see the effect of the fast gas (CF_4) on the drift velocity of electrons in Xe. This latest, increases with the CF_4 percentage. So, mixtures containing CF_4 gas look most promising.

A good agreement between simulations and measurements of the drift velocities for CF_4 (0, 5, 10)% added to Xe gas are cited in reference [57], and a comparison with the same proportion (10%) of CH_4 and CO_2 in Xe, confirmed that the measured drift velocity is the highest when adding CF_4 gas to Xe.

Measuring the length of muon pulses crossing the TPC from the anode to the cathode gives an idea about the drift velocity.

Obviously, high energy muons produce a straight track through the TPC, if vertical muons are selected, and measurement of the drift velocity from the pulse length of through-going cosmic muons is possible.

Measuring the drift velocity by the muon method using the miniTPC prototype is very encouraging, because the muon flux is high enough to have good statistics. In the Gotthard-TPC, where the muon flux is very low (attenuated by a factor 10^6), this method is excluded.

The drift velocity of electrons can be expressed as:

$$V_d = \mu \cdot E_d,$$

where, μ is the electron mobility and E_d is the applied drift field.

So the drift time can be derived:

$$t_d = \frac{d}{V_d} = \frac{d}{\mu \cdot E_d}, \tag{4.3.1}$$

where, d is the drift distance.

If the drift velocity is higher when adding CF_4 to the Xe gas, the drift time of electrons will be faster and the <u>*time resolution*</u> will be better.

The dependence of the drift velocity on the electric field, using the muon method, have been studied in reference [58].

4.3.2 Longitudinal and transverse diffusions

Diffusion is significant for large distances to the detection plane, this is why we should give importance to this factor and try to decrease its contribution. Adding fast gas to xenon decreases transverse and longitudinal diffusions.

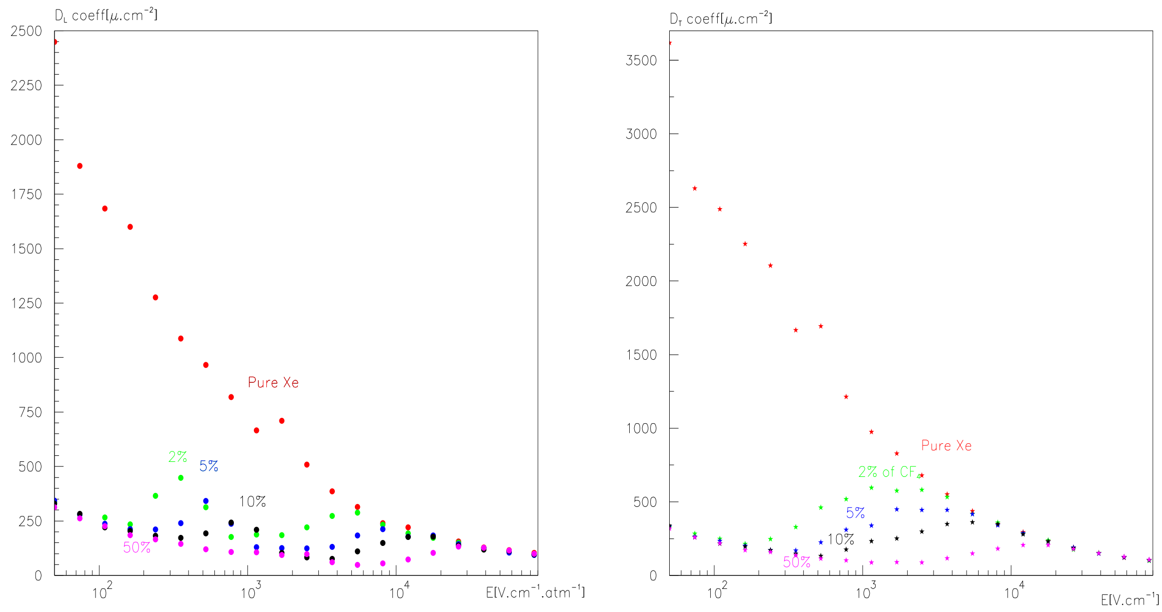

Figure 4.5: Electron longitudinal (left) and transverse (right) diffusions versus the electric field for pure Xe (red) and 2% (green), 5% (blue), 10% (black) and 50% (pink) of CF_4 admixtures.

During the drift, electrons and ions diffuse by multiple collisions. Low drift velocity and high diffusions spoil the *position resolution*.

The spatial resolution is good when a low transverse diffusion gas, like CF_4, is used [59]. The good tracks recorded by the MUNU experiment (see figure 2.3) using pure CF_4 gas is a clear argument.

As it is shown in figure 4.5, diffusions are high in pure Xe. This last can reach more than 1000 of micron for 1 cm of drift. Adding a small quantity of the CF_4 gas decreases rapidly

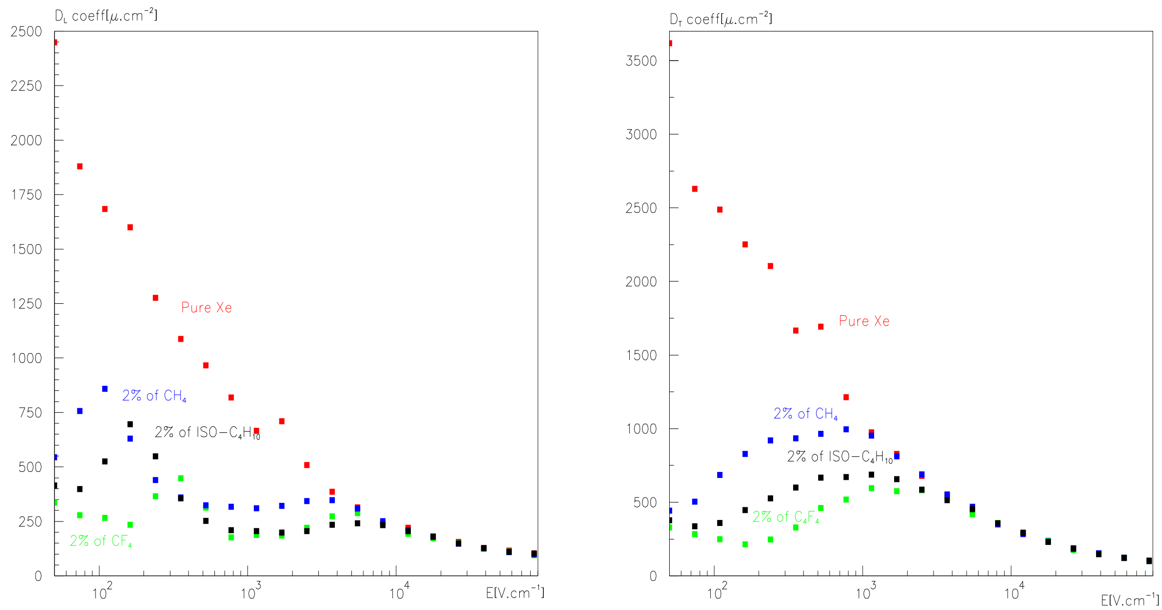

Figure 4.6: Electron longitudinal (left) and transverse (right) diffusions versus the electric field for pure Xe (red) and 2% of CF_4 (green), CH_4 (blue) and iso-C_4H_{10} (black) admixtures.

diffusions by a factor 10.

Let us compare with other admixtures, considered as good quenchers for Xe: iso-C_4H_{10} and CH_4 gases. Keeping the same percentage of the additive (2%), diffusions are lower with CF_4 admixtures than with CH_4 and iso-C_4H_{10}, as summarized in figure 4.6. Indeed, the smaller cross sections of CF_4 compared with iso-C_4H_{10} and CH_4 (see appendix F), contribute to higher drift velocities for the CF_4 mixtures and therefore, explain the small diffusions. As mentioned in reference [37], the drift velocity is high when electrons are slowed into an energy region when the mean scattering cross section "$< \sigma_{sc} >$" for the gas is small, which is the case for the CF_4 gas.

CF_4 gas showed its capability even by increasing electron drift velocity or decreasing transverse and longitudinal diffusions in Xe gas.

Fast gases can replace the magnetic field, which reduce diffusions by a great factor.

4.3.3 Townsend and attachment

The avalanche process is described by the number of ionization collisions per unit length, called the first Townsend coefficient "α".

Molecules with electronegative atoms, such as CF_4, containing fluor with the highest electronegativity, attach free electrons to form negative ions or to neutralize an ionized molecule as follows:

$$\mathrm{CF_4 + e^- \rightarrow CF_4^- + h\nu}$$

$$\mathrm{CF_4^+ + e^- \rightarrow CF_4}$$

The presence of the negative ions CF_4^-, diminish the efficiency of the detector by attaching electrons and inhibit ionization, especially in the amplification zone, where the electric field is high and attachment is enhanced.

The attachment in CF_4 gas precedes amplification, destroys energy resolution and detector efficiency. At higher voltages, the resolution is worst because the attachment is enhanced. One can minimize this effect by optimizing the grid voltages, which is possible when adding noble gases or changing the MWPC wires by the Micromegas structure. Detailed studies of CF_4 attachment are shown in subsection 5.2.2.

4.4 The effect of the pressure on the energy loss

We let the Heed code simulate to calculate the effect of the pressure by running an input file through Garfield.

Heed is used by Garfield to simulate the energy deposited in the gas medium, created by the passage of minimum ionizing particles, such as muons.

Figure 4.7 shows the results of the most probable energy loss in 1 cm of CF_4 gas at different pressures for muons with energies ranging from 100 MeV to 100 GeV. The Bethe-Bloch [60] type behavior is clearly visible.

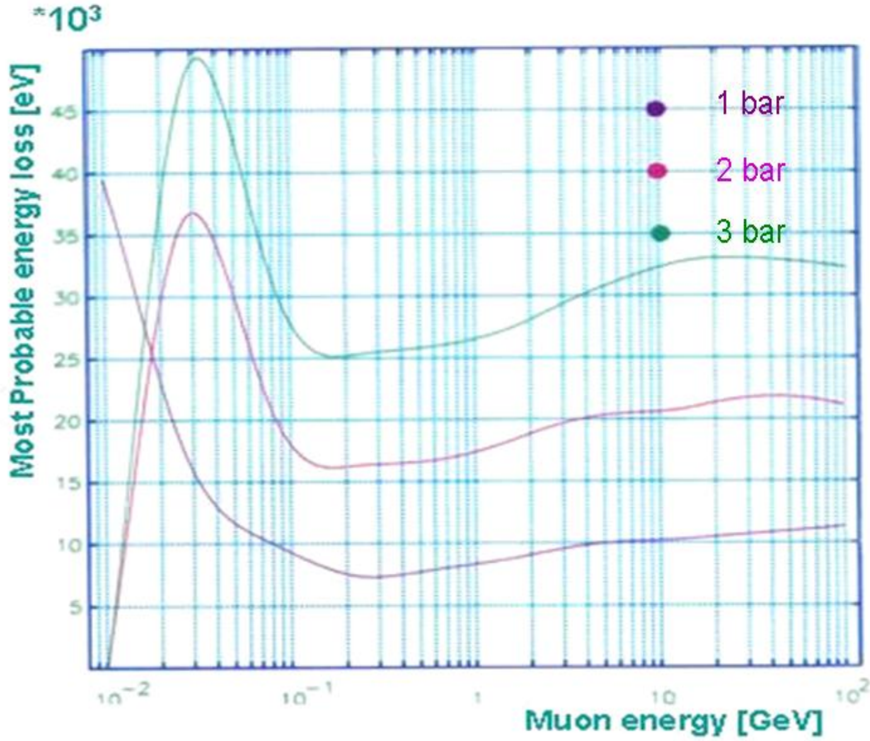

Figure 4.7: Energy loss as function of the muon energy for 1 (bottom), 2 (medium) and 3 (top) bar of CF_4 gas.

The most probable energy loss increases with pressure.

The energy loss of the charged particle by ionization is proportional to the density of the traversed medium. This is why, we try to increase the pressure or, in some cases, we use liquid or solid detectors.

Neuchâtel-miniTPC results

Chapter 5

New gas mixtures suitable for rare event detection using a Micromegas-TPC detector

Abstract

The aim of the work presented here was to develop new techniques based on a Micromegas-TPC, in order to reach a high gas gain with good energy resolution, and to search for gas mixtures suitable for rare event detection.

The gas gain and the energy resolution have been evaluated with low energy sources (^{55}Fe and ^{241}Am) in Xe-CF_4 gas-mixtures. High gains are obtained, with good uniformity and energy resolution.

This chapter focuses on the quenching effect by studying charge collection in xenon, which is convenient for the search of neutrinoless double beta decay in ^{136}Xe isotope. Conversely, a small admixture of xenon to CF_4 can reduce attachment in the latter: Overall this gas mixture would be suitable for dark matter and solar neutrino search.

5.1 Introduction

The gas medium is one of the most important components, determining good electron drift. The choice of the gas is therefore crucial to obtain a high amplification and a good energy resolution.

In the framework of the EXO [17] collaboration, we studied the charge collection in Xe gas and electron transport properties, seeking a suitable gas mixture for neutrinoless double beta decay in ^{136}Xe, if the gas version is chosen.

Moreover, the tracking capability of the MUNU detector, operated with pure CF_4 gas, and the good results obtained with this gas (the best limit of the electronic magnetic moment [10]), encouraged us to optimize the TPC detector by reducing the CF_4 attachment. This gas could be used for solar neutrinos and dark matter search.

For these reasons, we investigated the performance of a Micromegas-TPC detector filled with Xe-CF_4 gas mixtures at atmospheric pressure, going from a weakly added Xe with CF_4, to a version using CF_4 only.

All tests presented in this chapter, were done with the miniTPC prototype, with a 18 cm drift length and various amplification heights of the amplification region. The diameter of the Micromegas anode plane is 9 cm. A full description of the miniTPC prototype and the Micromegas detection plane is given in the section 3.1.

5.2 Main results

We measured pulse height spectra obtained from grid signals. Charge spectra are recorded for each gas mixture at different proportions of the additive, exposing the Micromegas detector to a ^{55}Fe source or to an ^{241}Am one. The acquisition time is maintained 100 s for every test.

Results have been carried out at atmospheric pressure for the majority and the drift field has been maintained constant during measurements at 200 $V{\cdot}cm^{-1}{\cdot}bar^{-1}$.

Before starting each test, we pumped out the set-up and the miniTPC down to 10^{-6} mbar. Moreover, common impurities (O_2, H_2O, CO_2 ...) are efficiently removed via the gas purification system.

To maximize the signal, the voltage on the grid had to be lowered a few volts below to the limit of the breakdown. The Micromegas is robust and stands sparks, recovering nicely after voltage is reduced.

In our work, we are interested to study the energy resolution of the detector at low energies and determine the gas gain with different gas mixtures, essentially in Xe-CF_4. Therefore, we should give how we determine the gas gain and the energy resolution:

- The gain of each gas mixture was measured by comparing the peak of the pulse height distribution generated by X-rays (^{55}Fe or ^{241}Am sources) with a charge calibration generated at the input test of the charge sensitive preamplifier.

  Referring to the equation 2.2.3, the collected charge on the grid represents the total number of ions created after the amplification and is equal to CV, where C is the input capacitance of the preamplifier and V is the voltage corresponding to the source calibrated with the input test of the preamplifier. Thus, the gas gain is given by this relation:

$$G = \frac{CV}{eE/W_i}, \tag{5.2.1}$$

- The relative intrinsic energy resolution of each ionization is given by:

$$R_E = \frac{\Delta E}{E}, \tag{5.2.2}$$

  where ΔE is the full width at half maximum of the energy response and E is the maximum energy deposit.

  In these results, the electronic resolution is neglected because the electronic noise is considerably low.

5.2.1 Favoring the charge collection in Xe

a. Gas gain and energy resolution in Xe-CF_4 admixtures using a ^{55}Fe source and 100 μm gap height

As a first step, we are doing some simulations (see 4.3), to study the effect of the CF_4 gas as an additive on the electron transport properties (drift velocity, diffusions ...) to the xenon as a main gas. Comparisons with other quenchers were also made. Calculations proved that CF_4 has the highest drift velocity and lowest longitudinal and transversal diffusions, compared with iso-C_4H_{10} and CH_4.

The excited ions $(Xe^*)^+$, emitted by first ionization, can emit a flash of fluorescent light. CF_4 addition to Xe does not mean absorb the UV light emitted by the excited ion, because the "Penning effect" in this case is not favored.

Although, the ionization potential of CF_4 (15.9 eV) is remarkably higher than the excitation energy of Xe (8.4 eV), we can obtain higher gains because we increase the drift velocity and we decrease fortunately diffusions as shown in figure 4.4 and 4.5. Therefore, adding CF_4 to Xe is possible.

Based on these simulations, we have done experimental tests studying the gas gain of Xe-CF_4 gas mixtures, going from 2% of CF_4 to fifty-fifty of the main gas and the additive. A comparison with 2% of Iso-C_4H_{10}, known as the best quencher for Xe, is also done.

We summarized in figure 5.1 the effective gas gain curves and energy resolutions at 6 keV of energy, obtained in various gas mixtures as a function of the grid voltage.

Gas gains are large enough to allow the detection of signals in the ionization mode on the Micromegas-TPC.

We can that one must increase the grid voltage with the proportion of CF_4 gas. Usually, the addition of the quencher gas is used to decrease the operating voltage and to increase the gain amplification, which is contrary in the case of the Xe-CF_4 admixtures.

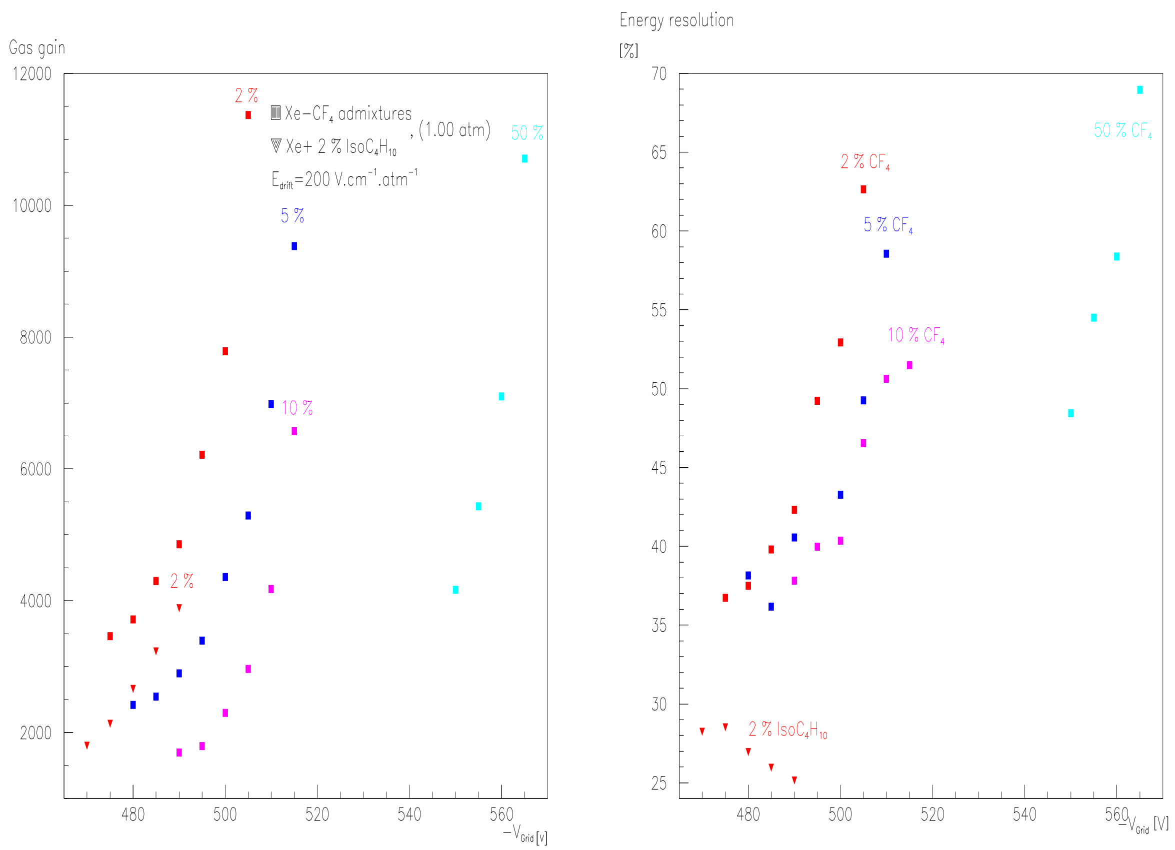

Figure 5.1: Gas gain measurements (left) and ^{55}Fe energy resolutions (right) versus grid voltages, with Xe-CF_4 (■) and Xe-IsoC_4H_{10} (▲) admixtures at atmospheric pressure and 100 μm gap.

The effective gain of the gas successfully exceeded 10^3 for all Xe-CF_4 gas mixtures. Moreover, the integrated signal current was measured with a nano-ampermeter and it is very small (few hundreds pA).

A remarkable fact is that if we put 2% of CF_4 to Xe gas, we observe that we obtain higher gains with lower operating voltages. Good agreement is seen with simulations (see figure 4.6).

The lowest gain at a higher percentage of CF_4 quencher, can be explained by the loss of

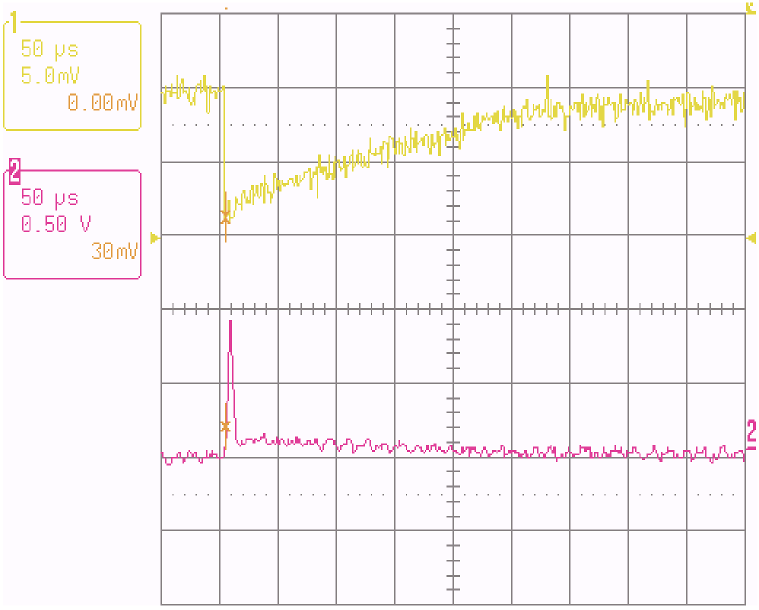

Figure 5.2: The shape of the preamplifier output (yellow) and the spectroscopic amplifier (pink), recorded in the scope for Xe(98)CF_4(2) gas mixture at 1.00 atm and −470 V on the grid voltage.

electrons, which inhibits the ionization in the avalanche region.

A typical preamplifier response of ^{55}Fe X-rays in the Xe(98%)CF_4(2%) gas at 1.00 atm, is shown in figure 5.2. The rise time is around hundred ns for this event. In addition, the shaping of the signal, allows to catch-up the fully induced charge.

The energy resolution of Xe(98)CF_4(2) admixtures is in the range of (35 - 65)% in the working region, compared with (25 - 29)% with Xe(98)iso-C_4H_{10}(2) (see the right of figure 5.1).

However, the poor energy resolution (around 37% at 6 keV) compared with the same proportion of iso-C_4H_{10} quencher added to Xe (27%), the Xe(98)CF_4(2) admixture gives higher gas gain (1.4 times better) at the same grid voltage ($V_g = -480$ V) with same settings and conditions, as summarized in figure 5.3.

Plots presented above confirm the CF_4 attachment effect on the deterioration of the energy

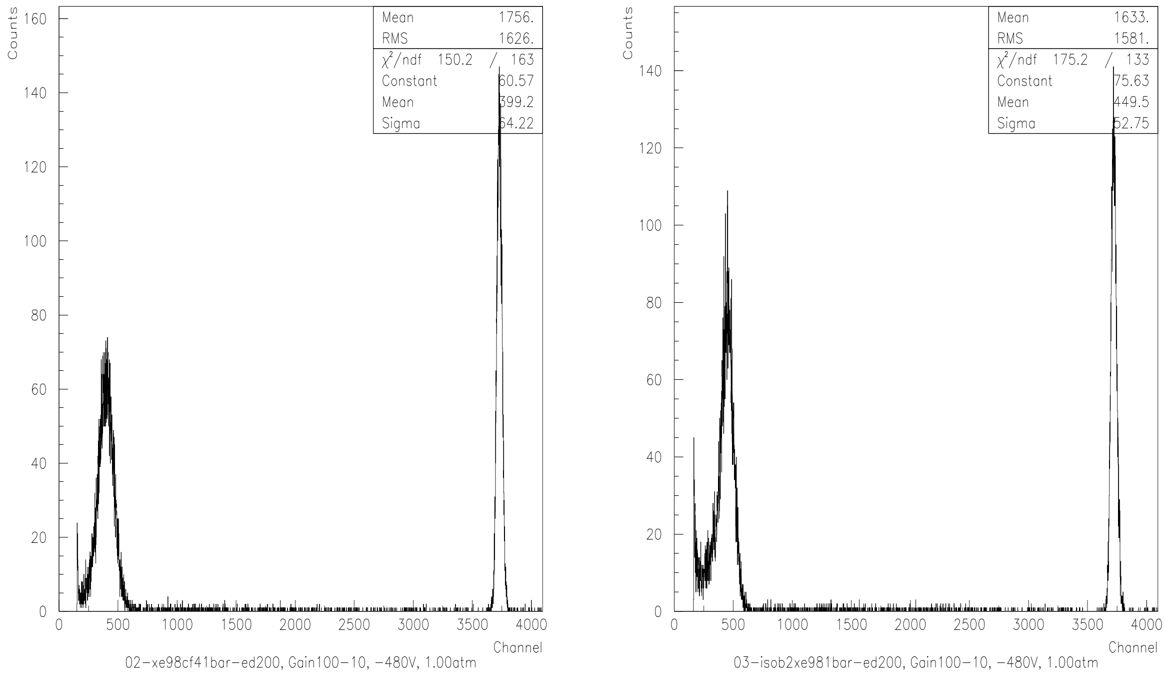

Figure 5.3: ^{55}Fe pulse height spectrum in Xe-CF_4 (left) and in Xe-isoC_4H_{10} (right) gas mixtures at the same proportion (2%) and the same settings, tested in the miniTPC at 1 bar of pressure.

resolution and at the same time proved the effect of the fastness of this gas on the charge collection. In addition, its high electron density (3.68 g/l at atmospheric pressure and ambient temperature), compared with iso-C_4H_{10} (2.67 g/l), also explained the higher gains obtained with the foremost.

As mentioned above, detailed studies have shown that it is possible to obtain higher gains with poorly mixed gas.

b. Gas gain and energy resolution in Xe(98)CF_4(2) gas mixture using an ^{241}Am source and 225 μm gap

These tests were done in the miniTPC with a 225 μm gap height, replacing the iron source by an ^{241}Am source facing the cathode copper plane. The choice of the gap dimension is based on results obtained in section 3.8. The gas mixture Xe(98)CF_4(2) is also chosen according to results obtained in the last subsection.

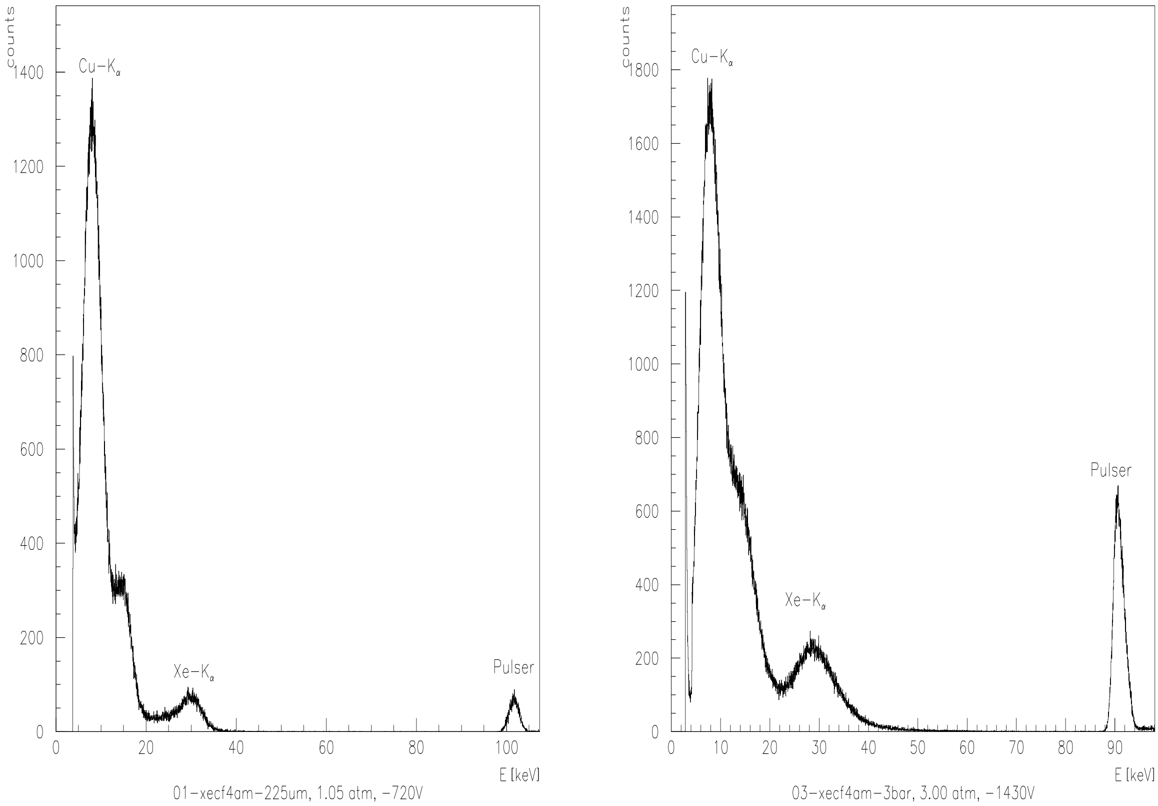

Figure 5.4: Pulse height spectra in the grid, measured in Xe(98)CF_4(2) admixture at approximately the same gas gains at 1 bar (left) and 3 bar (right) with 225 μm gap.

The Cu-activation (8.05 keV) and the Xe-K_α transition (29.779 keV) are clearly separated with the energy resolutions 63.5% and 19.65% at 1.05 bar. The Np-L_α (13.944 keV) and Np-L_β (17.75 keV) fluorescence from the source are merged, because their energies are close and energy resolution is not good enough to distinguish them.

Spectra presented in figure 5.4 show the performance of the Micromegas structure operated in Xe(98)CF_4(2) mixture at 1 (left) and 3 bar (right) pressures.

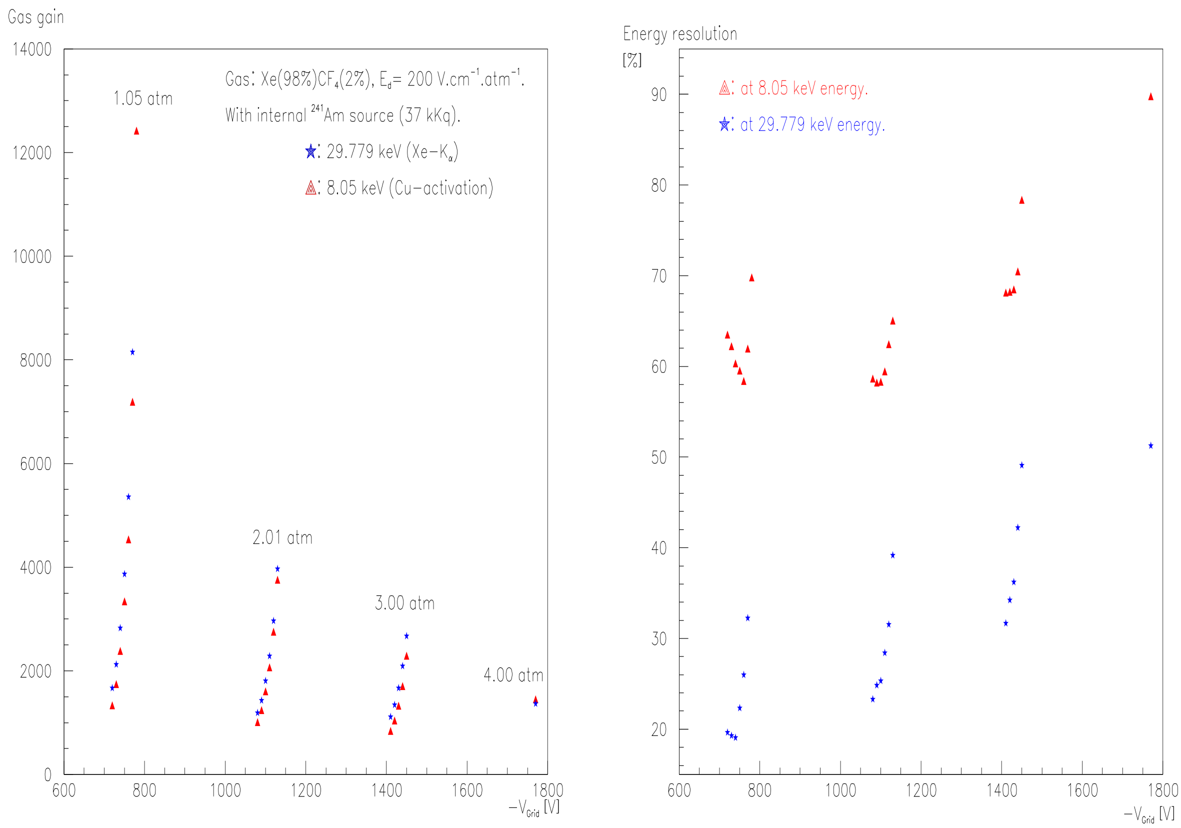

Figure 5.5: Gas gain (left) and energy resolution (right) measurements in Xe(98)CF_4(2) at different pressure with 225 μm gap, using an ^{241}Am source.

The dependence of the gas amplification and the energy resolution of the Micromegas-miniTPC filled with Xe(98)CF_4(2) on the grid voltage at pressures from 1 to 4 bar are shown in Figure 5.5. The limitation of the gas amplification for the upper part is due to the beginning of continuous discharges process.

At 4 bar pressure, we are limited by the cathode voltage and not discharges on the grid.

Gas amplification versus the grid voltage showed the stability of the detector. The exponential form has practically the same parameters for each pressure. The grid voltage increases with the pressure and charge collection is less favored at 4 bar with a moderate energy resolution (about 50% at 30 keV) and a very small working region.

Obviously, measurements are done at the same conditions including the time of purification: 1 day for each pressure, which is not optimized for a dense medium. Circulating longer time at higher pressure and increasing the opening of the grid, can lead to better charge collection with wide working region and make it possible to work at even higher pressure.

5.2.2 Reducing the CF_4 attachment

The excellent imaging capability of MUNU (a TPC filled with pure CF_4 at 3 bar pressure), encouraged us to search for solutions, reducing the electrons loss by the CF_4 attachment.

a. Electrons loss in MUNU experiment: In the reattached study to the MUNU [56] experiment, we estimated the electron loss at different CF_4 gas pressures, under the exact experimental conditions (pressure, temperature, voltages ...).

Simulations with Magboltz and Imonte interfaced to Garfield, showed that the electron loss percentage is proportional to the density of the CF_4 gas. Table 5.1 shows this effect and more details for electrons loss calculations are in reference [61].

Pressure [bar]	e^- loss [%]
1	87
3	95
5	98

Table 5.1: efficiency of MUNU detector at various gas pressure.

The electron loss increases with the gas pressure, which is confirmed by experimental results: the working voltage is higher at higher pressure. At 1 bar of pressure in MUNU experiment, the highest electric field (about 400 kV/cm) around the anode wires, causes a serious electron loss and the charge collection efficiency is about 13%. At 3 bar of CF_4,

only 5% of electrons survive as mentioned in table 5.1. This decrease of the collection efficiency contributes to the widening of the pulse height spectrum for all electrons.
Since the attachment is increased at high electric field, we confirm that the loss of energy resolution is due to a reduction by electron attachment of the avalanche ionization. A comparison between energy resolutions of the MUNU-TPC for 1 and 3 bar was mentioned in reference [38], confirming that the energy resolution at 1 bar is about $1.7-2$ times better than at 3 bar.
Moreover, we established that the energy resolution in CF_4 gas worsens when increasing gas pressure (see section 3.7) and when adding CF_4 to Xe gas (see subsection 5.2.1).
Even under the worst case of the Fano factor F= 1, the energy resolution is worse than expected (formulae 2.2.4). This effect can be explained by the strong contribution of the electron attachment [62].

b. How to overcome the CF_4-attachment problem? In our case, we collect ions: the electron attachment inhibits the ionization process in the avalanche region, so ions production is affected and energy resolution is deteriorated. Therefore, we are thinking to alleviate the CF_4 attachment by adding a quencher and fitting the MWPC with a Micromegas structure.

• **The detection plane structure effect:** The first advantage of the Micromegas micropattern is that all the wires inside a single grid are at the same plane, but it is not the case for the sense-wires and the field-wires in the MWPC detection plane, where they are tensed separately and the two grids are at the same Z-coordinate. This can insure the gain uniformity and the good energy resolution. A comparison between this two detection planes is given in figure 5.6, with the same chamber tested at the same conditions.

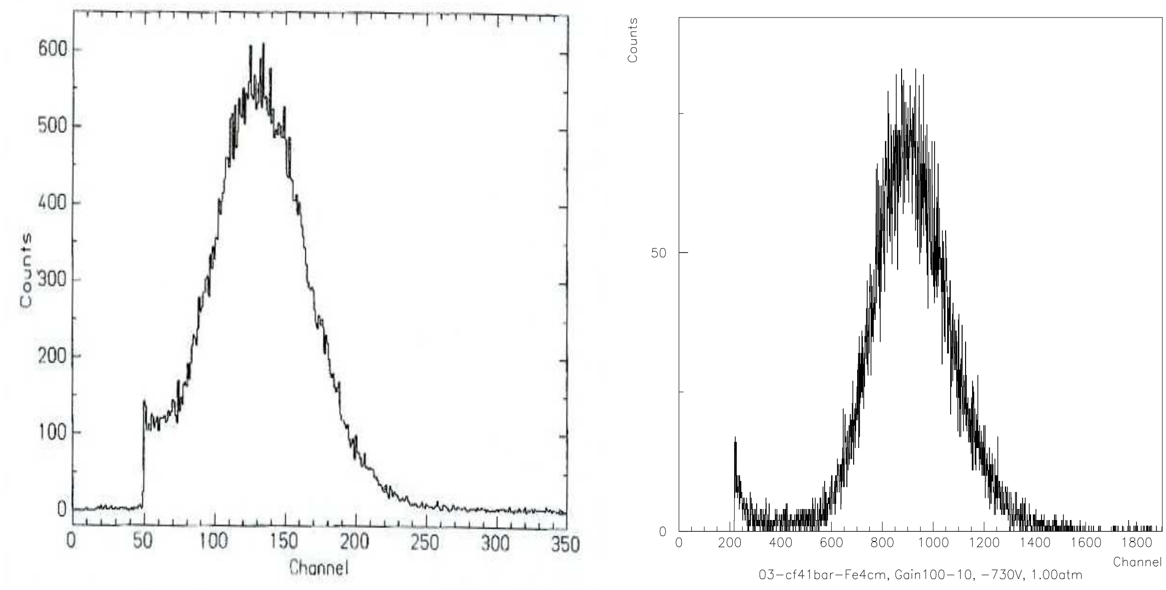

Figure 5.6: ^{55}Fe pulse height spectrum with MWPC wires (left), extracted from reference [41], and with Micromegas detection plane (right) tested in the miniTPC at 1 bar of pressure. Energy resolutions are 50 and 37 %, respectively.

Replacing the MWPC detection plane by the Micromegas one improve the energy resolution by a factor 1.3.

A second advantage is that we have less mass using the compact detection plane than the MWPC (no bulky frame), which leads to low radioactivity and thus, low contribution to the background.

• **The choice of the quencher:** On the other hand, the gas choice is also studied: Xe and Ar gases are candidates to quench CF_4 gas. The first one is simply chosen because of its low operating voltage, and the second one has zero attachment.

The first ionization potential of Xe (12.13 eV), compared with the excitation energy of CF_4 (12.5 eV) molecules, allows the addition of Xe to CF_4, which can quench *lights* caused

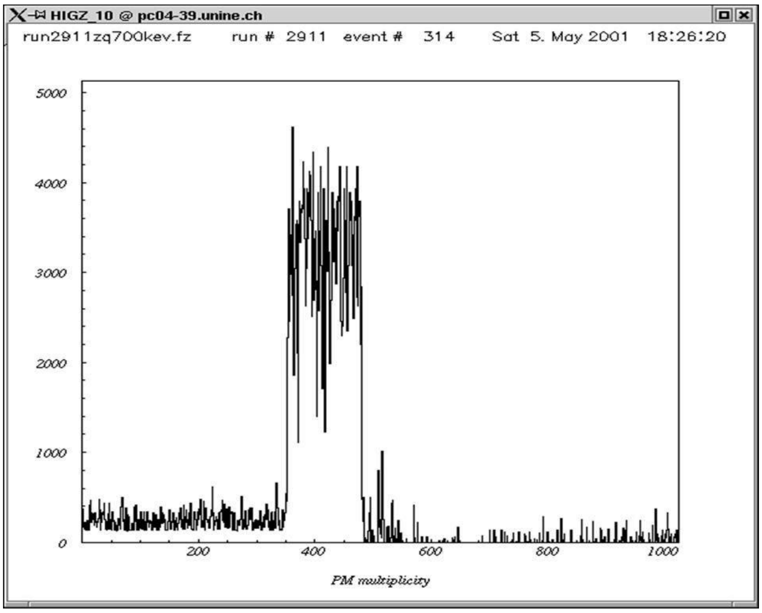

Figure 5.7: Photomultipliers sum from CF_4 light in MUNU experiment.

by $(CF_4^*)^+$ and $(CF_3^*)^+$ fragments [63]. Moreover, lowering operating voltages by Xe addition as showed in figure 5.8, reduces the CF_4 attachment. The high electric field in the amplification region leads to the following decomposition molecules [64]:

$$e^- + \mathrm{CF}_4 \rightarrow (\mathrm{CF}_3^*)^+ + \mathrm{F}^- + e^- \qquad (5.2.3)$$

When stable state is reached, the last dissociated fragment $(CF_3^*)^+$, emits photons in the visible range (λ = 620 nm). Light signals were recorded by the MUNU photomultipliers and an example is shown in figure 5.7.

c. The gas gain of CF_4 gas quenched with Xe or Ar: Measurements are carried out with the same prototype described below with an amplification height 100 μm and using same conditions used for favoring the charge collection in Xe study (pressure, drift field, circulation time ...).

The substantial reduction in the operating voltage when adding noble gases to the CF_4

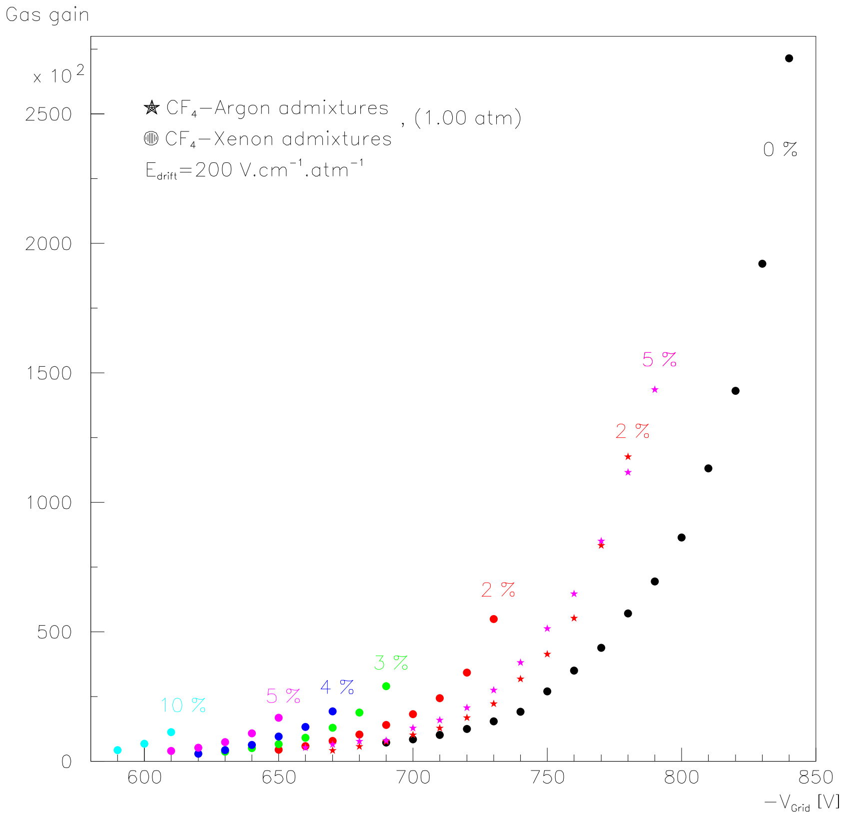

Figure 5.8: Gas gain measurements with CF_4-Xe ($\bullet$) and CF_4-Ar ($\star$) admixtures from pure CF_4 (black) to 10% of Xe and 5% of Ar quenchers at atmospheric pressure.

gas, should strongly reduce CF_4 attachment and improve the energy resolution. This is why we are thinking to use Xe and Ar as quenchers.

The gas gain curves are presented in figure 5.8. In pure CF_4 gas, the working region is about 150 V. Adding noble gas decreases the wide range of the working region but it increases the gas gain at low operating voltages.

The increase of the gas amplification limit in a mixture of CF_4 with Xe could be interpreted as evidence confirming the fact that Xe addition decreases operating voltages essentially and therefore attachment. For example, we can obtain the same gain (6×10^4) with the

CF_4(98)Xe(2) than with the pure CF_4 at lower operating voltage (50 V of difference), which can help to prevent cathode high voltages with long drift volumes.
Moreover, this addition decreases the probability of photoeffect on the grid wall, caused by ultraviolet photons from CF_4 fragments.
In our opinion, the presence of Xe atoms can prevent the formation of those fragments, especially dissociative processes, because the operating voltage is lower than before.
A small addition of Xe reduces the working voltage and increases the gas amplification. At the same grid voltage, we obtain a gas gain 10 times greater with CF_4(98)Xe(2) than with pure CF_4. This can be explained by the decrease of the number of electrons lost in the avalanche ionization region.
CF_4 with Xe addition at pressures ranging from 0.8 atm up to 14.8 atm, used in the Multi Cell Proportional Chamber "MCPC" (see appendix B) to search for WIMP's [65] and gas gains even in pure CF_4 or in quenched one with Xe did not exceed 10^3. Recently, a Triple-GEM TPC prototype [66] was operated in CF_4 gas and the maximum achieved gain is 10^4. An energy resolution of about 30% at 5.9 keV was obtained, which is somewhat better than our resolution at the same gain (see figure 5.9). Note that in our case, field shaping rings are 2 cm spaced compared with 3 mm in the case of the cited reference, which insures best uniform electric field in the last prototype and less electrons-ions fluctuations when drifting to electrodes. In addition, the drift electric field is also higher than used in our case, which drifts faster electrons to the detection plane. Here results obtained in section 3.6, are confirmed.

d. The energy resolution in CF_4 gas quenched with Xe or Ar As presented in figure 5.9, the energy resolution is not improved when adding Xe or Ar quenchers. It is a consequence of the increase of diffusions and the lowering of the drift velocity in these admixtures. But the lowering of the operating voltages and the higher gains obtained prove the good collection efficiency as confirmed by the obtained higher gains.

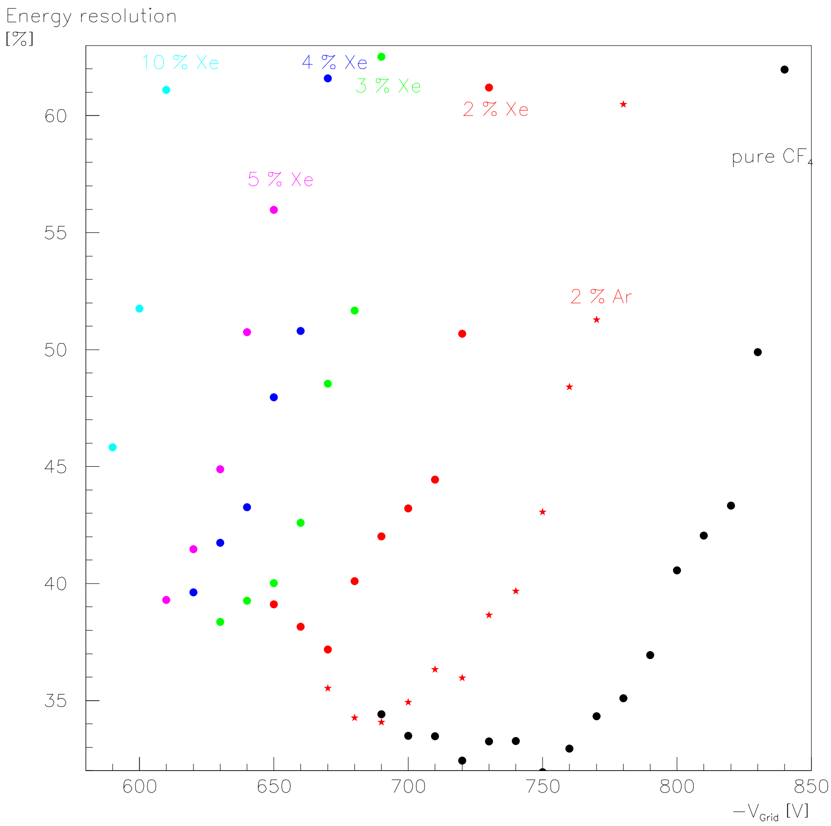

Figure 5.9: The energy resolution at 6 keV, measured in CF_4-Xe (•) and CF_4-Ar (⋆) admixtures from pure CF_4 (black) to 10% of Xe and 2% of Ar quenchers at atmospheric pressure.

We can also take into account the gas purity inside the amplification zone. The least humidity is responsible for the field perturbation and discharges. In our measurements, we purify 1 day for all gas admixtures, knowing that Xe needs more purification time than CF_4.

The energy resolution is also affected by the deformation of the equidistance between the grid and the anode. Even with its simple design, it is difficult to get a perfect parallel gap. The grid is not perfectly flat and the gap is not homogeneous everywhere and the non uniformity of the field near the grid affects seriously the energy resolution. But, this is not an argument for energy resolution poorness, because we used the same detection plane for all our tests.

Light information

The tracking can be further improved using photon energy information [21]. This has been made possible by using Micromegas micropattern with Xe-CF_4 at high pressure. The MSGCs operated with the Xe-CH_4 gas at high pressures was used [67] to study this effect. We can have good tracking with Xe-CF_4 gas, thanks to the abundance of the UV light emitted by Xe and CF_4 dissociated fragments scintillations. The detector can measure both the ionization electrons and the scintillation light to improve the energy resolution. We can use the scintillation properties of Xe and CF_4 in UV and visible range of light, to have good track and clear image. We suggest that further investigations in this direction are likely going to improve the energy resolution.

In addition, it is necessary to measure the primary scintillations they produce, to fix the time at which the charges begin to drift. This is why CF_4 scintillation will help us to achieve this aim. More investigations on the detector development to study primary scintillation are required.

Gotthard-TPC results

Chapter 6

New results from the Gotthard-TPC: low background achieved with a large Micromegas detection plane

Abstract

The search for extremely rare events with low energy threshold requires low background environments, cosmic ray shielding, detectors with large masses, and new techniques to reach high sensitivities.

Before going to a mass of several tons, we need an intermediate scale prototype to test the technology and to design the final detector. Thanks to an existing TPC detector in the Gotthard tunnel under the Swiss-Alps, where we can test the properties of such a detector. In the R&D for the EXO project: new techniques, based on a Micromegas micropattern, are developed to search for rare events, especially for neutrinoless double beta decay in ^{136}Xe isotope.

Results with a large Micromegas detection plane, with good energy resolution in CF_4 and P10 gas mixtures, will be presented. Detector components are measured in a low background Ge detector, in order to bring up relevant background sources in rare event detection experiments.

This chapter contains measurements needed for the construction of a large TPC for double

beta decay, dark matter and solar neutrinos detection.

6.1 Introduction

Higher detector sensitivities are obtained either by increasing *the count rate* or decreasing *the background rate* or combining both. The first one depends on detector mass and an efficient readout plane. The second one depends on the laboratory location and the choice of materials. Our efforts and activities are consecrated to both.

The most important factor, to take into account, is the background of the detector itself, due to radioactive contaminations of materials. It is essential to check the radiopurity of components before using them in low background experiments.

6.2 The Gotthard-TPC detector

The Gotthard TPC was installed in 1989 in a deep underground laboratory under 1460 m of rock[1], to protect the detector against the intense flux of parasitic events. This rock covering reduce the muon flux by a factor 10^6 compared with its intensity at the earth surface, as shown in reference [13].

The Gothard-TPC detector was filled at 5 bar of pressure with Xe gas enriched to 62.5% of ^{136}Xe, to search for rare neutrinoless double beta decay in this isotope (see section 1.2), and around 5% of methane as a quencher.

The main chamber (see figure 6.1) is itself the inner shield, with a 5 cm thick OFHC[2] copper vessel, with 57.4 cm inner diameter and 69.7 cm inner height. 65 field shaping rings spaced with 1 cm distance, are placed inside to insure the electric field homogeneity. The outer shield is about 20 cm of low radioactive lead[3].

[1] About 3700 m water equivalent.

[2] Oxygen-Free High Conductivity.

[3] Older than 200 years (Swedish mine).

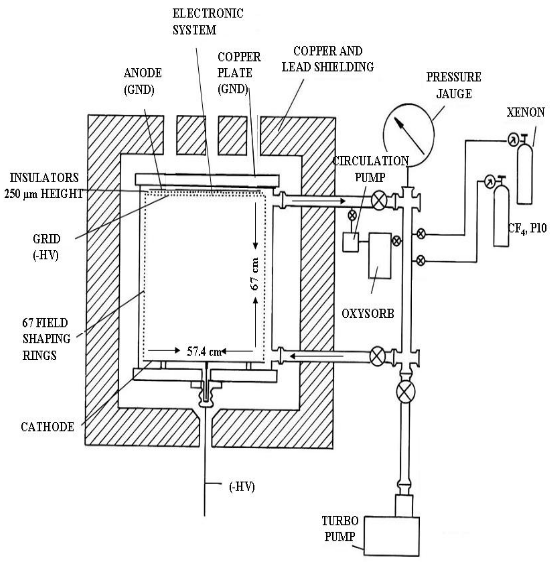

Figure 6.1: A schematic description (left) and a photograph showing the Gotthard TPC (right). The purification system is located in the left of the photographic view.

The body of the TPC is separated from the ground with 6 spacers[4], to insure a low level microphonic noise, considered as a source of background. More details on design and detector construction can be found in reference [68].

A full description of the TPC and the acquisition system are presented in reference [69], as well as experimental details and results from a first data taking period of 6830 h.

The background was estimated to about 0.01 counts/(keV·kg·years) at the "0ν" energy range. This is a good argument for us to cling to this valuable fact, which compensated the poorness of the energy resolution comparatively to Germanium detectors.

A skirt of 0.5 cm thick of boron carbide (B_4C), covering the lead shield, was added in 1994. This shielding contains ^{10}B, which is not radiative and particles emitted by the capture reaction ^{10}B(n,α)^{7}Li have high energy loss and large cross section (σ = 3840 barns) for thermal neutron capture [70].

[4] Kevlar strings are usually used to hung on "up moving" detectors.

Neutron capture efficiency has been measured, after the boron carbide installation, by using a Cf neutron source and a difference of 40% for β-like events in the interval from 1 to 3 MeV has been observed [71].
Some experimental results, from a second data taking period of 12843 h, are published in reference [13], after the B_4C addition and crimping wires to the frames with copper needles instead of solders. After this, the rate in the "$0\nu\beta\beta$" energy region was 2 times better than in the first data. Results are also cited in [72].
The TPC detector proved its tracking capability and particle identification, although, the energy resolution at the Q-value (2481 keV) was about 6.6%.
The experiment was stopped in 2000 and until now, the detector is used for R&D of the EXO near future experiment.

6.3 Radioactivity and background sources

Counts from cosmic rays, shielding material or intrinsic contamination of the detector itself, can cover the signal counts of interest. The behavior of some fake electrons can be similar to the real electrons coming from Xe decay. Therefore, the detector medium has to be as radiopure as possible, in order to avoid fake reactions or to keep them as low as possible. Further, an extremely low background in the TPC is needed to increase detector sensitivity to the "$0\nu\beta\beta$" channel resulting from Xe decay. Obviously, we should find background sources, which can affect the sensitivity in the "0ν" channel.

6.3.1 External background

The chamber is sufficiently shielded against photons coming from the ^{238}U, ^{232}Th decay series and ^{40}K decay. In addition, the whole shield of (B_4C-lead-copper) is able to stop about 10^3 of neutrons [71].

Gamma rays: The lead shielding is thick enough (about 20 cm) to reduce the external gamma flux due to the rock radioactivity and resulting from all existing material in the lab. The radioactivity of lead was measured and it confirmed its high radiopurity. It emits around 10^{-9} [Bq/g] of (^{232}Th and ^{238}U) and 10^{-8} [Bq/g] of ^{40}K, as it is shown in table 6.1. In addition, the copper is able to stop low energy emissions due to the lead itself and a big part of the rest of the external flux.
The only problem arises from the ^{210}Pb isotope with 22 years of half life. The 5 cm thick copper shielding is able to stop a greater part of gammas coming from ^{210}Pb descendants. But, this radioactive isotope can be contained in solders or coming from radon decays.

Muons and neutrons: Only muons remain worrisome particles in our case. Even with an extreme attenuation factor of about 10^6, thanks to the rock covering, muon interactions can take place in the neighboring rock and in the detector shielding (lead and copper).
When arriving at the external lead shield, negative muons are attenuated after a mean free path, depending on their energies, and produce neutrons via[5]:

$$\mu + \mathrm{Pb} \quad \longrightarrow \quad (\mathrm{Pb})^* + n \sim [MeV]$$

When returning to its stable state, the lead isotope can produce gamma rays, which can be attenuated by the copper shield.
The rest of muons can reach the copper shielding and interact with it, producing neutrons or fake electrons, so two reactions can occur:

$$\mu + \mathrm{Cu} \longrightarrow (\mathrm{Cu})^* + n \sim [MeV]$$

$$\mu + \mathrm{Cu} \longrightarrow e + \mathrm{Cu}$$

The excited copper regains its stable state by gamma ray emission, that can also contribute to the background, especially when the interaction occurs in the inner surface of the copper

[5] This interaction can also occur in the Cu shield and the gas medium.

face to the active volume.

Neutrons can also be produced by spontaneous fission or by spallation when high energy protons reach the laboratory.

If they have sufficient energy, muons can penetrate the outer and inner shielding and cross the detector medium producing fake electrons via:

$$\mu + \mathrm{Xe} \quad \longrightarrow \quad (\mathrm{Xe})^{*} + n \sim [MeV]$$

Moreover, sufficiently energetic neutrons, even if they scatter elastically from the whole shielding in the detector or if they are produced by muon interactions, can be captured by gas atoms, forming high energy β emitter ^{137}Xe, which decays via ^{136}Xe(n,γ)^{137}Xe neutron capture reactions.

Radon contamination: Radon is an intermediate member of all two decay series (^{238}U and ^{232}Th). This radioactive gas, can escape from the solid matrix either by recoil on ejection of the α particle or by diffusion from the earth's surface into the atmosphere. The radon rate depends on the rock composition (pegmatite or granite).

For example, Fréjus rock, measured at our Ge detector, emits about 10^{-1} [Bq/g] from ^{40}K and around 10^{-2} [Bq/g] from ^{232}Th and ^{238}U series (see table 6.1). These values explain the increase of radon rate near the NEMO-3 experiment [73]. The Gotthard rock was also measured and it emits about 1.42 [Bq/g] from ^{40}K and around 10^{-2} [Bq/g] from ^{232}Th and ^{238}U series.

The radon rate depends also on the humidity [74]. To keep the humidity low, the laboratory is located in the security tunnel with a continuous flush-air. In addition, a deshumidificator was put near the Gotthard-TPC to regulate the humidity to an acceptable level.

In spite of muon and neutron troubles, the external background is not the major problem in a deeper underground laboratory like the Gotthard-TPC. In addition the good lead-copper-B_4C wall-shielding insure a good protection against external noise, which can contribute to the background increase. This is why, our efforts are consecrated to the study of the intrinsic background of the detector itself.

6.3.2 Internal background

Shorter-lived radioisotopes produced by detector components, are the basic participants in the increase of the background rate. Thus, the materials need to be radiopure to keep count rates below the real signal.
For this reason, we tried to understand sources of background and to identify radioimpurities from each detector component through gamma spectrometry, hoping to keep the intrinsic background of the detector low, and to increase the chance to observe the "$0\nu\beta\beta$" decay.

Sample measurements: Some detector components are measured in the "La vue des Alpes" Ge detector. Radioactivity, mechanical properties and of course the cost are taken into account.
Location and full description of the Ge detector are explained in details in reference [75].
The sensitivity of the detector is below 10^{-10} [g/g] for ^{232}Th or ^{238}U, 10^{-6} [g/g] for ^{40}K and 10^{-21} [g/g] for ^{60}Co, details are in reference [76].
The advantage of this measurement technique is that the radioactivity is deduced indirectly, without any damage of the component.
The sample chamber is flashed with nitrogen recirculation and the spectrum is recorded during one week without opening.
We do not consider the first day of acquisition to avoid radon contaminations. This is necessary to help moving the radon with a half life 3.825 days.

Materials		Activities [Bq/g]					
		^{238}U series	^{232}Th series	^{40}K	^{137}Cs	^{60}Co	Remarks
Lead(Gotthard)		<10.3E-09	<1.12E-09	7.03E-08	3.14E-08		Good
Copper (rings + cath + tpc)		1.25E-05	3.27E-06	3.46E-05	5.44E-05		Good
Rock (Frejus) **Rock(Gotthard)**		1.61E-02 2.29E-02	1.13E-02 3.61E-02	1.99E-01 1.42	2.22E-04		The radon rate is high
Resistors [10MΩ] ceramic	with markers (colors)	<1.82E-03	1.14E-03	<9.90E-03			**High radioactivity** (Quartz Resistors are needed)
Glue	Araldite 2011	< 3.5E-05	< 3.E-06	< 8.4E-05	< 3.0E-06		Ref : J.Busto et al NIM A 492 (2002) 35-42
Insulators	Delrin	3.05E-06	5.18E-06	6.78E-05	<6.96E-05		Comparable but delrin is cheaper and easy to manufacture
	Teflon	<3.64E-06	<2.76E-06	<2.45E-05	<2.37E-06		
Grid	Bopp (s-s-v)	<7.77E-04	<4.80E-05			<3.47E-05	**Good**
	Gantois (s-s-v)	<9.05E-04	<2.05E-04				Slightly expensive than Bopp
	Euromip grid (etched)	<2.52E-04	<2.97E-04	<6.45E-03			
Detection plane	Printed circuit (resin-epoxy)	6.05E-02	2.31E-02	1.22E-01	1.30E-03		**High radioactivity**
	Full detection Plane (anode+grid)	1.40E-02	2.22E-02	1.47E-02	5.98E-04		This radioactivity is due to the printed circuit
	Kevlar	<7.54E-06	<6.14E-08	5.56E-04	8.28E-04		**expensive**

Table 6.1: Radiopurity levels of different elements measured with the Ge detector installed in the "la Vue des Aples" laboratory.

The table 6.1 recapitulates the most disturbing background sources for the Gotthard detector components.

The inner components, especially resistors, solders and the detection plane based on the printed circuit material (or resin-epoxy), have higher specific activities. The presence of the ^{137}Cs radioisotope is due to nuclear weapons testing and the Chernobyl accident.

a. Radioactive components:

The detection plane: Resin-epoxy is considered as radioactively dirty compared to Kevlar-epoxy. One can see in figure 6.2 the big difference between the activity of these two components. The printed circuit activities are about 10^4 larger than the Kevlar one.

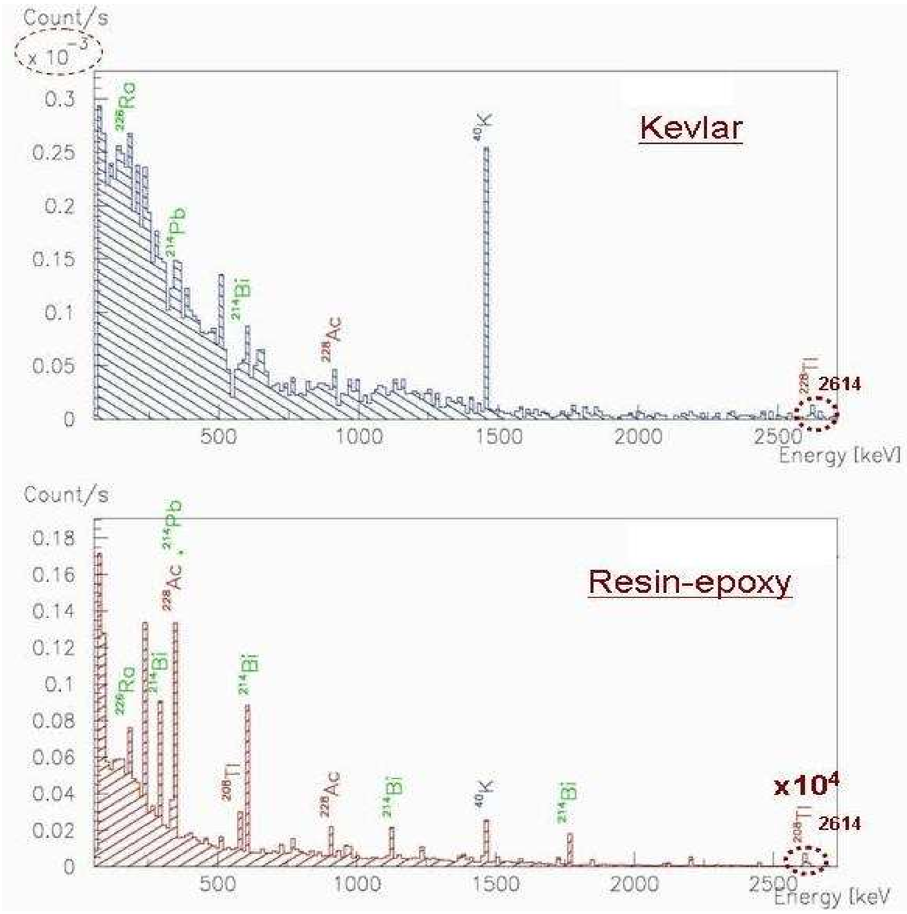

Figure 6.2: Comparison between the activity of the Kevlar-epoxy (top) and the resin-epoxy (bottom) insulators, measured at la Vue des Aples Ge detector.

The 2614 keV γ-line from ^{208}Tl (Th chain descendant) existing in the printed circuit, even if it has low counting rate (0.01 count/s), can be a worrisome source of background in the region of interest for the "$0\nu\beta\beta$" decay in Xe.

Knowing that plastic materials consist mainly of C, H and O, we have two additional sources of background[6]: ^{3}H and ^{14}C. These components contribute to the background at lower energies (some keV), which is the range of interest in the case of dark matter and

[6] ($^{14}C \rightarrow {}^{14}N + e^- + \overline{\nu}_e$)

low energetic solar neutrinos search.

Contaminations can also originate from chemical treatments, during material manufacturing, which is the case for the etched grids. The nickel grid is etched chemically, therefore it has an activity higher than the mechanical grid (see table 6.1).

Solder: In solder, ^{210}Pb can be introduced with tin [77]. Moreover, the background was improved by about a factor five in the Gotthard-TPC [13], by crimping the wires instead of using solder. Therefore, we should avoid solder and replace it with another candidate.

Resistors: Resistors are radioactively bad. In most resistors, the activity came from the ceramic material [78]. So, we need other resistors, quartz for example. Color-lines engraved on the resistors can also be a source of background. Scratching out color can reduce this radioactivity.

b. Radiopure components: All field shaping rings, cathode plane, the TPC itself, are constructed with the same copper. Radioactivity measurements showed the property of all these components as confirmed in table 6.1.

Moreover, the contamination level of the lowest background (delrin & copper) is, after all in the range of a few μBq/g for ^{40}K, ^{238}U and ^{232}Th.

6.4 Energy calibration of the Gotthard-TPC

Two external gamma ray-sources (^{241}Am and ^{137}Ba) are used to calibrate the Gotthard-TPC. They are placed outside, in a conic window (see the right side of the photograph presented in figure 6.1). This position is perpendicular to the drift direction, serving to irradiate the detector and initiate the ionization process.

An additional ^{241}Am source was put inside, face to the cathode.

The external sources, with equal activities (370 kBq), was chosen with an activity ten times higher than the internal one (37 kBq), in hope for initiating the ionization process from the outside of the chamber via the conic window.

The ^{241}Am source has a single γ-line at 59.5 keV and the ^{133}Ba source emits several γ-lines between 81 and 383 keV.

When collecting the charge on the grid, which is proportional to the energy deposited by the interaction, we measure the energy distribution of electrons coming from gamma rays by photoelectric effect or Compton scattering interactions.

Two sizes of Micromegas detection plane were tested, 9 and 50 cm of diameters in different gas mixtures.

6.4.1 An active area of 9 cm of diameter

In a first step, a 9 cm full active area Micromegas detection plane was used. This micropattern, replaced the MWPC's readout plane used before for the Gotthard experiment: it represents only 15% of the full active area. The detector efficiency is inevitably less than with a big detection plane. But, background problems can nevertheless be tackled.

These tests were done before going to a big Micromegas, which is more difficult to built and delicate to handle.

We chose 200 V.cm^{-1}.bar^{-1} as a drift electric field and a 250 μm as a Micromegas gap height for all our tests, according to tests done in sections 3.6 and 3.8 respectively.

Results given in the section 3.8 proved the good charge collection at higher pressures when increasing the height of the gap (225 μm)[7].

With the small area, however containment of events is poor and it is harden to see an external source put in the conic window of the chamber. Therefore, several tests were done with the internal ^{241}Am source with a 37 kBq of activity face to the cathode.

The chamber was filled with 1.02 bar of CF_4 gas as a fast gas.

[7] The variation on height (225 and 250 μm) is due to CERN manufacturing.

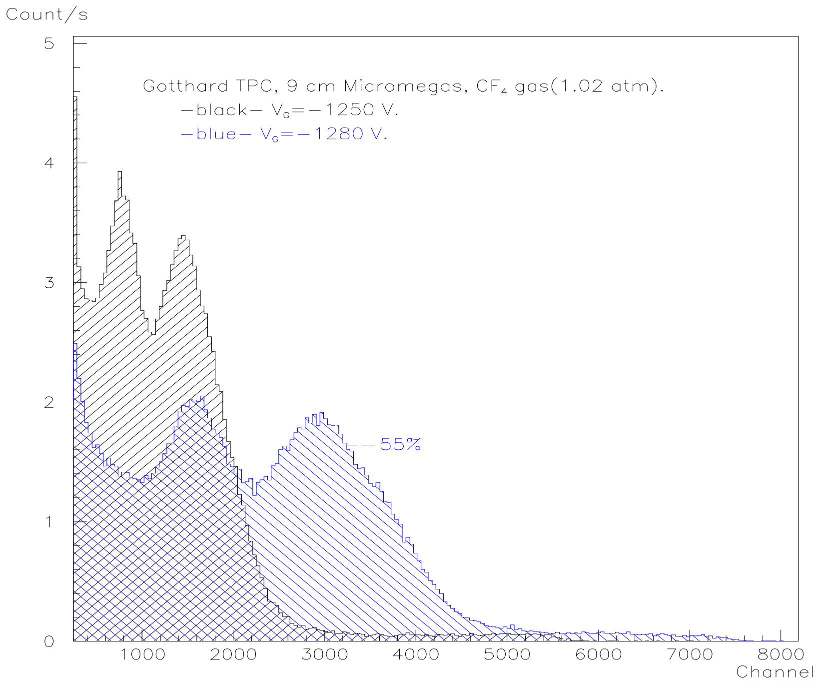

Figure 6.3: Voltage effect on the displacement of copper activation and Neptunium transitions, using 9 cm detection plane at 1.02 bar of CF_4.

Copper activation (Cu-K_α(8.05 keV)) (first peak) and Neptunium transitions (Np-L_α(14 keV) and Np-L_β(17 keV)) (merged in the second peak) are observed as shown in figure 6.3. An energy resolution of about 78.5% is achieved at Cu-Kα energy, with a grid voltage $V_g = -1280$ V.

Our tests showed that working at higher pressure in CF_4 gas with Micromegas detection plane is made impossible by the attachment, so it is useless to go up to higher pressures. Results presented in reference [42] and also in the section 3.7 confirmed our explanation.

6.4.2 An active area of 50 cm of diameter

Results presented above, are encouraging to elaborate a large scale Micromegas detection plane with 50 cm of diameter. The largest operating Micromegas until now is mounted in the COMPASS [79] experiment (40×40 cm^2).

a. Energy calibration in CF_4 gas

The effect of an external source: We are using the same gas (CF_4) and gap (250 μm) at atmospheric pressure and keeping the internal ^{241}Am source plated on the copper cathode.

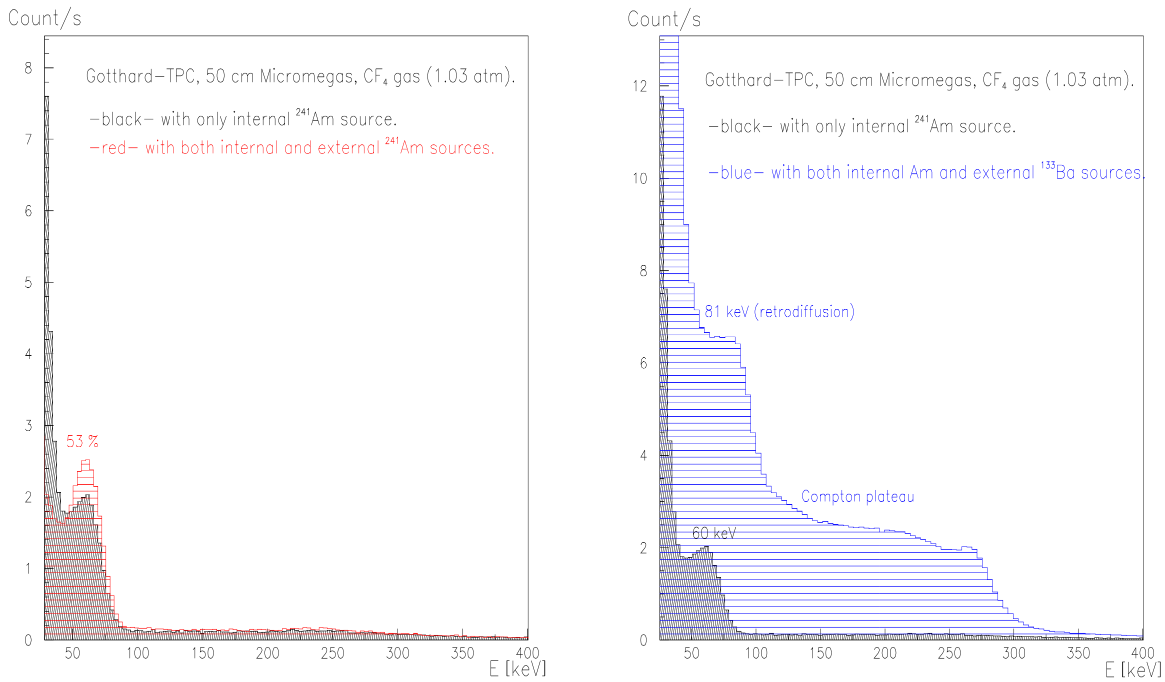

Figure 6.4: The effect of external ^{241}Am (left and red) and ^{133}Ba (right and blue) sources, added to the internal one (black), with 50 cm of Micromegas diameter at 1 bar of CF_4.

The cathode is set at -13.8 kV and the uniformity of the drift field is achieved by 1 cm spaced field shaping rings. Simulations presented in section 4.1 proved the homogeneity of the electric field inside the chamber.

Spectra presented in figure 6.4, respectively for external ^{241}Am and ^{133}Ba sources added to the internal ^{241}Am one, showed the good efficiency of the large Micromegas detection plane (50 cm of diameter). The energy resolution at 59.5 keV is about 53% at 1 bar of CF_4.

In addition, the Compton structure of the Ba source is seen in the right plot of the figure 6.4, with the 81 keV retrodiffusion gamma-line peak. The black spectrum in both plots (left and right) represented the response of the detector with only the internal ^{241}Am source. Better containment with the larger Micromegas is thus obvious.

The background in CF_4 at 1 bar pressure: Once, we established that we can see the source from the conic window of the chamber and we can distinguish between each source, we decided to eliminate the internal ^{241}Am source put on the cathode and started acquiring a background spectrum.

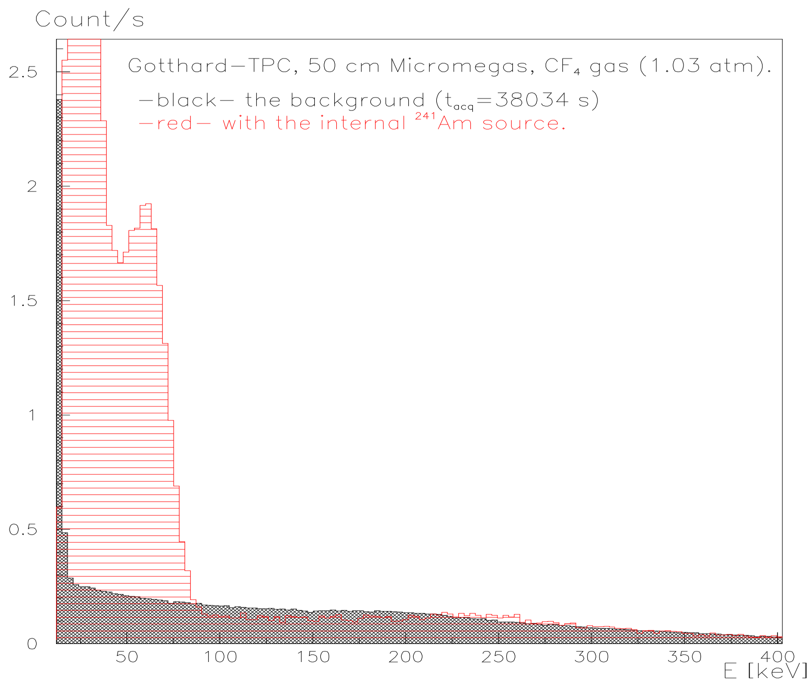

Figure 6.5: The background spectrum (black) superposed with an energy spectrum of an internal ^{241}Am source (red), in the Gotthard-TPC filled with CF_4 at 1.03 bar.

When comparing the internal ^{241}Am source spectrum with the background one, the high count rate caused by the source is clearly observed at lower energies as seen in figure 6.5. This is due to Neptunium transitions and to the activity of the support of the source. At higher energies, the count rate, even with or without a source, is remarkably low and still the same. The count rate at the maximum of the ^{241}Am source emission (about 1.9 count/s at 60 keV) is around ten times bigger than the background rate at the same energy (about 0.2 count/s).

When coming back to sample measurements (paragraph 6.3.2), we remarked that components emit almost nothing in the energy range of interest, even for the components considered as highly radioactive. In the case of the printed circuit (see figure 6.2), it emits nothing in the energy range $2460 < E$ [keV] < 2600. The background will be lower with a radiopure Kevlar-epoxy detection plane.

All spectra taken with the Gotthard-TPC have the same amplifier gain setting.

b. Energy calibration in P10 gas at 1 bar pressure

Test with a cheaper noble gas is essential before going to the expensive Xe(98)CF_4(2) gas mixture. For this reason, we are testing the Micromegas micropattern as a detection plane in the Gotthard-TPC with the P10 gas, in which purification is easy, just circulating via the oxysorb filter, and it works without a cold trap. A cold trap is necessary for Xe gas to trap humidity and Freon.

External source effect: Before going to higher gas densities, we start operating the detector and collecting charge at atmospheric pressure.

P10 gas has a low operating voltage like all noble gases, which is an advantage to avoid high electric fields and sparks.

Both 59.5 keV gamma emission of the ^{241}Am source and 81 keV resulting from the Compton scattering of the ^{133}Ba source are observed. An energy resolution of about 43.5% at 59.5

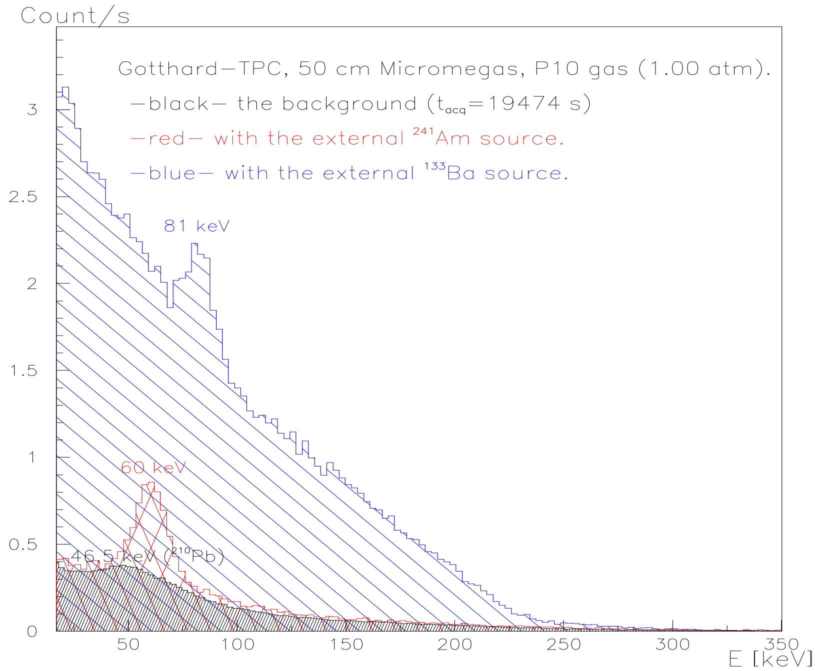

Figure 6.6: Pulse height spectra in the grid for ^{133}Ba (blue), ^{241}Am (red) sources and the background (black) registered in the Gotthard-TPC filled with P10 gas at atmospheric pressure.

keV is achieved as shown in figure 6.6. Notice that we purified the gas medium during one day only. The energy resolution at the same energy was worse in CF_4 gas because of the increased loss of electrons by this gas.

Voltage effect: When varying the grid voltage, the spectra are shifted forwards higher channels keeping the same integral as it is shown in figure 6.7.

Usually, we test the effect of the grid voltage on the peak displacement to be sure that we have is a physical signal and not an electronic oscillation.

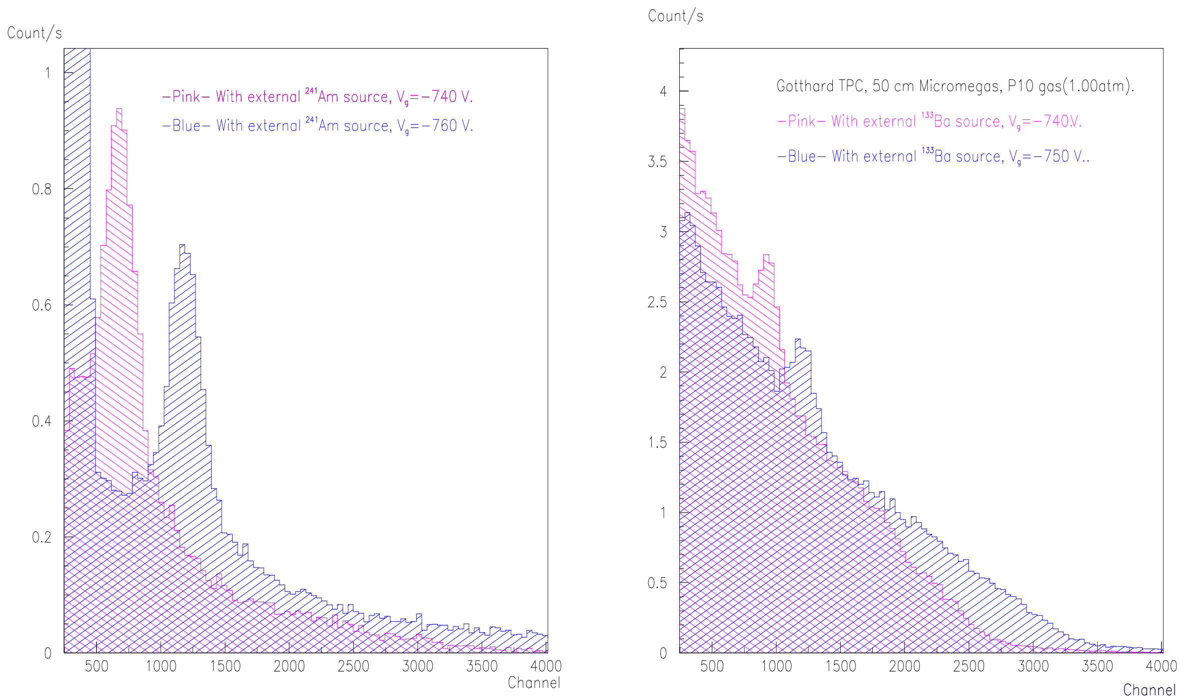

Figure 6.7: The voltage effect on the displacement of the ^{241}Am (left) and the ^{133}Ba (right) spectra.

The background in P10 at 1 **bar:** When seeing the background spectrum (the black plot) in figure 6.6, a remarkable fact is that the background has no an exponential decay shape. Calculation of the corresponding energy of the peak existing in the background spectrum gives around 46 keV of energy. This peak is probably due to the ^{210}Pb, the longer-living progeny, which can be produced by solders existing in the TPC-cover[8].

The count rate of 46 keV gamma is around 0.37 cnt/s at 1 bar of P10, compared with 60 keV source emission, we have around 0.85 cnt/s. It is not negligible but it is far from the region of interest in the case of double beta decay search. We can reduce it by keeping low or avoid components containing the ^{210}Pb isotope, by changing for example the cover of

[8]The endings of the old readout plane of the Gotthard experiment.

the TPC.

Coming back to the 1 bar-CF_4-background (figure 6.5), we conclude that we have the same shape, but the bad energy resolution in CF_4 gas hide away this peak.

c. Tests with P10 gas at 3 bar

The aim of all tests done before is testing the performance of a large Micromegas detection plane and operating it at higher pressures (up to 3 bar). Consequently, we encounter more problems such as, gas purification.

The necessity of long time gas purification: The effect of the circulation time on the appearance of the spectrum and on the energy resolution is important.

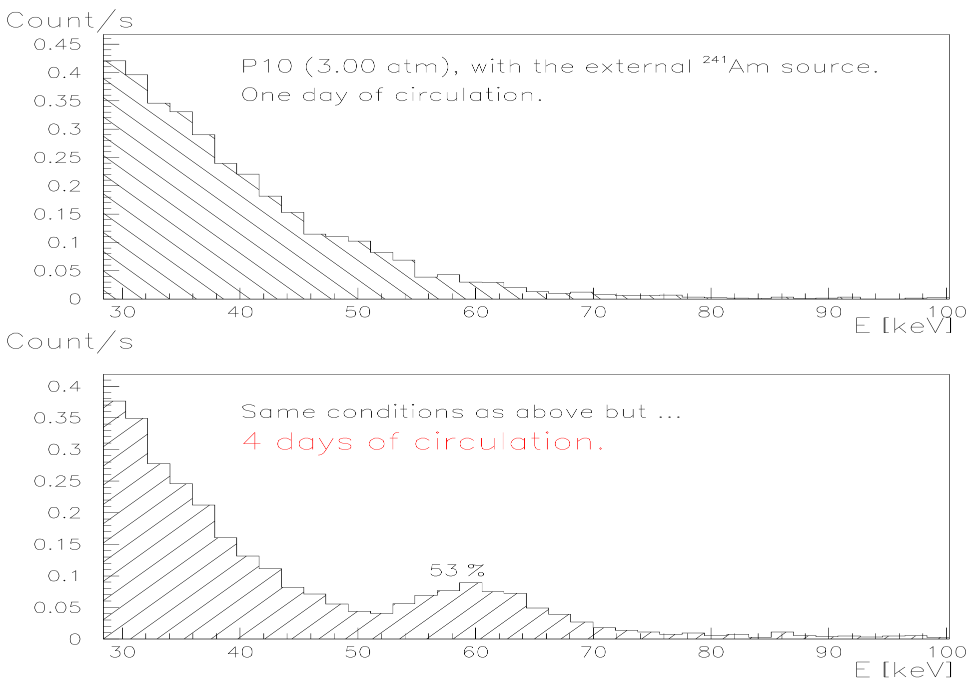

Figure 6.8: The pulse height spectrum in the grid for 60 keV X-rays, measured in P10 gas at 3.00 bar pressure, registered after 1 day (top) and 4 days (bottom) of circulation.

After 1 day, the 59.5 keV peak is indistinguishable from the background signal, but after 4 days, we can distinguish the ^{241}Am spectrum of the external source with an energy resolution of about 53% at this energy.
A comparison given in figure 6.8, showed the effect of circulating a long time, especially in a dense medium. It was not the case for 1 bar pressure of P10 gas, when we start collecting charge after just one day of circulation via the "oxysorb" filter. In the case of Xe gas, we need an additional cold trap in the purification system and of course a long time of circulation.
The resolution range of the ^{55}Fe energy at 3.00 bar of P10 gas tested in the miniTPC, was 29% < R_{6keV} < 33% in the interval of the grid working region.
The gas gain was about $10^3 < G_{P10} < 10^4$. At the same pressure and gas, the ^{241}Am energy resolution is about 53% after 4 days of purification in the Gotthard-TPC. Here, the large volume is the first responsible for energy degradation compared with the results presented in the section 3.8, when operating in the miniTPC prototype.

The background at 3 **bar:** The higher count rate at low energies (below the source response) is probably due to ^{210}Pb or to beta-active contamination near the detection plane.
A comparison between the background at 1 bar and 3 bar is given in figure 6.9. The peak 46 keV at 3 bar is hardly distinguished from the background spectrum. This can be explained by the deterioration of the energy resolution at 3 bar.
The purity specification for U and Th and for their progenies inside the TPC has a very low contribution to the "$0\nu\beta\beta$" production rate as it is shown in the table 6.1 and confirmed with the background at 1 and 3 bar in P10 gas.

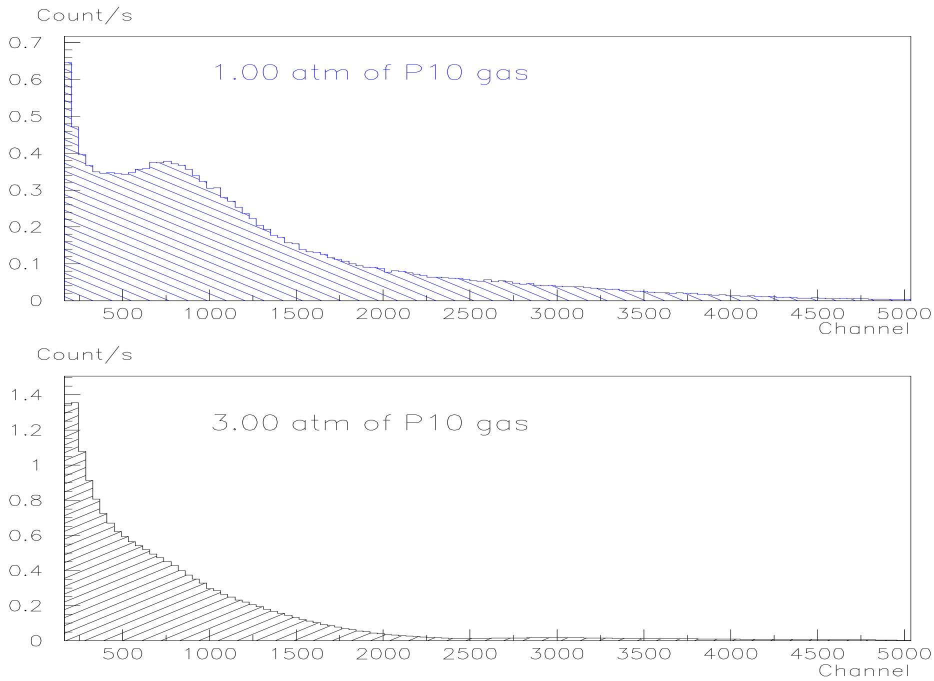

Figure 6.9: The behavior of the background registered in the Gotthard-TPC filled with P10 gas at 1.03 bar (top) and 3.00 bar (bottom) of pressure.

6.4.3 Energy calibration in Xe(98)CF_4(2) gas mixture

Our goal is to test the charge collection efficiency of the large Micromegas (50 cm of diameter) in a *large drift volume*, with the gas mixture chosen for neutrinoless double beta decay search Xe(98)CF_4(2).

Before going several hundreds of kilometers to the Gotthard tunnel, preliminary tests were done with the miniTPC (described in 3.1) at the Neuchâtel laboratory, in order to fix operating voltages and the limit of working pressure. Details are in paragraph 5.2.1.

In the near future, we will operate the large Micromegas-TPC with Xe(98)CF_4(2) at the highest achieved pressure.

Conclusions

Our detector is optimized for the measurement of the energy of double beta decay in ^{136}Xe. Undoubtedly, a precious detector-characteristics is essential for the observation of this rare and weak interaction: the energy resolution, which must be sufficient to distinguish the small "$0\nu\beta\beta$" peak from the continuous "$2\nu\beta\beta$" spectrum.

Good resolution is linked to high statistics, also relevant for low threshold energy, which allows to measure the small signal generated by other rare events (dark matter recoils, solar neutrino events) and increases the collection efficiency.

Consequently, tests have been performed with Xe as a double beta decay candidate, with CF_4 as an additive, in order to use also its good transport properties. Different proportions, going from a tiny mixed Xe to a pure CF_4 gas, have been studied. Comparisons with other quenchers like iso-C_4H_{10} and methane are also established showing the suitability of the CF_4 as the best additive for xenon. The drift velocity becomes higher, diffusions are reduced and gas gain is higher with only 2% of CF_4.

We showed the performance of the Micromegas-TPC with high gains and good energy resolutions for different gas mixtures. In addition, we proved that the increase of the gap height permits a good charge collection at higher pressure (4 bar). We obtained higher gains and wide working regions with higher gap heights than with smaller ones. We compared 75 and 225 μm gap heights and we achieved easily 10^4 with the last one at 3 bar of pressure in Ar(90)CH_4(10) gas, compared to 10^3 with the first one. While, when increasing the gas density to 4 bar pressure, the smaller height (75 μm) can not be operated and discharges occur rapidly. But, with 225 μm gap height, we can reach an amplification factor of about 10^4 with good energy resolution (about 30% at 6 keV) in the same gas.

Based on these results, a 250 μm gap height was chosen for a large detection plane (50 cm) installed in the Gotthard-TPC. Good results are obtained from the fastest gas (CF_4) to the noble and cheaper one (P10). Regarding these results, we are confident to operate the same detector with the Xe(98)CF_4(2) gas mixture, which is convenient for neutrinoless double beta decay search.

The calibration of the Gotthard-TPC with low energy sources was also studied, where the MWPC wires were replaced by a large Micromegas detection plane (50 cm of diameter). A low background is achieved with this large micropattern, which is the largest realized up to now. In addition, the background can be lowered by replacing some radioactive components like resistors, solders and resin-epoxy (the substrate of the detection plane) by quartz, paint silver and kevlar-epoxy, respectively. These components were measured and compared in view of their radioactivities and cost in our Germanium detector at "La vue des Alpes" laboratory.

The working limit of pure CF_4 gas at more than 1 bar pressure was also observed. At 2 bar of CF_4 pressure, the energy resolution is bad and the working region is limited. This effect is caused by electron attachment in this gas, which is also studied in our work and some suggestions are given to alleviate the electron attachment by this higher electronegative gas, by adding xenon or argon or by replacing the MWPC by the Micromegas structure.

In addition, choices of gas mixtures were studied by computer programs and good agreement between simulations and measurements were found. Charge collection is favored in Xe by a small addition of CF_4 (2%), and electron attachment caused by this last one is alleviated by Xe addition. Knowing that the high scintillation yields in this couple of gases can be a precious factor to improve energy resolution by collecting both charge and scintillation signals.

Perspectives

We discussed the performance of a Micromegas-TPC with Xe-CF_4 gas mixtures and we studied charge collection, getting high gas gains with good energy resolutions. We mentioned that detector performance can still be improved. Getting both charge and light information, will improve the energy resolution. We suggest some developments to achieve this goal:

One can change the detection plane by an X-Y readout plane (also a compact one), keeping insulators between copper pads (strips), in order to obtain the position information.

It is possible to put some fibers faced to the internal mini-TPC side and exit them to the outside of the chamber to photomultipliers, through the hole used before for the sense and potential wires fee through. Another possibility, which needs more investigations, is to built a miniTPC-cover embedding photodiodes in it. Large APD's [80] having higher quantum efficiency than photomultipliers are most promising.

Using both possibilities is not excluded.

When applying a low drift electric field in high pressure Xe-CF_4 gas mixtures, we will be able to collect primary scintillation on these APD's, which permits to determine the "start" time of the primary scintillation and then the absolute beginning time of the primary track. The opaque cathode plane would be replaced by a woven wire mesh plane.

An easy work to do is to paint the internal edge of the chamber with reflective paint, to insure total reflection.

Reading the anode signal, allows to compare grid and anode signals and to be sure that we collect total or partial charge, which gives us an idea about the feedback of ions to the drift space.

An important study to do is to develop a purification system for Xe gas mixtures, including radon and krypton extraction.

Other applications

The Micromegas-TPC detector with its simple design and high amplification, provides high performance from moderate and large diameters (9 cm up to 50 cm). So, we can use this device in different applications [81]. Some of them are:

- **Long drift Micromegas-TPC** :
  - Neutrinos and astroparticle physics (HELLAZ [82], ICARUS [83], NOSTOS [28], T2K [84] ...).
  - Axions and dark matter (CAST [85, 86], Drift [87], MIMAC [88] ...).
  - Trajectography (COMPASS [79], NA48/KABES [89], TESLA [90] ...).
- **Small drift Micromegas-TPC** :
  - Micromegas-based gaseous photomultipliers filled with Xe-CF_4 admixture can be developed, for the UV and the visible spectral range. Progress in this field with Multi-GEM micropattern cited in reference [91] are very encouraging.
  - Nuclear physics for neutral particles detection, for example crystal diffraction to determine molecular and proteins structures.
  - Medicine, for X-ray radiography using large detection plane with a small drift volume. Large flat area and high resolution needed in mammal radiography [92]. It can be used as a device for monitoring during cancer treatment.

- The Micromegas-TPC operated in Xe-CF_4 gas mixture at higher pressure, can be used for medical imaging. For example, imaging in Xe gas with MSGC's [67] and with MWPC's [93] at high pressure preceded. In addition, a triple-GEM detector [50] was filled with the pure Xe and the maximum achievable gain did not exceed 10^4 at 1 atm and 10 at 4 atm of pressures. Moreover, all the three GEMs were completely damaged after few discharges when operated in Xe (there were no damage in Ar and Ne gases for example)[9]. But, the Micromegas grid remains intact after all tests presented in this work and the gas gain achieved 10^3 at 4 bar of Xe(98)CF_4(2) (see the left of figure 5.5) without any additional amplification.
- Safety control at ports and airports ...

[9]More details are in the previous reference [50].

Appendix A

A few $\beta\beta$ emitting isotopes

Isotopes	$Q_{\beta\beta}$ [MeV]	Iso. abundance [%]	exp. $T^{2\nu}_{1/2}$ [year]
^{48}Ca	4.271	0.187	$> 4.0 \times 10^{19}$ [23]
^{76}Ge	2.039	7.8	$> 1.4 \times 10^{21}$ (Heid-Moscow, IGEX, **GENIUS**, **Majorana**)
^{82}Se	2.995	9.2	$> 0.9 \times 10^{20}$ (NEMO)
^{96}Zr	3.35	2.8	$> 2.1 \times 10^{19}$
^{100}Mo	3.034	9.6	$> 8.0 \times 10^{18}$ (NEMO, **MOON**)
^{116}Cd	2.802	7.5	$> 3.3 \times 10^{19}$
^{128}Te	0.868	31.7	$> 2.5 \times 10^{24}$
^{130}Te	2.533	34.5	$> 0.9 \times 10^{21}$ (CUORE)
^{136}Xe	2.479	8.9	**not observed yet** (Gotthard, **EXO**, **XMASS**)
^{150}Nd	3.367	5.6	$> 7.0 \times 10^{18}$

Large released decay energy "$Q_{\beta\beta}$" and natural abundance, are the most preferred properties for "$0\nu\beta\beta$" candidate isotope. The first desirable property, puts the sharp peak of "$0\nu\beta\beta$" above the background of "$2\nu\beta\beta$" continuous spectrum (see figure 1.1). The second property, makes the experiment cheaper.

The calcium ^{48}Ca is fantastic with its highest released energy, but it has a very low natural abundance.

The tellurium ^{130}Te has a moderate released energy, but no enrichment is needed.

Germanium ^{76}Ge has low released energy, moderate isotopic abundance, yet currently has the best sensitivity.

^{136}Xe has moderate abundance, but enrichment is relatively inexpensive (noble gas).

Appendix B

Gaseous micropattern detectors

- **SWPC**: Single Wire Proportional Chamber, developed just after the discovery of electromagnetic radiation [98].
- **MWPC**: Multi Wire proportional Chamber, developped by Georges Charpak in 1968 year [55].
- **MSC**: Multi Step Chamber, introduced by Charpak and Sauli [99].
- **MGC**: Multi Gap Chamber, invented by Angelini [100].
- **Micromegas**: Micro mesh gaseous structure, invented in 1996 by G. Charpak and Y. Giomataris [30].
- **CAT**: Compteur A Trou, it consists of a narrow hole micro-machined in an insulator metallized on the surface of the cathode [101].
- **MSGC**: Micro Strip Gas Chambers, invented in 1988 by Oed [102].
- **GEM**: Gazeous Electron Multiplier, introduced in 1997 by Sauli [103].
- **LEM**: Large Electron Multiplier, developed in our laboratory and cited in reference [104].

- **PIM**: Parallel Ionization Multiplier [105].

- **MDC**: Micro Dot Counters, anode dots surrounded by cathode rings [106].

- **MCPC**: Multi Cell Proportional Counter designed to search for WIMP [107].

Appendix C

Physics phenomena

C.1 Source decay and fluorescence

In the ^{55}Fe source, an electron from the K electron shell of the radioactive-atom Fe is absorbed via electro-weak interaction by a proton from the nucleus. Hence, this proton is transformed into a neutron with subsequent emission of a neutrino. The captured electron belongs generally to the internal layer of the atom. The gap created by the electron-capture in the internal orbital close to the nucleus is compensated by rearrangement of the electronic-procession. This rearrangement is accompanied by a fluorescence X-ray of about 5.9 keV, as shown below:

$$^{55}_{26}\mathrm{Fe}\,(\mathrm{instable}) + e^- \rightarrow\ ^{55}_{25}\mathrm{Mn}\,(\mathrm{stable}) + \nu_e + \gamma \tag{C.1.1}$$

Electron energy: $\mathrm{Q}_{EC} = 231.6$ keV.

Percentage: 100%.

Photon energy: $\mathrm{E}_\gamma = 5.898$ keV.

Half life: $\mathrm{T}_{1/2} = 2.73$ y.

Given the low energy of X-rays emitted by the iron source, the photoelectric effect dominates.

C.2 Photoelectric effect

The photoelectric effect corresponds to the ionization of the more attached electronic layers (K, L..) of atoms, which can be reorganized by emitting secondary electromagnetic X rays or electronics (Auger electrons). The first ionization:

$$\gamma(\mathrm{E_I}) + \text{gas molecule} \rightarrow (\text{gas molecule}^*)^+ + e^-(\mathrm{E_c}) \tag{C.2.1}$$

The photon emitted by rearrangement of the electron shells following incident energy E_I transfers his energy to an electron of the crossed gas medium. This electron is then ejected from its orbit with a kinetic energy $E_c = E_I - E_L$: E_L is the liaison energy of the ejected electron on its orbit.

C.3 Delta electrons

The electrons, liberated from the molecule, have sufficient energy to ionize further gas molecules before drifting towards the detection plane. These secondary electrons called "Delta electrons" look like hairs along the track. They result from particularly large energy transfers of the particle to an electron of a gas molecule.

C.4 Auger electrons

Auger electrons result from the return of an excited atom to a lower energy state by the emission of an electron rather than a photon, this mechanism is known as "Auger effect". The emitted electron may have enough energy to ionize further gas molecules, in which case these electrons look like delta electrons.

C.5 Penning effect

The penning effect contributes with a non-negligible amount to the ionization process in the gas mixture. It consists of the de-excitation of the excited noble gas which gains its stable state by ionizing the another gas (quencher) added to the primary component as follows:

$$(\text{basic gas})^* + (\text{quencher}) \rightarrow (\text{basic gas}) + (\text{quencher})^+ + \text{e}^-.$$

Therefore, it should be kept in mind, although the fraction of the excited noble gas state, that the quantity of the ionized quencher molecules, is not known. The question is: how much the Penning effect contributes to the gas gain?

Appendix D

Operational modes in the gas chamber

Depending on the applied voltage between TPC electrodes, especially in the case of MWPC, mainly three modes can exist: ionization, proportional and Geiger-Muller chambers. Figure D.1 presents distinct zones in gaseous chambers:

D.1 The ionization chamber

At very low electric field, electrons and ions move slowly, and are likely to form pairs. This mechanism is called "recombination". In this phase, there is no gas amplification. Several hundreds of volts applied to the electric field, is sufficient to prevent recombination. The detector is called "ionization chamber". There is also no multiplication but, only the primary charges are collected. The current signal increases slowly.

D.2 The proportional chamber

At higher electric field, the current increases rapidly. The field is strong enough to accelerate free electrons produced in the first ionization and increase their kinetic energy. These free electrons, have enough energy and can by their own ionize gas molecules. The electrons liberated in these secondary ionizations, are also accelerated to ionize in turn,

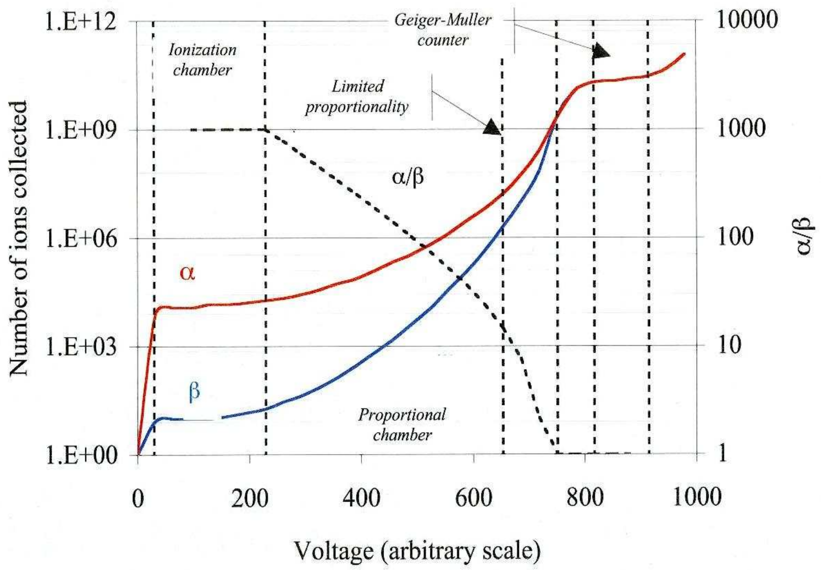

Figure D.1: Typical evolutions of the detector signal as a function of applied voltages for α (red) and β (blue) particles.

and so on ... This process is called "ionization avalanche", which is omnipresent in the amplification region. The charge collected is proportional to the primary ionisation, this is why, it is called "proportional chamber".

Take in mind that: recombination in densely ionized region is reduced with high electric fields.

D.3 The Geiger-Muller chamber

At very high electric field, the current is so high that electric breakdowns occur and the rate of discharges is very important. The avalanche region is so dense that the gain is saturated and the chamber is operated in the "Geiger-Muller" mode.

Appendix E

Software programs

¶***Maxwell:***

Maxwell [43] is an electromagnetic field simulation software for signal integrity and detector design applications. We used only the $2-3D$ simulation program, which is a drawing tool, using the finite element method to simulate the electric field inside the TPC with RZ symmetry. Hence, electric field maps inside the chamber are produced and imported to Garfield.

¶***Garfield:***

Garfield [44] was written in Fortran77 by Rob Veenhof at CERN [94], for detailed simulation of two and three dimensional drift chambers. This program is able to determine *field configurations* for two dimensional chambers and it also accepts two and three-dimensional field maps generated by Maxwell program, as basis of its calculations. Garfield is also interfaced to Magboltz and Heed.

The program was only exploited to calculate electric field, contour plots inside the chamber and determine plots of electron and ion drift lines near the detection plane.

¶***Magboltz:***

Magboltz [95] was written by Stephen Biagi. It computes electron transport properties (drift velocity, diffusions, amplification and attachment) in different gas mixtures, by solving the Boltzmann transport equations under the influence of electromagnetic fields. This program is interfaced to Garfield.

¶***Imonte:***

Imonte [96], also written by Stephen Biagi, is a high field version of Monte Carlo. It is developed as a continuity of Magboltz. It is used where ionization and attachment are important. This program was essential to compute electrons lost in CF_4 gas, when attachment is accented.

¶***Heed:***

Heed [97] was written by Igor Smirnov and simulates ionization of molecules hit by charged particles. It also computes the energy loss of incident particles, taking into account, delta electrons and multiple scattering of the incoming particles. Heed is also interfaced to Garfield.

Appendix F

Cross sections used by Magboltz

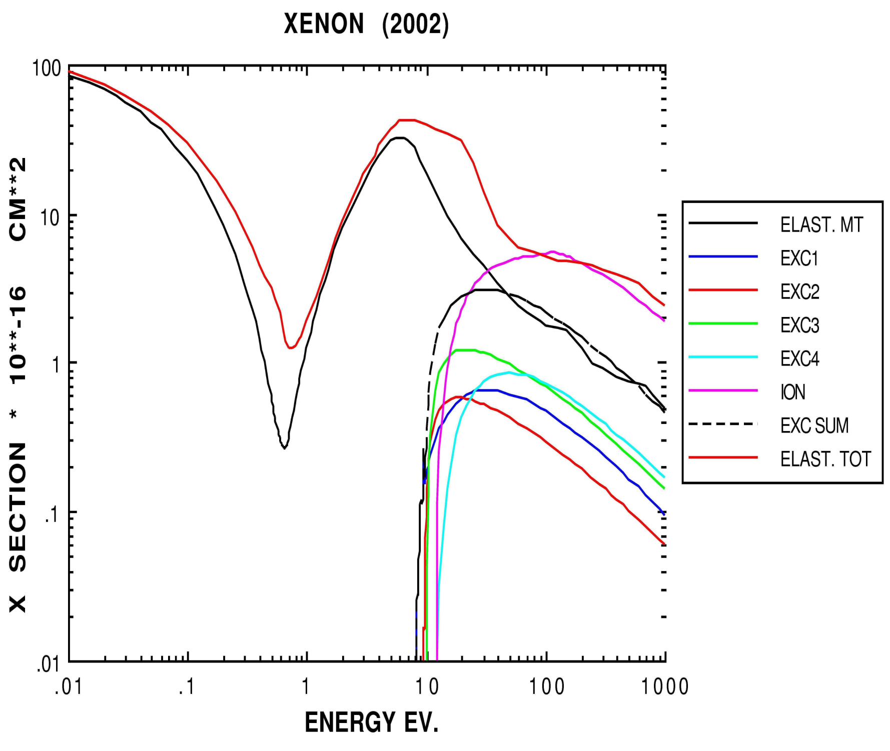

Figure F.1: Cross sections for electron collisions in Xenon.

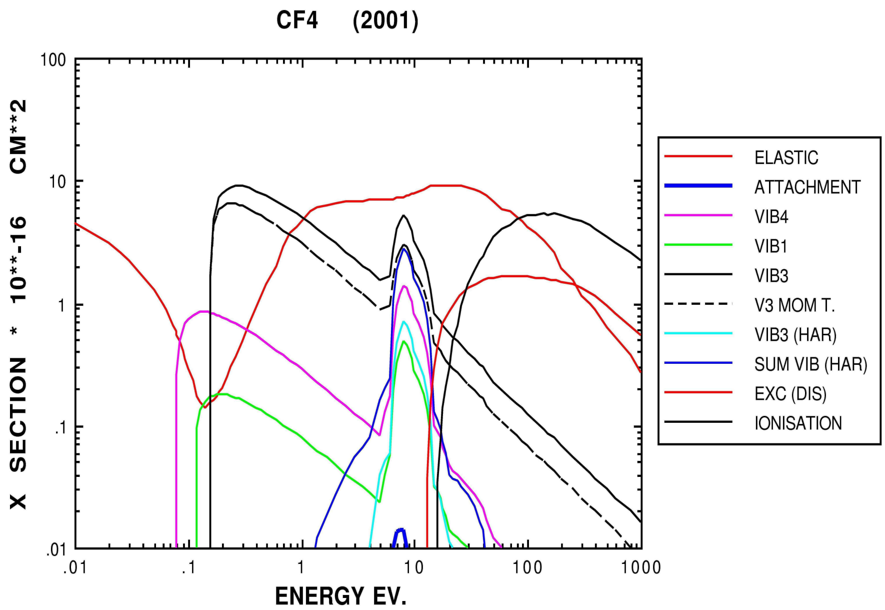

Figure F.2: Cross sections for electron collisions in CF_4.

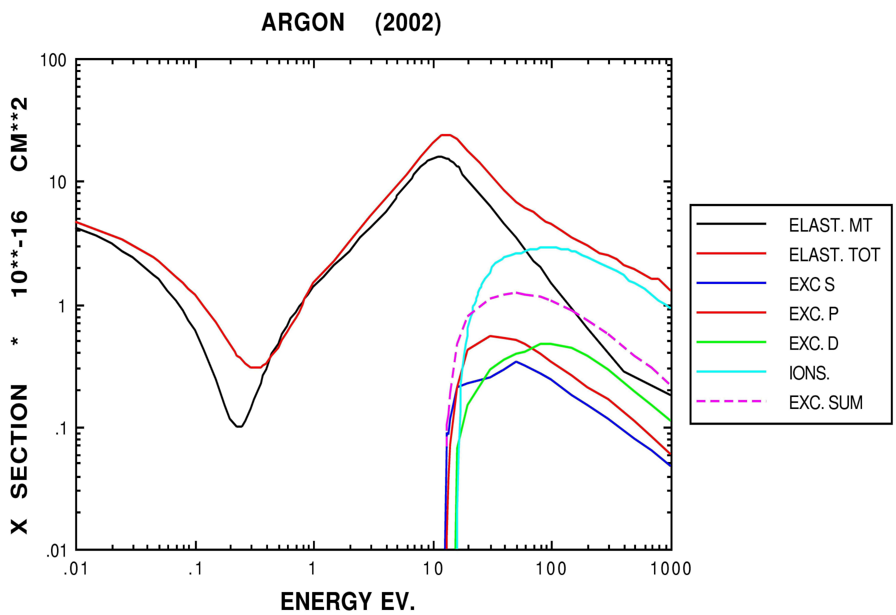

Figure F.3: Cross sections for electron collisions in Argon.

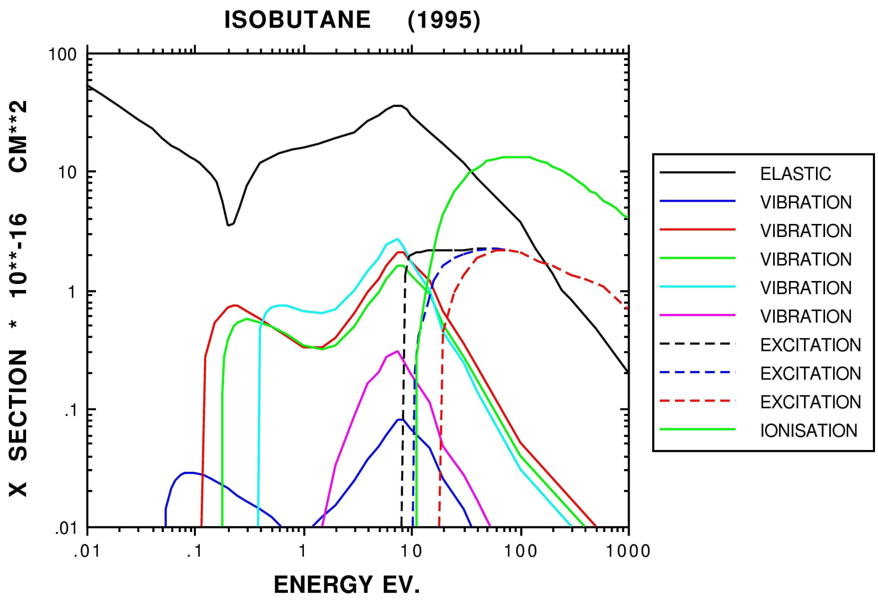

Figure F.4: Cross sections for electron collisions in isobutane.

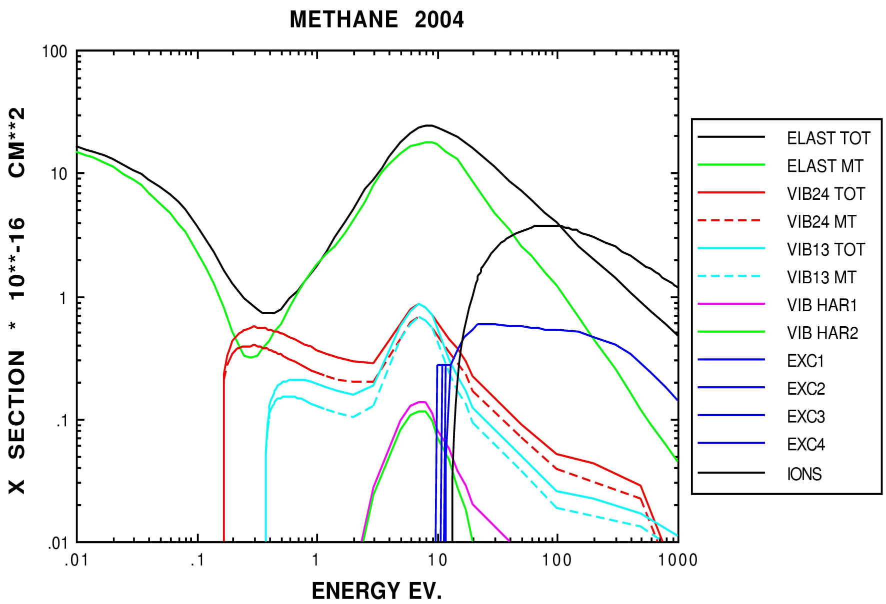

Figure F.5: Cross sections for electron collisions in CH_4.

Acknowledgements

I would like to thank Jean-Luc Vuilleumier, my supervisor, for his constant support during this thesis work and his many suggestions and rich discussions.

Professor Yannis Giomataris and Viktor Zacek expressed their interest in my work and provisioning me with the preprints of some of precious ideas, which gave me a better perspective on my own results.

I am thankful to Jose Busto and Frederic Juget for their critical reading and rereading my manuscript.

I am also thankful to Damian Twerenbold for his comments citing defenselessness points, which permits me to better improve my manuscript.

I am also thankful to Jean-Michel Vuilleumier for his continuous disposal on technical assistance.

I had the pleasure of meeting the particle physics group (Zornitza Daraktchieva, Markus Hauger, Eric Baussan, Iozsef Janicsko Csathy, Dominique Schenker and Patrick Weber). They are sympathetic people.

Finally, I wish to thank the following people: Rob Veenhof (for his disposability and initiating me to simulation programs); the staff of electronic, especially, Daniel Varidel for his sympathy and Urs Bart (for his strange behavior); the staff of mechanic, particularly, Jean-Louis Moratel for his doing the new gas station, Cornu André for his sympathy, and Thierry Delhove (for his bad collaboration); The staff of secretary (Anne Marie Milo, Nicole Derendinger and Muriel Vallery-Mügeli) for their administrative work and their usual smiles; Ichraf, Gersende, Amel, Antonia (for their friendships)...

Of course, I am grateful to my husband for his patience and love, to my daughter and my girl for their wrestling with a fully occupied mother, to the mind of my father, to my mother for his continuous encouragement and the great help to accommodate my girl with tenderness, in order to accomplish this work, to my sisters (Hadia and Yasmin) and brothers (Mourad and Yamen), to the family of my husband and to the mind of my stepfather. Without them, this work would never be accomplished literally.

I should also mention that my work was supported in part by the "Fond National Suisse" and in the other part by the "Etat de Neuchâtel".

Please forgive me if I forgot someone:

I am grateful to who's thinking to me.

Neuchâtel, October 25^{th}2006 Leila Ounalli

Remerciements

Ce travail de thèse a été réalisé sous la direction du professeur Jean-Luc Vuilleumier, à qui je tiens à exprimer mes vifs remerciements pour son appui constant, ses discussions constructives le long de ce travail et pour avoir mis à disposition les moyens nécessaires pour accomplir ce travail dans les meilleures des conditions.

Je remercie Les professeurs Yannis Giomataris et Viktor Zacek pour leurs intérêts à mon travail ainsi que leurs remarques et suggestions qui m'ont permis de mieux présenter mes résultats.

Je suis reconnaissante à Jose Busto et Frederic Juget pour la lecture de mon manuscrit et pour ce qu'ils m'ont apporté pour son amélioration.

Je suis également reconnaissante à Damian Twerenbold de ses commentaires utiles pour la présentation du manuscrit.

J'exprime ma gratitude à Jean-Michel Vuilleumier pour sa disponibilité, son assistance technique, et son enthousiasme pour le travail que j'ai fait.

Je remercie les membres du groupe de physique de particules pour leurs sympathies (Zornitza Daraktchieva, Markus Hauger, Eric Baussan, Iozsef Janicsko Csathy, Dominique Schenker et Patrick Weber).

Je tiens à remercier les personnes suivantes: Rob Veenhof pour sa disponibilité et son aide pour les programmes de simulation; le personnel de la section de l'électronique, en particuier, Daniel Varidel pour sa sympathie et Urs Bart (pour son comportement étrange); le personnel de la section du mécanique, particulièrement, Jean-Louis Moratel pour la

construction de la nouvelle station de gaz; Cornu André pour sa sympathie et Thierry Delhove (pour sa mauvaise collaboration);
J'adresse mes remerciements aux secrétaires de l'institut Anne Marie Milo, Muriel Vallery-Mügeli et Nicole Derendinger pour leurs services, leurs sympathies et leurs sourires habituels.
Mes vifs remerciements pour Ichraf, Gersende, Amel et Antonia pour leurs amitiés.
Sans doute, je suis très reconnaissante à mon mari pour sa patience et son amour, à ma fille et mon fils pour leurs luttes avec une mère entièrement occupée, à la mémoire de mon père, à ma mère pour son continuel encouragement, à mes soeurs (Hadia et Yasmin) et mes frères (Mourad et Yamen), à la famille de mon marie et à la mémoire de mon beau-pére.
A tous ceux qui ont une pensée pour moi.
Je devrais aussi mentionner que mon travail a été soutenu par le fond National Suisse pour la recherche Scientifique ainsi que l'état de Neuchâtel.
Pardonnez-moi si j'ai oublié quelqu'un:
je suis reconnaissante à tous ceux qui ont pensé à moi.

Neuchâtel, Le 25 October 2006 — Leila Ounalli

Bibliography

[1] H. Bethe and R. Peierls "The neutrino" Nature, 532, (1934) 133.

[2] P. Anselmann et al. "Implications of the GALLEX determination of the solar neutrino flux", Phy. Lett. B 285, (1992) 390-397.

[3] M. Altmann et al. "GNO solar neutrino observations", Phy. Lett. B 490, (2000) 16-26.

[4] T. Bruce et al. "Measurement of the solar electron neutrino flux with the Homestake chlorine detector", Astrophys. J 496, (1998) 505-526.

[5] K. S. Hirata et al. "Constraints on neutrino oscillation parameters from the Kamiokande-II solar neutrino data", Phys. Rev. Lett 65, (1990) 1301-1304.

[6] J. N. Abdurashitov et al. "Results from SAGE", Phys. Lett. B 328, (1994) 234-248.

[7] B. Aharmim et al. "Electron Energy Spectra, Fluxes, and Day-Night Asymmetries of ^{8}B Solar Neutrinos from the 391-Day Salt Phase SNO Data Set", Phys. Rev. C 72, (2005).

[8] Y. Fukuda et al. "Measurements of the solar neutrino flux from Super-Kamiokande's first 300 days", Phys. Rev. Lett 81, (1998) 1158-1162.

[9] H. T. Wong et al. "A Search of Neutrino Magnetic Moments with a High-Purity Germanium Detector at the Kuo-Sheng Nuclear Power Station", Report, (2006).

[10] Z. Daraktchieva et al. (MUNU collaboration) "Final results on the neutrino magnetic moment from the MUNU experiment", Phy. Lett. B 615, 3-4 (2005) 153-159.

[11] T. Araki et al. "Measurement of Neutrino Oscillation with KamLAND: Evidence of Spectral Distortion", Phys. Rev. Lett 94, (2005) 081801.

[12] D. W. Liu et al. (Super-Kamiokande collaboration) "Limit On the Neutrino Magnetic Moment Using 1496 Days of Super-Kamiokande-I Solar Neutrino Data", Phys. Rev. Lett 93, (2004) 021802.

[13] R. Leuscher et al. "Search for $\beta\beta$ decay in ^{136}Xe: new results from the Gotthard experiment", Phy. Lett. B 434, (1998) 407-414.

[14] C. E. Aalseth et al. "The IGEX Ge-76 neutrinoless double-beta decay experiment: Prospects for next generation experiments", Phys. Rev. D 65, (2002) 092007.

[15] R. Arnold et al. "Limits on different Majoron decay modes of and for neutrinoless double beta decays in the NEMO-3 experiment", Nucl. Phys. A 765, (2006) 483-494.

[16] C. Arnaboldi et al. "A New Limit on the Neutrinoless DBD of ^{130}Te", Phys. Rev. Lett 95, (2005) 142501.

[17] M. Danilov et al. "Detection of very small neutrino masses in double-beta decay using laser tagging", Phys. Lett. B 480, (2000) 12-18.

[18] J. Hellmig, H.V. Klapdor-Kleingrothaus "A large scale double beta and dark matter experiment: GENIUS", Z. Phys. A 359, (1997) 351-359.

[19] C. E. Aalseth et al. "The Majorana Neutrinoless Double-Beta Decay Experiment", Phys. Atom. Nucl 67, (2004) 2002.

[20] H. Ejiri et al. "Spectroscopy of double-beta and inverse-beta decays from Mo-100 for neutrinos", Phys. Rev. Lett 85, (2000) 2917-2920.

[21] Conti et al. "Correlated fluctuations between luminescence and ionization in liquid xenon", phys. Rev. B 68, (2003) 054201.

[22] Z. Maki et al. Prog. Theor. Phys, 28, (1962) 870.

[23] Moe et al. "Double Beta Decay of ^{48}Ca", Phy. Rev. Lett 77-26, (1996) 5186.

[24] H. V. Klapdor-Kleingrothaus et al. "Latest results from the HEIDELBERG-MOSCOW double beta decay experiment", Eur. Phys. J. A 12, (2001) 147-154.

[25] C. E. Aalseth et al. "Recent results of the IGEX Ge-76 double-beta decay experiment", Phys. Atom. Nucl 63, (2000) 1225-1228.

[26] F. Boehm and P. Vogel. "Physics of Massive Neutrinos", Cambridge University Press, (2000).

[27] H. V. Klapdor et al. "Search for neutrinoless double beta decay with enriched ^{76}Ge in Gran-Sasso $1990-2003$", Phy. Lett. B 586, (2004) 198-212.

[28] Y. Giomataris and J. D. Vergados "Neutrino properties studied with a triton source and a large spherical TPC", Nucl. Instr. And Meth. A 530, 3 (2004) 330-358.

[29] D. Nygren et al. "Feasibility tests of a high resolution sampling radial drift chamber", Nucl. Instr. And Meth. A 241, 2-3 (1985) 375-386.

[30] Y. Giomataris et al. "Micromegas: a high-granularity position-sensitive gaseous detector for high particle-flux environments", Nucl. Instr. Meth. A 376, (1996) 29-35.

[31] S. Kubota et al. Phys. Rev. B 17, (1978) 2762.

[32] D. Friedrich et al. "Positive ion effects in large-volume drift chambers", Nucl. Instr. And Meth 158, (1979) 81-88.

[33] F. Sauli, Nucl. Instr. Meth. A 505, (2003) 195-198.

[34] D. Mörmann et al. "Evaluation and reduction of ion back-flow in multi-GEM detectors", Nucl. Instr. And Meth. A 516, 2-3 (2004) 315-326.

[35] F. Sauli et al. "Ion feedback suppression in time projection chambers", Nucl. Instr. And Meth. A 560, 2 (2006) 269-277.

[36] S. Kane et al. Nucl. Instr. Meth. A 505, (2003) 216-218.

[37] L. G. Cristophorou et al. "Fast gas mixtures for gas filled particle detectors", Nucl. Instr. And Meth 163, 1 (1979) 141-149.

[38] Z. Daraktchieva "Experimental study of neutrino-electron scattering at low energy with the Munu experiment", PhD thesis, Neuchâtel, 2004.

[39] G. F Knoll "Radiation detection and measurement", (1979) 2nd edition, New York: Wiley.

[40] N. Ishida et al. "Fano factor in xenon", Phys. Rev. A 46, 3 (1992) 1676-1679.

[41] C. Broggini et al. "A gas detector to measure the $\overline{\nu_e}$ magnetic moment at a nuclear reactor", Nucl. Instr. And Meth. A 311, (1992) 319-326.

[42] P. Jeanneret et al. "Performance of a new Micromegas detector, with woven wire mesh, in CF_4", Nucl. Instr. Meth. A 500, 1-3 (2003) 133-143.

[43] http://wwwce.web.cern.ch/wwwce/ae/Maxwell/

[44] http://garfield.web.cern.ch/garfield/

[45] I. Giomataris et al. "Micromegas in a Bulk", Nucl. Instr. Meth. A 560, (2006) 405-408.

[46] http://consult.cern.ch/xwho/people/27738

[47] http://www.bopp.ch.

[48] Y. Giomataris et al. "Development and prospects of the new gaseous detector "Micromegas"", Nucl. Instr. Meth. A 419, (1998) 239-250.

[49] A. Orthen et al. "Gas gain and signal length measurements with a triple-GEM at different pressures of Ar-, Kr- and Xe-based gas mixtures", Nucl. Instr. And Meth. A 512, 3 (2003) 476-487.

[50] A. Bondar et al. "High pressure operation of the triple-GEM detector in pure Ne, Ar and Xe", Nucl. Instr. And Meth. A 481, (2002) 200-203.

[51] B. Schmidt "Drift properties of electrons in methane and methane noble gas mixtures", Nucl. Instr. And Meth. A 252, 2-3 (1986) 579-585.

[52] Dϕ collaboration "The Dϕ detector", Nucl. Instr. And Meth. A 338, 2-3 (1994) 185-253.

[53] A. Pansky et al. "The scintillation of CF_4 and its relevance to detection science", Nucl. Instr. Meth. A 354, 2-3 (1995) 262-269.

[54] A. Breskin et al. "GEM photomultiplier operation in CF_4", Nucl. Instr. And Meth. A 483, (2002) 670-675.

[55] G. Charpak et al. "The use of multiwire proportional counters to select and localize charged particles", Nucl. Instr. and Meth 62, 3 (1968) 262-268.

[56] C. Amsler et al. (MUNU collaboration) "A new measurement of the $\overline{\nu_e} e^-$ elastic cross section at very low energy", Phys. Lett. B 545, (2002) 57-61.

[57] L. G. Christophorou et al. "Xe-Counting fast gas mixtures for gas-filled detectors", Nucl. Instr. And Meth 171, (1980) 491-495.

[58] B. Jean-Marie et al. "Systematic measurement of electron drift velocity and study of some properties of four gas mixtures", Nucl. Instr. And Meth 159, (1979) 213-219.

[59] J. Derré and I. Giomataris "Recent experimental results with MICROMEGAS ", Nucl. Instr. and Meth. A 477, 1-3 (2002) 23-28.

[60] W. Blum and L. Rolandi "Particle detection with drift chambers", Springer-Verlag, New York, 1994.

[61] L. Ounalli "CF_4 attachment in MUNU experiment", Internal report NEIPH/CORP/03/03, (2002).

[62] J. Lamblin "Performances du détecteur MUNU et perspectives en vue de la détection des neutrinos solaires", PhD thesis, Grenoble, 2002.

[63] W. Zhang et al. "Excitation and ionization of freon molecules", Chem. Phys 137, 1-3 (1989) 391-405.

[64] G. Turban et al. Pure & Appl. Chem 56, 2 (1984) 215-230.

[65] Yu. M. Gavrilyuk et al. "Characteristics of a Proportional Counter Filled with CF_4 and Additions of Xe", Instr. Exp. Tech 46, 1 (2003) 26-31.

[66] S.X. Oda et al. "Development of a time projection chamber using gas electron multipliers (GEM-TPC)", Nucl. Instr. And Meth 564, (2006) 190-196.

[67] D. Gobbin et al. "Photon-counting radiography with the gas microstrip detector", Phys. Med. Biol 44, (1999) 1317-1335.

[68] M. Z. Iqbal et al. "Design and construction of a high pressure xenon time projection chamber", Nucl. Instr. Meth. A 259, (1987) 459-465.

[69] J.-C. Vuilleumier et al. "Search for neutrinoless double-β decay in ^{136}Xe with a time projection chamber", Phys. Rev. D 48, 3 (1993) 1009-1020.

[70] I. Mandic et al. "Thermal neutron damage in DMILL bipolar transistors", Nucl. Instr. Meth. A 518, (2004) 474-476.

[71] R. Luesher "Double Beta Decay in ^{136}Xe: upgrade of the Gotthard experiment, new results and low pressure investigations", PhD thesis, Neuchâtel, 1999.

[72] F. Boehm et al. "The Gotthard experiment on ^{136}Xe $\beta\beta$ decay", Proceedings of the XXXth rencontre de Moriond, Villard sur Ollon (Switzerland), (1995) 213-218.

[73] R. Arnold et al. "First results of the search of neutrinoless double beta decay with the NEMO-3 detector", Phys. Rev. Lett 95, (2005) 182302.

[74] Ch. Murith and A.Gurtner, Radioprotection 34, N°1 (1999) 37-46.

[75] http://www.unine.ch/phys/.

[76] J. Busto and Y. Gonin "Le laboratoire souterrain de la vue-des-alpes: Mesure des quantités de radio-isotopes présents dans la matière", Bulletin de la société neuchâteloise des sciences naturelles 125, (2002) 99-106.

[77] R. L. Brodzinski et al. "The impact of natural radioactivity in solder on low background experiments", Nucl. Instr. Meth. A 254, (1987) 472-473.

[78] J. Busto, Private communication, Sep 2006.

[79] C. Bernet et al. "The 40×40 cm^2 gaseous microstrip detector Micromegas for the high-luminosity COMPASS experiment at CERN", Nucl. Instr. And Meth. A 536, 1-2 (2005) 61-69.

[80] J. A. M. Lopes et al. "A large area avalanche photodiode as the VUV photosensor for gas proportional scintillation counters", Nucl. Instr. And Meth. Phys. Res. A 454, (2000) 421-425.

[81] G. Charpak et al. "Micromegas, a multipurpose gaseous detector", Nucl. Instr. And Meth. A 478, 1-2 (2002) 26-36.

[82] P. Gorodetzky et al. "Identification of solar neutrinos by individual electron counting in HELLAZ", Nucl. Instr. And Meth. A 433, 1-2 (1999) 554-559.

[83] F. Arneodo et al. "Study of solar neutrinos with the 600-t liquid argon ICARUS detector", Nucl. Instr. And Meth. A 455, (2000) 376-389.

[84] D. Karlen "Near detectors for the T2K experiment ", Nucl. Phys. B 159, (2006) 91-98.

[85] A. Samuel et al. "CAST: A low-background Micromegas detector for axion searches", Nucl. Instr. And Meth. A 535 (2004) 309-313.

[86] S. Andriamonje et al. "A Micromegas detector for the CAST experiment", Nucl. Instr. And Meth. A 518, 1-2 (2004) 252-255.

[87] Ben Morgan "DRIFT: a directionally sensitive dark matter detector", Nucl. Instr. And Meth. A 513, 1-2 (2003) 226-230.

[88] E. Moulin, F. Mayet and D. Santos "Supersymmetric dark matter search via spin-dependent interaction with ^{3}He", Phys. Lett. B 614, 3-4 (2005) 143-154.

[89] B. Peyaud "KABES: a novel beam spectrometer for NA48", Nucl. Instr. And Meth. A 535, 1-2 (2004) 247-252.

[90] N. Ghodbane "The TESLA time projection chamber", Nucl. Phys. B 125, (2003) 258-262.

[91] R. Chechik, et al. "Progress in GEM-based gaseous photomultipliers", Nucl. Instr. And Meth. A 502, (2003) 195-199.

[92] A. Bressan et al. "Two-dimensional readout of GEM detectors", Nucl. Instr. And Meth 425 , (1999) 254-262.

[93] G. Charpak "Applications of proportional chambers to some problems in medecine and biology", Nucl. Instr. And Meth 156, 1-2 (1978) 1-17.

[94] R. Veenhof, Nucl. Instr. And Meth. A 419, (1998) 726-730.

[95] http://consult.cern.ch/writeup/magboltz/

[96] S. F. Biagi "Monte Carlo simulation of electron drift and diffusion in counting gases under the influence of electric and magnetic fields", Nucl. Instr. And Meth. Phys. Res. A 421, (1999) 234-240.

[97] http://consult.cern.ch/writeup/heed/

[98] Townsend and Raether "conduction of electricity through gases", Proc. of Roayl Society. A 81, (1908) 141.

[99] A. Breskin et al. "The multistep avalanche chamber: A new family of fast, high-rate particle detectors", Nucl. Instr. And Meth 161, 1 (1979) 19-34.

[100] F. Angelini, et al. "The micro-gap chamber", Nucl. Instr. And Meth. A 335, 1-2 (1993) 69-77.

[101] G. Chaplier et al. ”Preliminary results of the experimental and simulated intrinsic properties of the Compteur A Trou (CAT) detector: behavior with synchrotron radiation”, Nucl. Instr. And Meth. A 426, 2-3 (1999) 339-355.

[102] J. Lee-Franzini ”The CUSB-II detector”, Nucl. Instr. And Meth. A 263, 1 (1988) 35-42.

[103] F. Sauli ”GEM: A new concept for electron amplification in gas detectors”, Nucl. Instr. And Meth. A 386, 2-3 (1997) 531-534.

[104] P. Jeanneret ”Time Projection Chambers and detection of neutrinos”, PhD thesis, Neuchâtel, 2001.

[105] L. Luquin et al. ”Parallel Ionization Multiplier (PIM): application of a new concept of gaseous structure to tracking detectors”, Nucl. Instr. And Meth. A 518, 1-2 (2004) 135-138.

[106] S. F. Biagi et al. ”First experimental results from a microdot gas avalanche detector integrated onto a silicon wafer” Nucl. Instr. And Meth. A 366, 1 (1995) 76-78.

[107] J. Gavriljuk et al. ”Search for WIMP’s with the Multicell Proportional Counter” Abstracts of papers, Proc. 2nd Workshop on the Dark Side of the Universe: Experimental Efforts and Theoretical Framework, Rome, 1995. Singapore: World Sci. (1996) 203-210.